ABSTRACT

BORON-BASED NANOSTRUCTURES: SYNTHESIS, FUNCTIONALIZATION, AND CHARACTERIZATION

Eyrusalam Bedasso, Ph.D.
Department of Chemistry and Biochemistry
Northern Illinois University, 2015
Narayan S. Hosmane, Director

Boron-based nanostructures have not been explored in detail; however, these structures have the potential to revolutionize many fields, including electronics and biomedicine. The research discussed in this dissertation focuses on synthesis, functionalization, and characterization of boron-based zero-dimensional nanostructures (core/shell and nanoparticles) and one-dimensional nanostructures (nanorods).

The first project investigates the synthesis and functionalization of boron-based core/shell nanoparticles. Two boron-containing core/shell nanoparticles, namely boron/iron oxide and boron/silica, were synthesized. Initially, boron nanoparticles with a diameter between 10-100 nm were prepared by decomposition of nido-decaborane ($B_{10}H_{14}$) followed by formation of a core/shell structure. The core/shell structures were prepared using the appropriate precursor, iron source and silica source, for the shell in the presence of boron nanoparticles. The formation of core/shell nanostructures was confirmed using high resolution TEM. Then, the core/shell nanoparticles underwent a surface modification. Boron/iron oxide core/shell nanoparticles were functionalized with oleic acid, citric acid, amine-terminated polyethylene glycol, folic acid, and dopamine, and boron/silica core/shell nanoparticles were modified with 3-(amino propyl)

triethoxy silane, 3-(2-aminoethyleamino)propyltrimethoxysilane), citric acid, folic acid, amine-terminated polyethylene glycol, and O-(2-Carboxyethyl)polyethylene glycol. A UV-Vis and ATR-FTIR analysis established the success of surface modification. The cytotoxicity of water-soluble core/shell nanoparticles was studied in triple negative breast cancer cell line MDA-MB-231 and the result showed the compounds are not toxic.

The second project highlights optimization of reaction conditions for the synthesis of boron nanorods. This synthesis, done via reduction of boron oxide with molten lithium, was studied to produce boron nanorods without any contamination and with a uniform size distribution. Various reaction parameters such as temperature, reaction time, and sonication were altered to find the optimal reaction conditions. Once these conditions were determined, boron nanorods were produced then functionalized with amine-terminated polyethylene glycol.

NORTHERN ILLINOIS UNIVERSITY

DEKALB, ILLINOIS

DECEMBER 2015

BORON-BASED NANOSTRUCTURES: SYNTHESIS, FUNCTIONALIZATION, AND CHARACTERIZATION

BY

EYRUSALAM KIFYALEW BEDASSO

A DISSERTATION SUBMITTED TO THE GRADUATE SCHOOL

IN PARTIAL FULFILLMENT OF THE REQUIREMENTS

FOR THE DEGREE

DOCTOR OF PHILOSOPHY

DEPARTMENT OF CHEMISTRY AND BIOCHEMISTRY

Doctoral Dissertation Director:
Narayan S. Hosmane

ACKNOWLEDGEMENTS

I would like to thank my advisor Dr. Narayan S. Hosmane for his guidance and support during my doctoral journey. He gave me the freedom to work on multiple projects and demanded a high quality of work, which pushed me to work harder and accomplish more. Additionally, I would like to thank my committee members, Professor Chong Zheng, Professor Jon Carnahan, Professor Timothy Hagen, and Professor Yassuo Ito for their contribution to my dissertation. In particular, Professor Yassuo Ito has collaborated with me in projects and has assisted me significantly with TEM/STEM and EELS data collection and interpretations; I would like to express my genuine gratitude. He encouraged me to explore the deeper issues, taught me additional characterization methods and explained the ideas and topics in detail so that I could have a better understanding.

I would also like to thank Lori Bross from Biological Sciences for TEM analysis, Dr. Zhili Xiao from Physics for magnetic measurements, Dr. Nestor Zaluzec and Jie Wang from Argonne National Laboratory for their input on TEM/STEM, Heather Barkholtz of Northern Illinois University (NIU) for EDX analysis, Dr. James Mabon and Dr. Haijun Yao of the University of Illinois at Urbana-Champaign for XPS analysis, Dr. Verkatram Mereddy of the University of Minnesota Duluth and Dr. Masao Takagaki of Kyoto University for cytotoxicity studies. Use of the Center for Nanoscale Materials, an Office of Science user facility, was supported by the U. S. Department of Energy, Office of Science, Office of Basic Energy Sciences, under Contract No. DE-AC02-06CH11357. This work made use of the EPIC facility

(NU*ANCE* Center- Northwestern University), which has received support from the MRSEC program (NSF DMR-1121262) at the Materials Research Center, the International Institute for Nanotechnology (IIN), and the State of Illinois, through the IIN. I am grateful for the financial support of Northern Illinois University (NIU). Also, I ought to thank Dr. Hosmane's past and present group members, Dr. Amartya Chakrabarti, Dr. Vijayaraghavan Kalavakunda, and others.

Many others have guided me in my studies during my doctoral program. Most importantly, my mother Zewdinesh Eshete and my uncle Hailegiorgis Legesse have been constantly encouraging, motivating, and reminding me why I am here. And I am grateful for their unconditional love and support. Also Ayonaiel Ghiday has been a continual source of motivation and happiness.

Without the help of these people and many other colleagues, friends, and family I would not have been able to complete my education at Northern Illinois University. I am forever grateful for all who assisted me in my education.

DEDICATION

To everyone who has helped me in my education throughout my life.

TABLE OF CONTENTS

Page

LIST OF TABLES

Table Page

LIST OF FIGURES

LIST OF ABBREVIATIONS

0-D	Zero-dimensional
1-D	One-dimensional
2-D	Two-dimensional
AEAPS	3-(2-aminoethyleamino)propyltrimethoxysilane
APTES	3-(amino propyl) triethoxy silane
ATR	Attenuated total reflection
BNCT	Boron neutron capture therapy
BPA	Boronophenylalanine
BSH	Mercaptoundecahydrododecaborate
CTAB	Hexadecyl trimethyl ammonium bromide
CVD	Chemical vapor deposition
DA.HCl	Dopamine hydrochloride
DI	Deionized
DMF	N,N'-dimethylformamide
DMSO	Dimethyl sulfoxide
EDC	1-ethyl-3-(3-dimethylamino-propyl) carbodiimide hydrochloride
EDX	Energy-dispersive X-ray spectroscopy
EELS	Electron energy-loss spectroscopy

FTIR	Fourier-transform infrared spectroscopy
HAADF	High-angle annular dark field
HRTEM	High-resolution transmission electron microscopy
MRI	Magnetic resonance imaging
NHS	*N*-hydroxysuccinimide
ODCB	Orthodichlorobenzene
PBS	Phosphate buffered saline
PEG	Polyethylene glycol
SDBS	Sodium dodecylbenzenesulfonate
SDS	Sodium dodecyl sulfate
SEM	Scanning electron microscopy
TEM	Transmission electron microscopy
TEOS	Tetraethoxysilane
UV-Vis	Ultraviolet-visible spectroscopy
XPS	X-ray photoelectron spectroscopy
XRD	X-ray diffraction
ZnS	Zinc sulfide

CHAPTER 1

INTRODUCTION

1.1 Nanotechnology

The process of manufacturing materials in nanoscale is called nanotechnology. The first person to illustrate the idea of creating and developing products with atomic size was Richard Feynman in 1959 at the American Physical Society conference with a talk titled "There Is Plenty of Room at the Bottom."[1] Then later in 1974 N. Taniguchi used the word "nanotechnology" at the international conference on industrial production in Tokyo. Over a decade later in 1986 E. Drexler published a book called *Engines of Creation: The Coming Era of Nanotechnology* which contains a thorough description of nanotechnology.[2] In the 1990's and 2000's more discoveries and important institutions such as National Nanotechnological Initiative (NNI) and Nanotechnological Program of National Scientific Fund were created that allow the expansion of this idea.[3]

Even though the idea gained a lot of attention in the 1990's, nanotechnology has been around for a few centuries. For example, painters in the 16th through 18th centuries used gold chloride and silver nitrate in stained glass to achieve a red and yellow color.[4] These colors are a result of gold and silver quantum dots. Even earlier in the 4th century the Lycurgus Cup at the British Museum demonstrated the same idea by exhibiting a green or red color depending if a light source is inside or outside the cup.[5]

The development of this technology leads to the ability to manipulate and construct structures atom by atom. This process provides great control to modify various characteristics of particular nanomaterials; as a result these materials can be altered for specific uses. The freedom to control certain features of nanomaterials significantly increases the various fields the technology can be utilized in. In the last 40 years, this technology has been used to fabricate novel materials that impact human life positively and more research is required to fully understand the extent of nanotechnology. Furthermore, the investment in nanotechnology worldwide, including U.S.A, Japan and European countries, increased from $1.5 billion in 2001 to over $4 billion in 2005.[6] In return, nanotechnology contributed $251 billion to the global economy in 2009 and is estimated to increase to $2.4 trillion by 2015.[7]

1.2 Nanomaterials

Nanomaterials have gained large interest in the last three decades following the invention of the scanning tunneling microscope in 1981. Nanomaterials are defined as a structure with at least one of its dimensions between 1-100 nm.[8] As a result, nanomaterials exhibit unique chemical and physical properties. Some of these properties include: (i) Color,[9] such as cadmium selenide nanoparticles, which have multiple colors depending on the diameter of particles; small particles with high energy corresponding to shorter wavelength display blue color; and larger particles with low energy corresponding to longer wavelength display red color (Figure 1.1).[10] (ii) Size-dependent melting point (Figure 1.2[11] shows the decrease in melting point of tin nanoparticles as the particles get smaller). (iii) High surface atom-to-volume ratio, which refers to when the structure is getting smaller and smaller the total number of atoms deceases with an even larger decrease in volume, forcing the atoms that are present to exist on the surface. (iv) High surface

energy. However, nanotechnology is still not well established; as a consequence, the interactions responsible for these rare chemical and physical properties are not known.

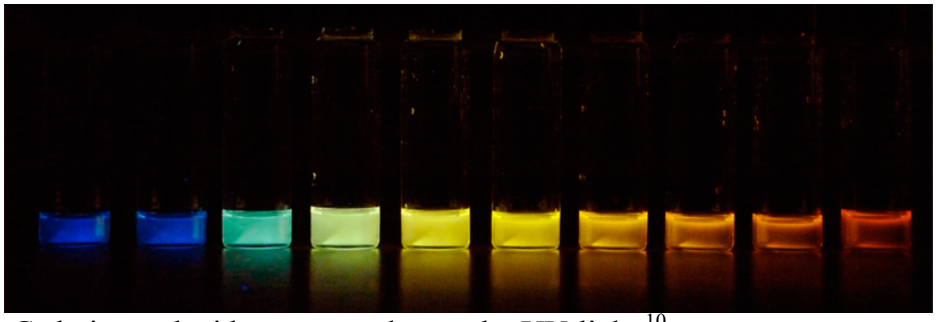

Figure 1.1: Cadmium selenide quantum dots under UV-light.[10]

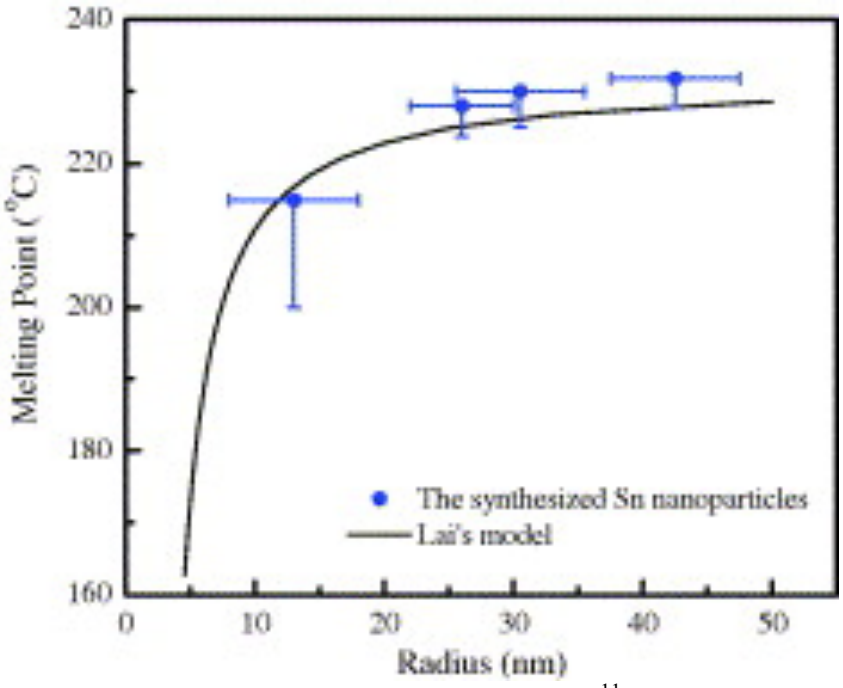

Figure 1.2: Size-dependent melting point of tin nanoparticles.[11]

Most of these unique properties give an advantage to nanomaterials compared to bulk structures. On the other hand, properties such as high surface energy (Table 1.1) are not so beneficial since the structure of high surface energy is thermodynamically unstable and is likely

to decrease the surface energy by aggregation followed by agglomeration. As a consequence, the nanostructures essentially lose their nanodimension. However, there are a few methods to lower surface energy while maintaining nanodimension of the structure: (i) surface relaxation, where atoms on the surface can move inward or laterally; (ii) surface adsorption, when dangling bonds on the surface form chemical bonds with atoms in the surroundings; (iii) surface restructuring, in which broken bonds attach together to form strained bonds; and (iv) surfactants and polymers attached to the nanostructure prevent the structures from aggregating through steric hindrance.[12]

Table 1.1

Change in Total Surface Area and Surface Energy Based on Particle Size.[12]

Side (cm)	Total surface area (cm^3)	Surface energy (J/g)
0.77	3.6	7.2×10^{-5}
0.1	28	5.6×10^{-4}
0.01	280	5.6×10^{-3}
0.001	2.8×10^{3}	5.6×10^{-2}
10^{-4}(1μm)	2.8×10^{4}	0.56
10^{-7}(1 nm)	2.8×10^{7}	560

1.3 Classification of Nanostructures

Nanostructures are generally categorized into different groups based on the axis of growth or dimension. The first category is zero-dimensional (0-D) nanostructures, where structures are confined in all three dimensions like nanoparticles and core/shell nanostructures. The second category is one-dimensional (1-D) nanostructures; in this group structures can grow in one dimension but are confined in other dimensions. Nanotubes, nanorods, and nanowires are examples of 1-D nanostructures. The third category is two-dimensional (2-D) nanostructures; structures in this group can grow in two dimensions and nanofilms, nanosheets, and nanoplates belong to this group (Figure 1.3).[13]

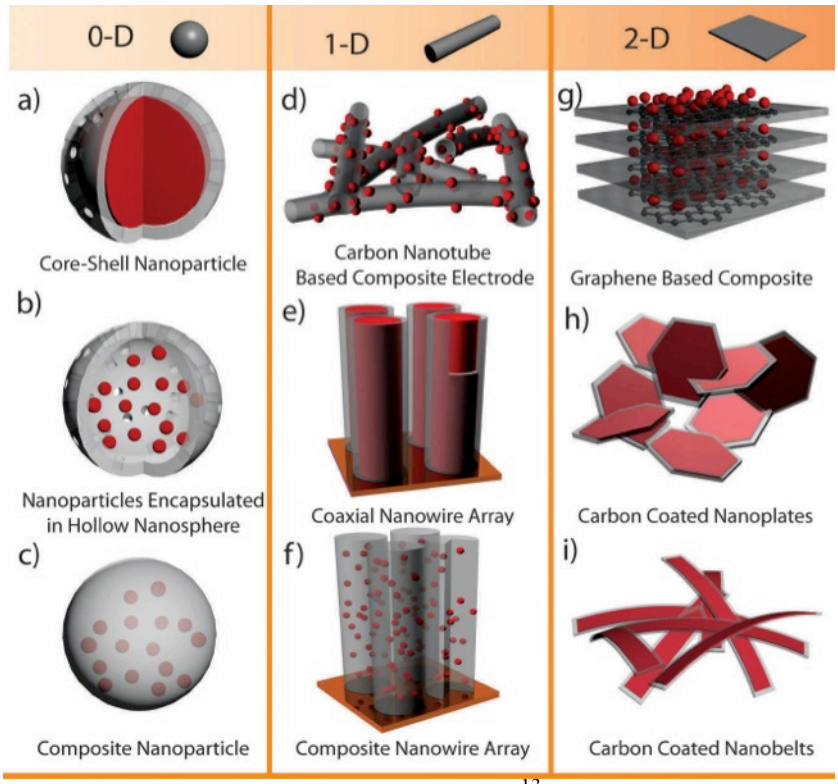

Figure 1.3: Different morphology of nanoastructures.[13]

Zero-dimension nanostructures such as quantum dots are known to be semiconductors and can exhibit a quantum effect when the diameter is considerably small. Quantum dots were predicted to exist in the 1970's but were not produced in a laboratory until the 1980's. On the other hand, 1-D nanostructures such as carbon tubes with a diameter of 5μm have been around since 1960.[14] Both 1-D and 2-D carbon nanostructures were studied in detail for their potential applications (Figure 1.4).[15]

Figure 1.4: Carbon nanostructures.[15]

1.4 Synthesis of Nanostructures

Nanomaterials are generally synthesized using two approaches: top-down and bottom-up (Figure 1.5). Top-down synthesis starts from bulk materials that undergo physical or mechanical alteration to produce nanomaterials. Ball milling and lithography are considered as top-down syntheses. These techniques typically produce nanostructures containing a significant amount of defects. In addition, the scope of production of materials with a small range of size and shape is limited; consequently, many researchers do not favor the top-down method.

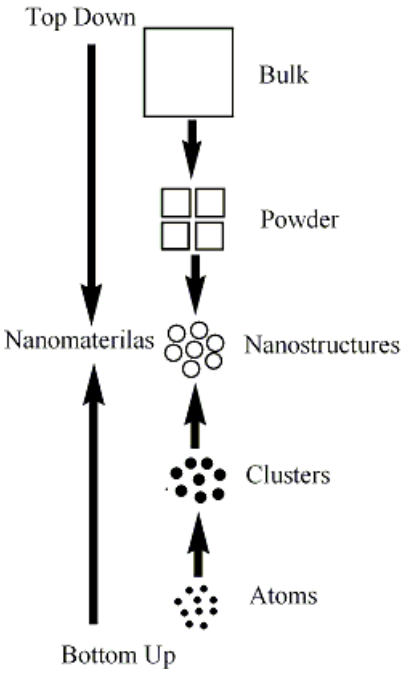

Figure 1.5: Top-down and bottom-up synthesis of nanostructures.

Bottom-up is a synthetic approach for building nanostructures atom by atom with fewer defects. This approach allows structures to have a similar size, shape, morphology or chemical composition and prevents agglomeration. Chemical synthesis using sol-gel processing, physical vapor deposition, chemical vapor deposition (CVD), atomic layer deposition, laser ablation and pyrolysis are all considered bottom-up approaches. Moreover, these methods can be designed to produce different morphologies by simply changing one or more of the experimental parameters.

1.5 Application of Nanomaterials

Discovery of instruments that help researchers study and understand nanomaterials opened a large window into untouched territory of the field. In addition, innovations to manipulate structures and materials for specific purposes allow researchers to explore a wide variety of applications. For example, in electronics carbon nanotubes have been used as a transistor for

very large-scale integration.[16-20] Additionally, many organic reactions use nanocatalysts for synthesis of specific products.[21-25] Nanomaterials are also applied in other fields such as energy,[26-28] construction,[29-31] biomedicine,[32-35] cosmetics, textiles, coatings and paints.[36] For biomedical applications in particular, nanomaterials are now being utilized to detect, image, deliver drugs, and monitor diseases. Among different nanomaterials, the carbon-based nanomaterials, such as carbon nanotubes,[37] fullerene[38] and graphene,[37] are being extensively investigated for their application in drug delivery, contrast agents, and cancer therapy. In addition, gold[39] and iron oxide nanoparticles[40] have also been studied for potential application in cancer therapy. Moreover, it has been recently reported that fluorescent silica nanoparticles containing vascular endothelial growth factor can be used for the treatment of isochemic.[41] In conclusion, nanomaterials and nanotechnology not only benefit us in our day-to-day life for diagnosis of diseases but also by producing materials that are durable and environmentally advantageous to our earth.

The research discussed in this dissertation focuses on synthesis and characterization of boron-based 0-D nanostructures (core/shell and nanoparticles) and 1-D nanostructures (nanorods) as well as zinc sulfide nanomaterials with the majority of the research done on boron-based nanomaterials. The main goal of the research is to prepare a biocompatible boron-containing nanostructures for boron neutron capture therapy (BNCT).

Boron-containing nanomaterials are chosen as a boron source for BNCT because the nanodimensions provide multiple advantages. First, these nanomaterials have the capacity to carry many boron atoms, while maintaining nanodimensions. When compared to other bulky organic boron sources such as boronophenylalanine (BPA), which only contains a single boron atom, these boron-based nanomaterials can have a large number of atoms depending on the

diameter of the nanostructure. Consequently, the dosing requirement will be lower since a small amount can attain the necessary level of boron concentration. Second, nanomaterials can pass through the blood brain barrier (BBB), which makes the delivery of drugs into the brain much easier. Considering these benefits, boron-containing nanomaterials were investigated.

The three boron-containing nanomaterials that have been studied are boron/iron oxide core/shell nanoparticles, boron/silica core/shell nanoparticles, and boron nanorods. Knowing boron's limit susceptibility for functionalization, a core/shell structure was proposed in order to gain the ability for surface modification.

1.6 Boron

Boron is the fifth element of the periodic table with three valance electrons and was discovered in 1808 by Joseph Louis Gay-Lussac, Louis Jacques Thenard, and Humphry Davy. However, the first compound discovered was not pure elemental boron.[42] Pure boron was processed a century later by Ezekiel Weintraub.[43] Boron has a high boiling point (2076°C) and is the second hardest element following diamond allotrope of carbon with a Vickers hardness value of 5000 HV. Boron has more than 13 isotopes, but only two of those are stable. The two stable isotopes are B-10 (^{10}B) with an abundance of 19.9% and B-11 (^{11}B) with 79.9%. Crystalline boron can have multiple allotropes but only a few of them, namely α-rhombohedral, β-rhombohedral, and α-tetragonal, have been studied intensively. Furthermore, each allotrope contains a different number of boron atoms per unit cell; for example. α-rhombohedral is composed of 12 boron atom, while β-rhombohedral consists of 105 boron atoms.[44] For humans, a small quantity (1-13 mg/day) of boron in the dietary supply is required and the two major sources in food are milk and coffee.[45] Boron-based nanomaterials can be utilized for high-

temperature semiconductor devices,[46] semiconductor dopant for n-type and p-type doping, rocket propellant mixtures,[47] biomedical applications and to increase the strength of construction materials such as ceramic.

1.6.1 Biomedical Application of Boron

In the biomedical field, boron-containing compounds are the ideal candidate for BNCT. BNCT is a treatment that uses ^{10}B isotope to absorb thermal neutron to become ^{11}B; however, the artificially made ^{11}B has a lifetime of 10^{-12} sec. This unstable ^{11}B nuclei undergoes a nuclear fission reaction to form α-particle, lithium ion, and produces energy of 2.79 MeV (Figure 1.6).[48,49] The energy created during the nuclear reaction can destroy any cell within 5-9 μm, that is the same as the diameter of a single cell; therefore, the process only damages cells containing boron without affecting the surrounding cells. This treatment is currently being used for many different types of cancer, including glioblastoma multiforme (GBM) and melanoma.

$$^{10}B + n_{th} \rightarrow [^{11}B] \rightarrow {}^{4}He + {}^{7}Li + 2.79\ MeV\ (6\%)$$

$$^{10}B + n_{th} \rightarrow [^{11}B] \rightarrow {}^{4}He + {}^{7}Li + 2.31\ MeV + \gamma\ (0.48MeV)\ (94\%)$$

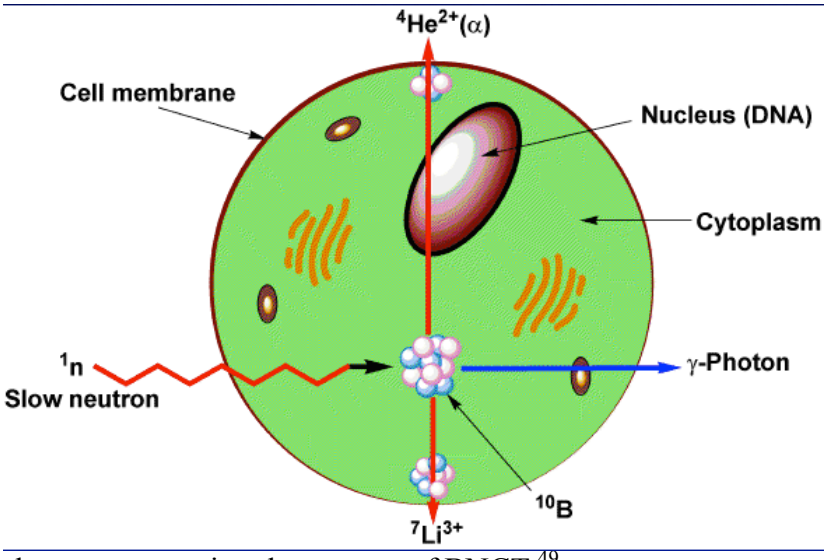

Figure 1.6: Scheme representing the process of BNCT.[49]

The basis for BNCT originated with the discovery of neutrons in 1932 by James Chadwick; afterwards G.L Locher in 1936 theorized ^{10}B could be used for cancer treatment. Boron, particularly its ^{10}B isotope, is the ideal candidate for neutron capture therapy because of its high neutron cross-section area compared to ^{11}B and other elements (Figure 1.7).[50] The large neutron cross-section area (3,800 barn) increases the probability of neutrons being captured, leading to the fission reaction.

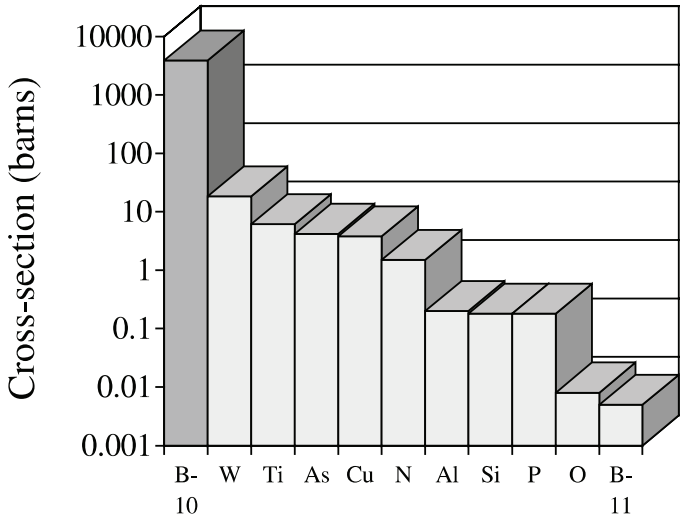

Figure 1.7: Chart containing neutron absorption cross-section area of multiple elements as well as the two isotopes of boron.[50]

In 1951, W. H. Sweet suggested the use of this therapy for brain tumors and a few years later the first trial was conducted at Massachusetts General Hospital and Brookhaven National Laboratory. The first trial used borax as a boron source, but there was no evidence of cure or improvement of the patients; as a matter of fact, the patients experienced severe side effects after the irradiation process. Even though the first trial ended with disappointing results, researchers still continued working to improve the process and finally in the 1960's trials performed in Japan

demonstrated the success of BNCT. The victory in Japan's trials can be attributed to the use of sodium mercaptoundecahydrododecaborate ($Na_2B_{12}H_{11}SH$), one of the two clinically approved boron delivery agents.[51] To be a successful boron delivery agent, the boron-containing compounds should have low toxicity and low concentration in normal cells while having high tumor uptake and high tumor concentration around 35 μg/g of tissue (10^9 ^{10}B atoms). The faster removal from the blood and normal tissue and persistence in tumor during irradiation are also the major key factors for a compound to succeed.[50] Currently there are two BNCT agents that are used in clinical trials, which are boronophenylalanine (BPA) and sodium mercaptoundecahydrododecaborate (BSH). However, these compounds are not tumor specific and deliver a low dosage of ^{10}B, thus requiring a larger dose to be administered in order to destroy the cancer cells. Furthermore, BSH can result in high concentrations of ^{10}B in the blood compared to tumor cells.[52,53] Consequently, there is an enormous demand for synthesis of tumor-specific BNCT agents with high boron content.

1.6.2 Zero-Dimension Boron Nanostructures

Structures such as nanoparticles, core/shell nanoparticles, and quantum dots are considered 0-D nanostructures. Quantum dots are mostly made of metal alloys with a matching lattice constant and can emit light in the visible spectra region. However, the color that is observed is dependent on the particle size. Zero-dimension nanoparticles have been widely explored for optics,[54] solar cells,[55,56] imaging,[57] and detection of diseases.[54,57]

1.6.3 Synthesis of Boron Nanoparticles

Boron nanoparticles can be synthesized using different methods, such as CVD, thermal plasma, solution reduction, ball milling, and pyrolysis. Different approaches in the synthesis process produce different structures with specific size distribution and purity.

CVD is a vapor transport process that uses the gaseous form of the starting materials, which is then deposited on a substrate. This process is a bottom-up approach for the synthesis of boron nanoparticles. The starting materials are usually inorganic compounds that contain boron, such as boron trichloride, boron tribromide, and boron trifluoride. These gases are transported to a furnace that is maintained at elevated temperature with argon or hydrogen as a carrier gas. Once the boron-containing gas reaches the furnace, it decomposes to produce boron nanoparticles. He and coworkers used boron tribromide gas as a boron source to synthesize α-rhombohedral boron nanoparticles at 900°C (Figure 1.8).[58] The α-rhombohedral boron nanoparticles were deposited on a boron-doped silica substrate; the substrate helped the formation of the structure at a lower temperature compared to other non-boron-containing substrates.[58] CVD has been the main synthesis route to produce boron nanoparticles with uniform morphology and size distribution. However, the major disadvantages associated with the CVD process include high temperature requirement, the need for stable substrates at a high temperature, uses of toxic gases as a starting material, and release of toxic by-products.

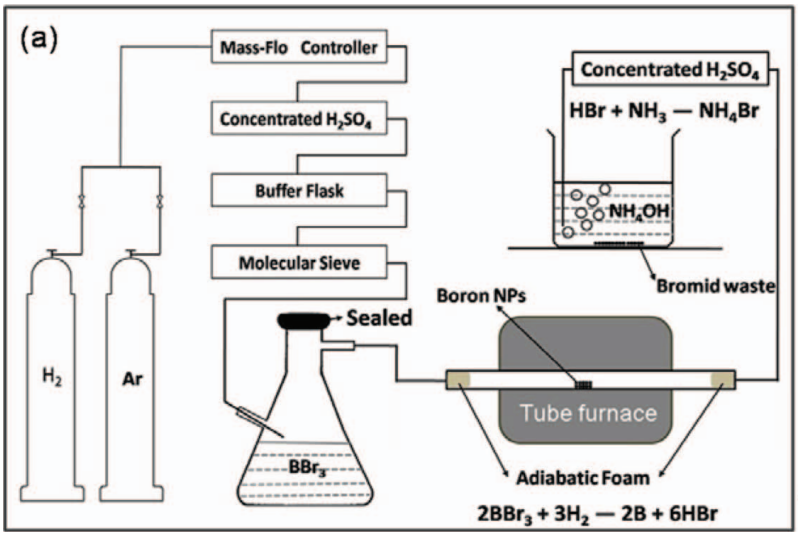

Figure 1.8: Illustration of CVD process to synthesize boron nanoparticles.[58]

Pyrolysis is a similar technique to CVD, except for the fact that it does not require a substrate for the deposition of the product. Bellott and coworkers successfully synthesized boron nanoparticles using decaborane as a boron source for pyrolysis.[59] Decaborane was sublimed and carried by argon gas to a furnace heated at 700°C or 900°C. Boron nanoparticles that were recovered from the reaction were α-rhombohedral in nature with size ranging between 10-150 nm. Unfortunately, the product contained a small amount of oxygen contamination.

Ball milling is another approach used to fabricate boron nanoparticles by physically breaking bulk starting materials into nanomaterials using balls made of tungsten carbide or other heavy metals. In this process, the starting material must have the same chemical composition as the target product, since there is no chemical reaction involved that can alter the chemical identity of the starting material. Particles produced via this route are pyrophoric and tend to oxidize upon air exposure; therefore, the introduction of these particles to air requires special handling. However, the milling process can be done in the presence of organic compounds, which will functionalize the surface of the particles and prevent oxidation. Perez et al.

synthesized boron nanoparticles with narrow size distribution of highly pure boron powder with a diameter of 2 μm.[60] The boron powder was ball milled in oleic acid and the resulting nanoparticles were covered with organic groups. Consequently, ball milling can accomplish synthesis and functionalization of boron nanoparticles in one step.

Arc discharge uses two electrodes with constant or alternating current supply to decompose boron-containing gases at reduced pressure. During this process, high temperature creates plasma, which then disintegrates the chemical bonds of the precursor gas to form the intended product. The temperature of the plasma could reach as high as 7000 K. Si et al. reported synthesis of boron nanoparticles via arc discharge of diborane gas.[61] The system used tungsten as the cathode and iron as the anode with a current of 20 amperes. The resulting nanoparticles were amorphous boron and had a diameter between 50-95 nm.

1.6.4 One-Dimension Boron Nanostructures

Zero-dimension boron nanostructures include nanorods, nanowires, nanotubes, nanobelts, and nanoribbons. Synthesis and application of 1-D boron-based nanostructures are not well developed yet. In some cases, like boron nanotubes, the physical properties are not completely known, but they are predicted to be metals and semiconductors depending on their crystalline allotrope. To date, 1-D boron-based nanostructures are synthesized using CVD, thermal reduction, magnetic sputtering and laser ablation. These nanostructures can be used for electric transport, field emission and biomedical application.[62]

1.6.5 Synthesis of Boron Nanorods

Boron nanorods can be synthesized in various methods and we will discuss a few of them in this section.

Zhu and Kisi synthesized boron nanorods by annealing boron powder.[63] First, boron powder was ball milled for an extended period of time under an inert atmosphere. Next, the powder was annealed in an aluminum boat inside a furnace. The annealing process was performed under a nitrogen atmosphere for five hours (h) at 1200°C. The product was characterized using transmission electron microscopy (TEM), scanning electron microscopy (SEM), energy-dispersive X-ray spectroscopy (EDX) and X-ray diffraction (XRD). TEM displays amorphous structures and nanorods with a diameter between 50-250 nm (Figure 1.9). XRD and EDX indicate the presence of contamination such as iron that came from the steel ball during the milling process.

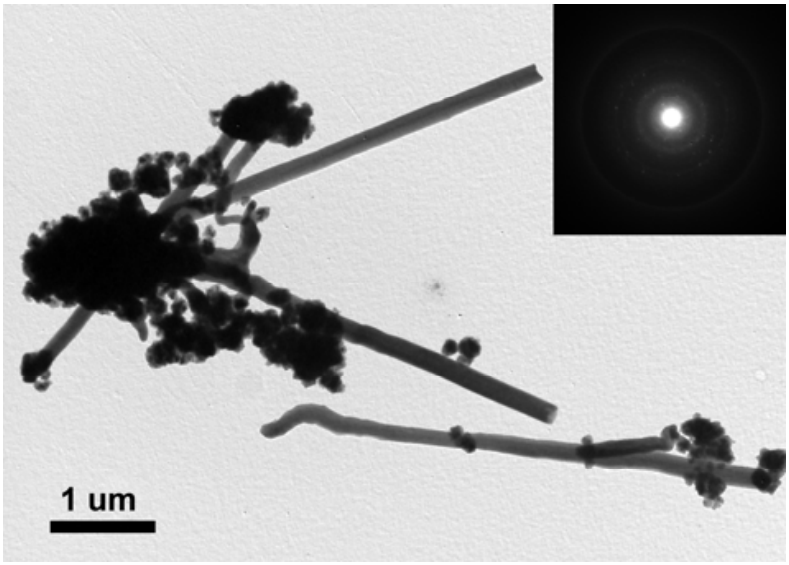

Figure 1.9: TEM image of the product containing boron nanorods and other amorphous structure.[63]

In 2006, Yang et al. produced boron nanorods without any contamination using the CVD technique.[64] This procedure allowed the synthesis process to be done at a lower temperature compared to the annealing temperature of 1200°C used by Zhu and Kisi. CVD was done in a furnace heated to 700-950°C with a mixture of argon, hydrogen and diborane passing through the furnace and the decomposed gas was deposited on a silica wafer coated with aluminum film (Figure 1.10).

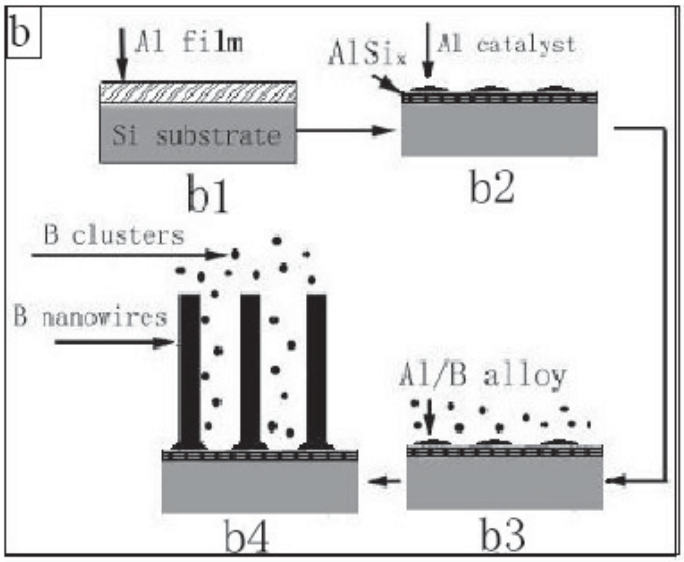

Figure 1.10: Scheme showing the formation of boron nanorods via CVD.[64]

The TEM result shows nanorods with a diameter of 20-50 nm without any contamination. Furthermore, a temperature between 800-900°C formed the intended product with excellent size distribution.

Chakrabarti et al. reduced boron oxide by using molten lithium to synthesize boron nanorods.[65] This novel method uses a significantly low temperature and avoids toxic starting

materials. The procedure includes melting lithium metal followed by adding boron oxide. Boron oxide and molten lithium are mixed using ultra sonication, and then the temperature is elevated to 250°C for two hours (Figure 1.11).

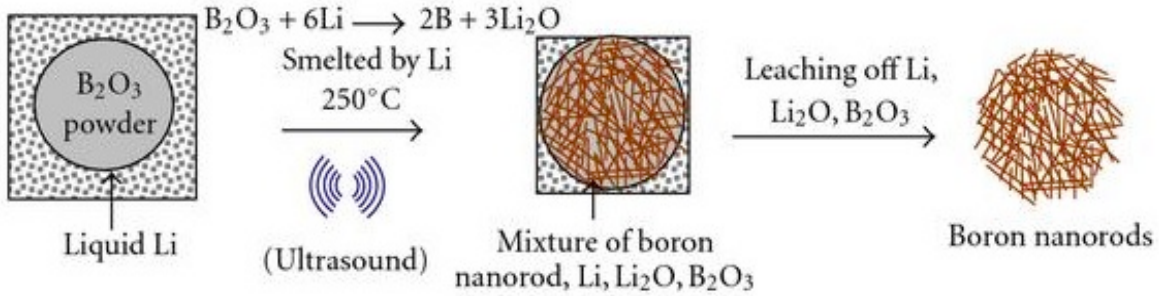

Figure 1.11: Scheme showing the synthesis of boron nanorods via reduction.[65]

The resulting nanorods are stable under argon and air up to 550°C and have a diameter between 20-40 nm. Furthermore, EDX characterization verifies the purity of the sample. However, the final product contains a mixture of boron nanorods and boron nanoparticles (Figure 1.12), requiring an improvement of the synthesis procedure to produce only nanorods.

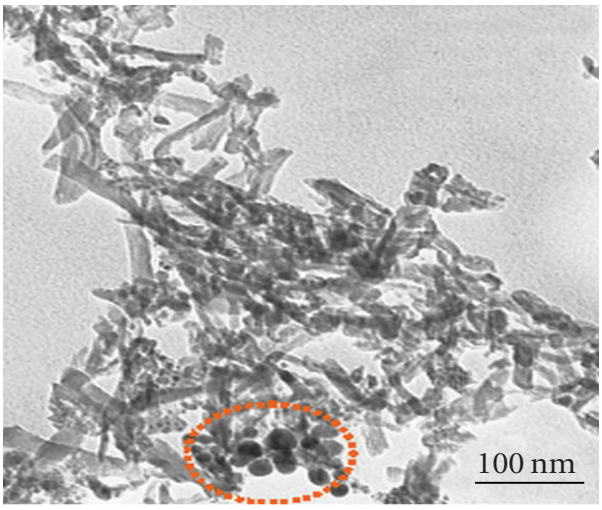

Figure 1.12: TEM image of the final product containing boron nanorods and boron nanoparticles.[65]

1.7 Core/Shell Nanostructures

Core/shell structures are 0-D nanostructures that are composed of two distinct layers. Each layer has its own chemical identity that complements the other to amplify or weaken certain characteristics. Further, each layer can be composed of organic or inorganic materials. In other words, core/shell structures can have organic/organic, organic/inorganic, inorganic/organic, and inorganic/inorganic compositions. Each of these pairs can be used to modify optical, catalytic, magnetic, and electronic properties as well as to stabilize the nanoparticle core. Figure 1.13[66] shows the different morphologies that core/shell structures can obtain, including spheres. The core/shell structure can be composed of an amorphous core and shell, a crystalline core and shell, or one of each. Additionally, the core and shell may have a similar lattice constant or a lattice constant that is significantly different. The case that has both crystalline structures with a comparable lattice constant increases the probability of shell growth as an extension of the core.

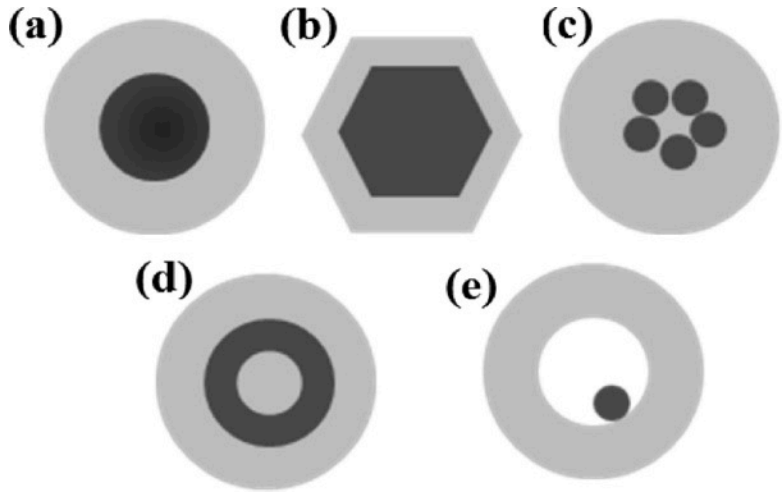

Figure 1.13: Illustration of different core/shell morphologies.[66]

When core/shell nanostructures are prepared initially the core is formed followed by the shell. The two steps can be performed separately or combined as one-pot synthesis.[67] One-pot synthesis can save time and chemicals by eliminating the purification of the core nanostructure, but it can lead to other unwanted side reactions.

References

1. Faynman, R.; There is plenty of room at the bottom. *Engineering and Science,* **1960**, 23:5, 22-36.

2. Drexler, K.E., Engines of Creation; The Coming Era of Nanotechnology. 1986, New York, New York: Anchor Books. 298.

3. Tolochko, N. K.; *History of Nanotechnology.* Nanoscience and Nanotechnologies. Encyclopedia *of Life Support Systems* (EOLSS).

4. National Nanotechnology Initiative. Nanotechnology Timeline: Premodern examples of nanotechnology. http://www.nano.gov/timeline (accessed July 20, 2015).

5. Chemical Heritage Magazine. From nanotech to nanoscience. http://www.chemheritage.org/discover/media/magazine/articles/26-2-from-nanotech-to-nanoscience.aspx (accessed July 20, 2015).

6. Allan, R., *A brief history of telemedicine*. Electronic Design, 2006

7. National Nanotechnology Initiative. Frequently asked questions: Where is nanotechnology used today. http://www.nano.gov/nanotech-101/nanotechnology-facts (accessed July 20, 2015).

8. National Nanotechnology Initiative. Nanotechnology Timeline: Examples of discoveries and developments enabling nanotechnology in the modern era. http://www.nano.gov/timeline (accessed May 1, 2015) .

9. Ye, X.; Jin, L.; Caglayan, H.; Chen, J.; Xing, G.; Zheng, C.; Doan-Nguyen, V.; Kang Y.; Engheta, N.; Kagen, C.; Murray, C. B., Improved Size-Tunable Synthesis of Monodisperse Gold Nanorods through The Use of Aromatic Additives. *ACS Nano,* **2012**, 6, 2804−2817.

10. Landry, M.; Morrell, T.; Karagounis, T.; Hsia, C.; Wang, C. Simple Syntheses Of Cdse Quantum Dots. *J. Chem. Educ.* **2014**, 91, 274-279.

11. Jiang, H.; Moon, K-S.; Dong, H.; Hua, F.; Wong, C. P., Size-dependent melting properties of tin nanoparticles. *Chem. Phys. Lett.*, **2006**, 429, 4-6**,** 492–496.

12. Cao, G.; Wang, Y., Nanostructures and Nanomaterials, synthesis, properties, and applications, 2nd ed.; World Scientific, 2011;pp 19-23.

13. Ran Liu's Research. Hestrogenious Nanostructured Materials with Different morphologies. The Pennsylvania State University. 2011. http://research.chem.psu.edu/axsgroup/Ran/research/energystorage.html (accessed July 21, 2015).

14. Shenderova, O. A.; Zhirnov, V. V.; Brenner, D. W.; **Carbon Nanostructures.** *Critical Reviews in Solid State and Materials Sciences,* 2002, 27, 227–356.

15. Mauter, M. S.; Elimelech, M., Environmental applications of carbon-based nanomaterials. *Environmental Science & Technology* **2008,** *42*, 5843-5859.

16. Bsiesy, A.; Muller, F.; Ligeon, M.; Gaspard, F.; Herino, R.; Romestain, R.; Vial. J.C., Voltage-Controlled Spectral Shift of Porous Silicon Electroluminescence*Phys. Rev. Lett.* **1993**, 71, 637-640.

17. Jalali, B.; Fathpour, S., Silicon Photonics. *J. Lightw. Technol.*, **2006**, *24*, 4600-4615.

18. Zhang, J.; Lin, A.; Patil, N.; Wei, H.; Wei, L.; Wong, H.-S. P.; Mitra, S., Robust Digital VLSI using Carbon Nanotubes. *IEEE Trans. Comput.-Aided Design Integr. Circuits Syst.,* **2012**, *31*, 453-471.

19. Jin, L.; Fang, Y.; Wen, D.; Wang, L.; Wang, E.; Dong, S., Reversibly Electroswitched Quantum Dot Luminescence in Aqueous Solution. *ACS Nano,* **2011***, 5*, 5249-5253.

20. Zorn, M.; Bae, W. K.; Kwak, J.; Lee, H.; Lee, C.; Zentel, R.; Char, K., Quantum Dot-Block Copolymer Hybrids with Improved Properties and Their Application to Quantum Dot Light-Emitting Devices. *ACS Nano,* **2009***, 3*, 1063–1068.

21. Ohtaka, A.; Teratani, T.; Fujii, R.; Ikeshita, K.; Kawashima, T.; Tatsumi, K.; Shimomura, O.; Nomura, R., Linear Polystyrene-Stabilized Palladium Nanoparticles-Catalyzed C-C Coupling Reaction in Water. *J. Org. Chem.* **2011,** 76, 4052–4060**.**

22. Salam, N.; Kundu, S.; Roy, A. S.; Mondal, P.; Roy, S.; Bhaumik, A.; Islam, S. M., Cu-grafted mesoporous organic polymer: A new recyclable nanocatalyst for multi-component, N-arylation and S-arylation reactions. *Catal. Sci. Technol.*, **2013**, 3, 3303-3316.

23. Hu, Y.; Tao, K.; Wu, C.; Zhou, C.; Yin, H.; Zhou, S., Size-Controlled Synthesis of Highly Stable and Active Pd@SiO2 Core−Shell Nanocatalysts for Hydrogenation of Nitrobenzene. *J. Phys. Chem. C*, **2013**, *117*, 8974−8982.

24. Violi, I. L.; Zelcer, A.; Bruno, M. M.; Luca, V.; Soler-Illia, G., Gold Nanoparticles Supported in Zirconia−Ceria Mesoporous Thin Films: A Highly Active Reusable Heterogeneous Nanocatalyst. *ACS Appl. Mater. Interfaces,* **2015**, *7*, 1114−1121.

25. Polshettiwar, V.; Baruwati, B.; Varma, R. S., Assembly of Metal Oxides into Three-Dimensional Nanostructures: Synthesis and Application in Catalysis. *ACS Nano*, **2009**, *3*, 728–736.

26. Jadhav, P. J.; Mohanty, A.; Sussman, J.; Lee, J.; Baldo, M. A., Singlet Exciton Fission in Nanostructured Organic Solar Cells. *Nano Lett.* **2011**, *11*, 1495–1498

27. MacDonald, B. I.; Martucci, A.; Rubanov, S.; Watkins, S. E.; Mulvaney, P.; Jasieniak, J. J., Layer-by-Layer Assembly of Sintered $CdSe_xTe_{1-x}$ Nanocrystal Solar Cells. *ACS Nano*, **2012,** *6*, 5995–6004.

28. Li, Y.; Yang, R. T., Hydrogen Storage in Low Silica Type X Zeolites. *J. Phys. Chem. B,* **2006,** *110,* 17175-17181.

29. Flores-Vivian, I.; Pradoto, R.G.K.; Moini, M.; Sobolev, K. The Use Of Nanoparticles To Improve The Performance of Concrete**.** *NANOCON 2013*, Brno, Czech Republic, EU, October 16-18, 2013, 5th International Conference on Nanomaterials.

30. Mondal, P.; Shah, S.P.; Marks, L.D.; Gaitero, J.J., Comparative Study of the Effects of Microsilica and Nanosilica in Concrete. *Transportation Research Board*, **2010**, *2141*, 6-9.

31. Wanga, R.; Wanga, B.; Hea, Y.; Lva , W.; Wang, J., Preparation of composited Nano-TiO2 and its application on antimicrobial and self-cleaning coatings. *Polym. Adv. Technol.* **2010**, *21*, 331–336.

32. Singh, M.; Singh, S.; Prasad, S.; Gambhir, I.S., Nanotechnology In Medicine And Antibacterial Effect of Silver Nanoparticles. *Dig. J. Nanomater. Bios.* **2008**, *3*, 115-122.

33. Patil, M.; Mehta, D.S.; Guvva, S., Future impact of nanotechnology on medicine and dentistry. *J Indian Soc. Periodontol*. **2008**, *12*, 34–40.

34. Shi, J.; Votruba, A.R.; Farokhzad, O.C.; Langer, R., Nanotechnology in Drug Delivery and Tissue Engineering: From Discovery to Applications. *Nano Lett.* **2010,** *10,* 3223–3230.

35. Farokhzad, O.C.; Langer, R., Impact of Nanotechnology on Drug. *ACS Nano*, **2009**, *3*, 16–20.

36. Lövestam, G.; Rauscher, H.; Roebben, G.; Klüttgen, B. S.; Gibson, N.; Putaud, J-P.; Stamm, H.; Considerations on a Definition of Nanomaterial for Regulatory Purposes. *JRC Reference Reports*, European Union, **2010**, EUR 24403 EN.

37. Monaco1, A.M.; Giugliano, M., Carbon-Based Smart Nanomaterials In Biomedicine and Neuroengineering. *Beilstein J. Nanotechnol.* **2014**, *5*, 1849–1863.

38. Partha, R.; Conyers, J.L., Biomedical applications of functionalized fullerene-based nanomaterials. *Int. J. Nanomedicine*, **2009**, *4*, 261–275.

39. Popovtzer, R., Biomedical Applications Of Gold Nanomaterials. *Nanomedicine (Lond.)* **2014**, 9, 1903–1904.

40. Wang, B.; Yin, J.; Zhou, X.; Kurash, I.; Chai, Z.; Zhao, Y.; Feng, W., Physicochemical Origin for Free Radical Generation of Iron Oxide Nanoparticles in Biomicroenvironment: Catalytic Activities Mediated by Surface Chemical States. *J. Phys. Chem. C* **2013**, *117,* 383-392.

41. Kim, J.; Cao, L.; Shvartsman, D.; Silva, E.A.; Mooney, D.J., Targeted Delivery Of Nanoparticles To Ischemic Muscle For Imaging And Therapeutic Angiogenesis. *Nano Lett.* **2011**, *11*, 694–700.

42. Oganov, A. R., Solozhenko, V. L., Boron: a Hunt for Superhard Polymorphs, *J. Superhard Mater.,* 2009, 31, (5), 285-291.

43. Weintraub, E., Preparation and properties of pure boron. *Transactions of the American Electrochemical Society*, **1910***,* 16, 165–184.

44. Setten, M.J., Uijttewaal, M.A., de Wijs, G. A., de Groot, R. A., Thermodynamic Stability of Boron: The Role of Defects and Zero Point Motion. ***J.** Am. Chem. Soc.* **2007,** 129, 2458-2465.

45. Samman, S.; Foster, M.; Hunter, D. In Boron Science: *New Technologies & Applications*; Hosmane, N. S., Ed.; CRC Press: Boca Raton, FL, 2011, Chapt. 4, 73-90.

46. Cao, L.; Zhang, X.; Wang, W.; Feng, M., Stoichiometric Boron-Based Nanostructures. *Stoichiometry and Materials Science - When Numbers Matter* InTech, China, 2012; pp 25-46.

47. He, X.: Joo, S.: Liang, H., Boron-Based Nanoparticles for Chemical-Mechanical Polishing of Copper Films. *ECS Journal of Solid State Science and Technology,* **2013**, 2 (1), 20-25.

48. Alotiby, M., Boron Neutron Capture Therapy for Cancer Treatments. M.S. Dissertation, University of Surrey, 2012.

49. Zhu, Y.; Maguire, J. A.; Hosmane, N. S. In Boron Science: *New Technologies & Applications*; Hosmane, N. S., Ed.; CRC Press: Boca Raton, FL, 2011, Chapt. 7, 147-149.

50. Baumann, R.C; Smith, E.B; Neutron-induced ^{10}B fission as a major source of soft errors in high density SRAMs. *Microelectronics Reliability*, **2001**, 41, 211-218

51. Farr, L.E.; Sweet, W.H.; Robertson, J.S.; Foster, C.G.; Locksley, H.B.; Sutherland, D.L.; Mendelsohn, M.L.; Stickley, E.E., Neutron capture therapy with boron in the treatment of glioblastoma multiforme. *Am. J. Roentgenol. Radium. Ther. Nucl. Med.,* **1954**, 71, 2, 279–293.

52. Hosmane, N. S.; Maguire, J. A.; Zhu, Y.; Takagaki, M. *Boron and Gadolinium Neutron Capture Therapy for Cancer Treatment*, World Scientific Publishers: Hackensack, NJ, USA, 2012.

53. Coderre, J. A.; Turcotte, J. C.; Riley, K. J.; Binns, P. J.; Harling, O. K.; Kiger, W. S., Boron Neutron Capture Therapy: Cellular Targeting of High Linear Energy Transfer Radiation. *Technol. Cancer Res. Treat.,* **2003**, 2, 5, 1-21.

54. Biju, V., Itoh, T., Anas , A., Sujith, A., Ishikawa, M., Semiconductor quantum dots and metal nanoparticles:syntheses, optical properties, and biological applications. *Anal. Bioanal. Chem.*, **2008**, 391, 2469–2495.

55. Nozik, A. J., Beard, M. C., Luther, J. M., Law, M., Ellingson, R. J., Johnson, J. C., Semiconductor Quantum Dots and Quantum Dot Arrays and Applications of Multiple Exciton Generation to Third-Generation Photovoltaic Solar Cells. *Chem. Rev.,* **2010**, 110, 6873–6890.

56. Nozik, A. J., Exciton Multiplication and Relaxation Dynamics in Quantum Dots: Applications to Ultrahigh-Efficiency Solar Photon Conversion. *Inorg. Chem.,* **2005**, 44, 6893−6899.

57. Michalet, X., Pinaud, F. F., Bentolila, L. A., Tsay, J. M., Doose, S., Li, J. J., Sundaresan, G., Wu, A. M., Gambhir, S. S., Weiss S., Quantum Dots for Live Cells, in Vivo Imaging, and Diagnostics. *Science*, **2005**, 307, 538-544.

58. He, X.: Joo, S.: Liang, H., Boron-Based Nanoparticles for Chemical-Mechanical Polishing of Copper Films. *ECS Journal of Solid State Science and Technology,* **2013**, 2 (1), 20-25.

59. Bellott, B. J.; Noh, W.; Nuzzo, R.G.; Girolami, G.S., Nanoenergetic materials: boron nanoparticles from the pyrolysis of decaborane and their functionalization. *Chem. Commun.,* **2009**, 3214–3215.

60. Perez, P.L.; McMahon, B.W.; Schneider, S.; Boatz, J.A.; Hawkins, T.W.; McCrary, P.D.; Beasley, P.A.; Kelley, S.P.; Rogers, R.D, Anderson, S.L., Exploring the Structure of Nitrogen-Rich Ionic Liquids and Their Binding to the Surface of Oxide-Free Boron Nanoparticles. *J. Phys. Chem. C,* **2013**, 117, 5693−5707.

61. Si, P. Z.; Zhang, M.; You, C. Y.; Geng, D. Y.; Du, J. H; Zhao, X. G.; Ma, X. L.; Zhang, Z. D., Amorphous boron nanoparticles and BN encapsulating boron nano-peanuts prepared by arc-decomposing diborane and nitriding. *J. Mater. Sci.* **2003,** 38, 689– 692.

62. Tian, J., Xu, Z., Shen, C., Liu, F., Xub, N., Gao, H-J., One-dimensional boron nanostructures: Prediction, synthesis, characterizations, and applications. *Nanoscale.*, **2010**, 2, 1375–1389.

63. Zhu, D.M.; Kisi, E., Synthesis and Characterization of Boron/Boron Oxide Nanorods. *J Aust. Ceram. Soc,*, **2009**, 45[2], 49-53.

64. Yang, Q.; Sha, J.; Wang, L.; Yuan, Z.; Yang D., Aligned single crystal Al-catalyzed boron nanorods on Si substrates. *Eur. Phys. J.* B, 2007, 56, 35–39.

65. Chakrabarti, A.; Xu, T.; Paulson, L. K.; Krise, K. J.; Maguire, J. A.; Hosmane, N. S., Synthesis of Boron Nanorods by Smelting Non-Toxic Boron Oxide in Liquid Lithium. *J. Nanomater*., **2010**, 589372.

66. Chaudhuri, R.G., Paria. S., Core/Shell Nanoparticles: Classes, Properties, Synthesis Mechanisms, Characterization, and Applications. *Chem. Rev.*, **2012**, 112, 2373–2433.

67. Gao, S.; Liu, X.; Xu, T.; Ma, X.; Shen, Z.; Wu, A.; Zhu, Y.; Hosmane, N.S; *ChemistryOpen* **2013**, 2, 88 – 92.

CHAPTER 2

INSTRUMENTATION

2.1 Introduction

In this chapter, the different instrumentations that were used to characterize the products will be discussed. The basic principles of the instruments will also be provided. In addition, we will cover sample preparation for instruments that require special handling. In order to characterize nanomaterials, instruments with high magnification are mandatory because of the products' small dimension. Some of these instruments are transmission electron microscopy and high-resolution transmission electron microscopy, which are used to identify the morphology of the products. Electron energy-loss spectroscopy, X-ray photoelectron spectroscopy, and energy-dispersive X-ray spectroscopy identify the chemical compositions of the nanomaterials. Additionally, Fourier-transform infrared spectroscopy, X-ray diffraction, and ultraviolet-visible spectroscopy will supply more structural and elemental information on the products. A few of these characterization methods will be described in detail.

2.2 Transmission Electron Microscopy[1,2]

Transmission electron microscope (TEM) is an instrument that allows the visual observation of the sample product. Both TEM and HRTEM work following a similar principle, except HRTEM has a higher magnification power that will allow the researchers to see

individual molecules. In this research, TEM was used to confirm the formation of nanostructures with specific morphology (particles or rods), and HRTEM allowed the researchers to see the formation of core/shell structures with two distinct layers.

A typical TEM (Figure 2.1) uses electrons generated from tungsten filament to bombard the sample surface. The sample should have a thickness less than 100 nm. The electrons are focused on the sample with the help of multiple condenser lenses. Once the beam reaches the sample, the interaction between electrons and the sample provides various information about the sample. During the interaction, if the electrons maintain their kinetic energy, a diffraction pattern is recovered and used for imaging. In contrast, if there is a loss in kinetic energy, there is a change in the intensity and scattering angle of the electrons, which leads to spectroscopy.

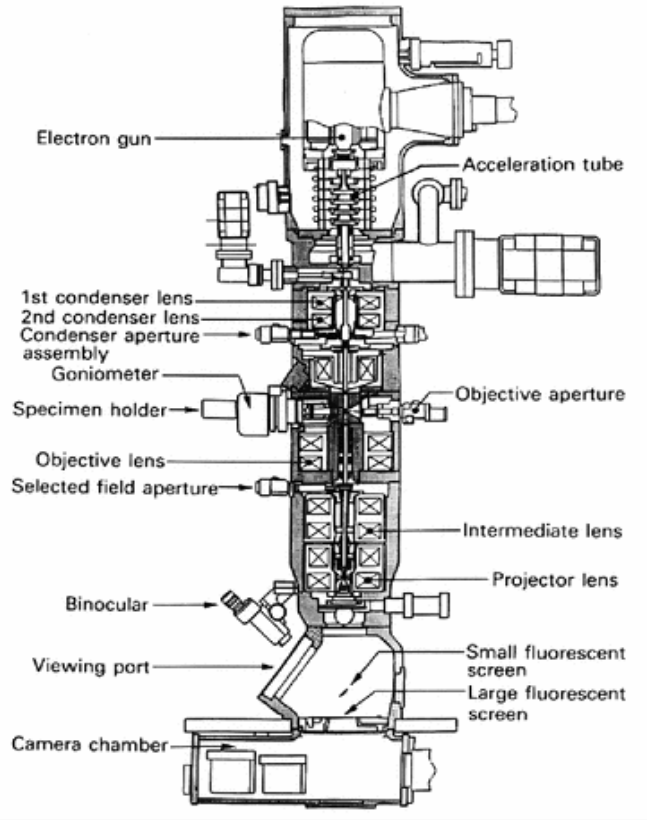

Figure 2.1: Schematic diagram of components of TEM.[1]

A typical TEM can be transformed to HRTEM using the basic principle of the de Broglie equation:

$$\lambda = \frac{h}{(2mqV)^{1/2}} \qquad \text{(Equation 2.1)}$$

where λ is wavelength, h is Planck's constant, m and q are the electron mass and charge and V is the voltage applied to the electrons. Based on this equation, the voltage applied is inversely proportional to the λ. Therefore, we can achieve shorter wavelength (λ) or higher resolution by increasing the voltage used to accelerate the electrons. Further, TEM equipped with a high voltage source can be utilized to establish the melting point and mechanical characteristics of nanomaterials.

For our research purpose, we used three different TEM, which are a Hitachi H-600, JEOL 2010, and FEI Tecnai F20 with acceleration energy of 200kv. All of the samples were prepared following a simple procedure. In a typical sample preparation, a small amount of the sample was placed in a vial to which subsequently ethanol was added. Then the solution was dispersed with a probe sonicator set at 60% amplitude for 2 minutes. Once the sonication was done, a drop of the solution was placed on a copper grid coated with carbon film, and the grid was left to dry in air. These steps were repeated two more times to accumulate a sufficient amount of the sample on the grid.

2.2.1 Electron Energy-Loss Spectroscopy[3,4]

Electron energy-loss spectroscopy (EELS) uses the energy released from electrons to identify the presence of elements. The analysis is done using high-resolution electron microscopy such as TEM or STEM. The use of high-resolution electron microscopy allows the arrangement of electrons based on kinetic energy and creates an EELS plot of scattered intensity

vs. kinetic energy. There are different designs of the TEM-EELS, which are shown in Figure 2.2. The sample preparation for EELS is identical to TEM sample preparation mentioned above.

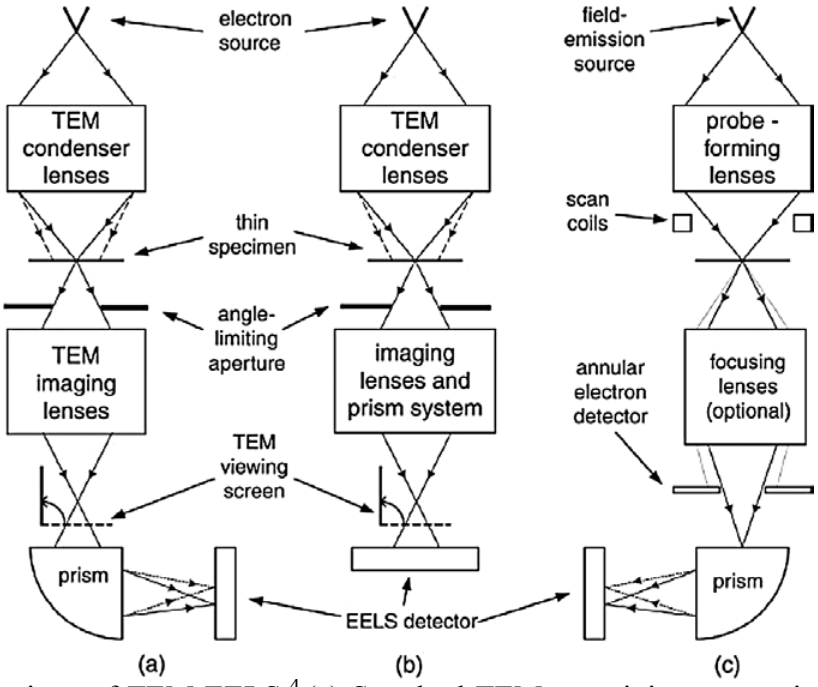

Figure 2.2: Designs of TEM-EELS.[4] (a) Standard TEM containing magnetic prism, (b) TEM containing an in-column imaging filter, and (c) scanning transmission electron microscopy (STEM).

2.2.2 High-Angle Annular Dark Field[5,6,7]

High-angle annular dark field (HAADF) or Z-contrast imaging utilizes high-angle scattering of electrons where θ is greater than 50 mrad to construct an image of crystalline or amorphous samples. A higher angle will not allow Bragg electrons to reach the detector; therefore, crystalline structures can be analyzed which would not be possible otherwise (Figure2.3). In addition, this method has the capacity to map a single element, usually heavier elements. The signal intensity is proportional to the atomic number, so a sample composed of

heavier elements will have an intense signal. HAADF is performed when the microscope is in STEM mode. The sample preparation is similar to TEM.

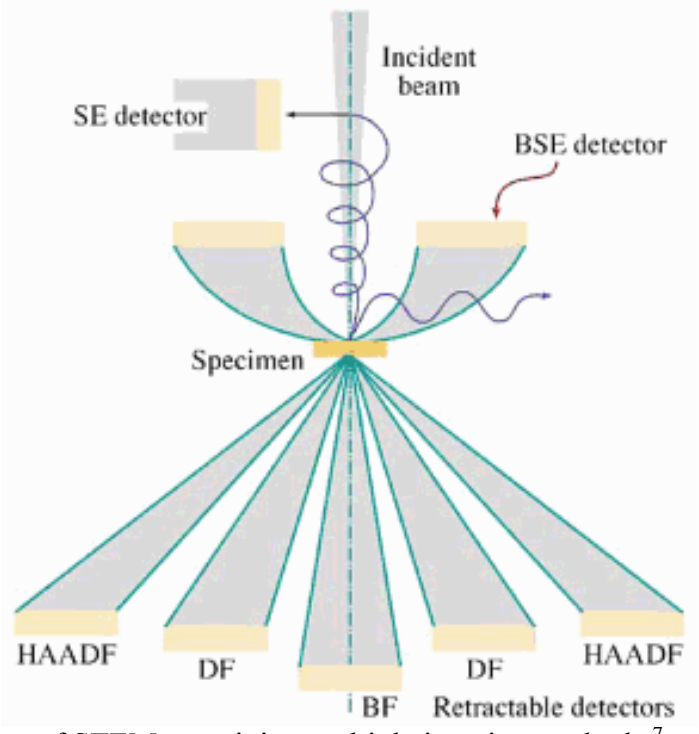

Figure 2.3: Diagram of STEM containing multiple imaging methods.[7]

2.3 X-ray diffraction[8,9]

X-ray diffraction (XRD) is a method used to identify if a sample is amorphous or crystalline. When the structure is crystalline, the X-ray diffracts from the sample and the diffraction pattern is used to resolve structure or geometry, lattice constants, chemical bonds, and defects of the crystalline material. Figure 2.4 demonstrates the formation of diffraction pattern by the radiation source that bounces off the atoms in the sample. The diffraction pattern is rich with

information, such as wavelength and reflection angle of the X-ray. However, this information does not provide a complete structural analysis until complex mathematical integration is done.

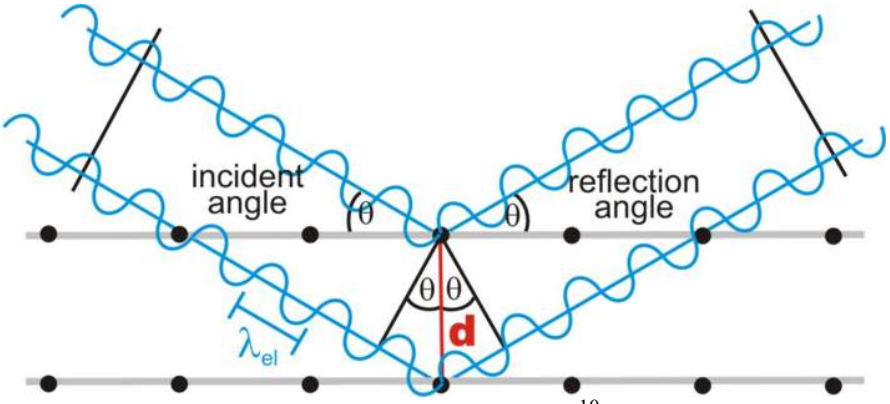

Figure 2.4: Illustration of XRD in crystalline structures.[10]

The atoms in the crystal lattice are placed layer by layer, and the distance between the layers can be calculated using Bragg's equation:

$$n\lambda = 2d \sin\theta \qquad \text{(Equation 2.2)}$$

where n is an integer, λ is wavelength, d is the distance between the layers, and θ is the reflection angle, which is also the same as the incident angle. Once all the parameters are determined, the crystal structure can be solved. Since the diffraction patterns are accurate, XRD can be used to analyze inhomogeneous and homogeneous strains. The presence of homogeneous strains changes the position of the diffraction peak while inhomogeneous strains broaden the peak.

XRD is a simple method with an easy sample preparation and produces an accurate analysis for high-Z materials. The system is composed of a low-intensity beam; therefore, the data are collected with a large sample and over an extended period of time. In our data collection, we used Rigaku MiniFlex (30 kV, 15 mA) fitted with Cu source procuring X-ray with 1.54°A wavelength. The instrument has six sample holders. Prior to each measurement, a sample

holder is covered with double-sided clear tape and the sample is placed on it. Then the holder is tapped to remove any loose samples before it is placed back on the instrument.

2.4 Energy-Dispersive X-ray Spectroscopy [11,12]

Energy-dispersive X-ray spectroscopy (EDX) is a quantitative analysis used to determine the chemical composition of a sample. The instruments utilize X-ray to excite atoms in a lower energy level. Furthermore, the excited electrons leave, creating a hole, and this hole is filled by an electron from the upper level. When an electron with a higher energy jumps to a level with lower energy, some of its initial energy is emitted in the form of an X-ray (Figure 2.5). Each atom or element has its own unique X-ray emission; therefore, the X-ray emitted during this process corresponds to a specific atom.

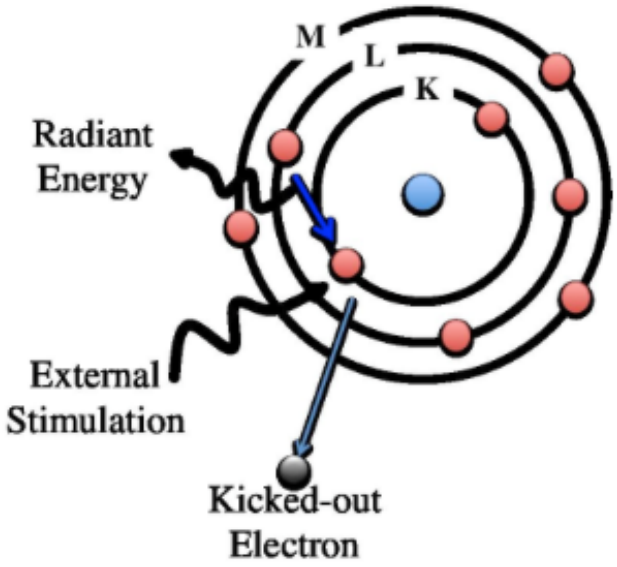

Figure 2.5: Illustration of the EDX process.[12]

This characterization technique has a few disadvantages including elements with a small atomic numbers not appearing, an overlap of energy peaks, and the presence of signals from the sample preparation (carbon tape).[13] All of these result in incorrect data interpretation. We used INCAX-act analytical standard EDX for elemental analysis of our samples. The samples are prepared by placing a small amount of the sample on a carbon tape that is attached to a holder. Then, the sample holder is tapped to remove any loose samples.

2.5 Fourier-Transform Infrared Spectroscopy[14,15,16]

Fourier-transform infrared spectroscopy (FTIR) is analysis of solid, liquid, or gas samples using infrared radiation, which is focused on a sample, and the radiation can be transmitted or absorbed by the sample. The radiation that is absorbed causes vibration or rotation of the molecules in the sample, and each molecule absorbs energy at a certain wavelength. Therefore, molecules are identified based on their characteristic wavelength. The data collected can be based on absorbance, transmittance, or photoconductivity of the sample.

There is also another type of IR called attenuated total reflectance (ATR). This instrument allows the users to analyze samples without any sample preparation. ATR has an optical crystal, and when the infrared radiation is focused on the crystal, it bounces within and on the surface of the crystal. Next, the radiation interacts with the sample leading to the absorption peak (Figure 2.6). In order to acquire accurate data, the sample should be placed within 0.5-5 μm of the crystal surface, and the reflective index of the sample should be much lower than the crystal. Many different kinds of crystals such as zinc selenide or germanium are available, but diamond crystal is preferable because it cannot be easily damaged. In our facility, we used a

Mattson ATI Genesis FTIR spectrometer with a Pike Miracle ATR attachment. The ATR has a diamond crystal, and the sample is directly placed on the crystal before analysis.

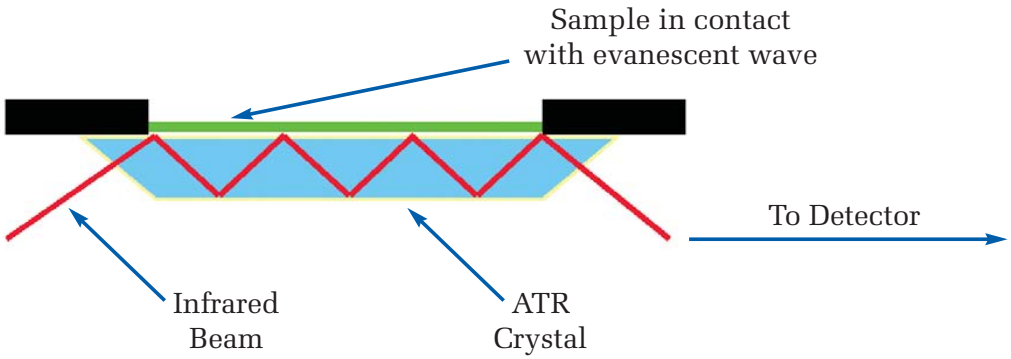

Figure 2.6: Diagram demonstrating the use of crystal in ATR instrument.[16]

2.6 Ultraviolet-Visible Spectroscopy (UV-Vis) [17,18]

This analytical method utilizes the fact that molecules absorb radiation to detect their presence. When radiation is absorbed by a sample, the electrons on the sample gain some energy and move to a higher energy level; the energy gain is inversely proportional to the wavelength that is displaced as shown in equation 2.3:

$$E = \frac{hc}{\lambda} \qquad \text{(Equation 2.3)}$$

where h is planks constant, c is the speed of light, and λ is wavelength. If the energy gained is higher, the transmitted light will have a lower wavelength. The energy transmitted is seen in the ultraviolet and visible regions of the spectra with a wavelength between 200-700 nm.

Figure 2.7 shows different parts of a typical UV-Vis spectrometer. Usually, the sample is dissolved in a solvent before analysis, and the pure solvent is used as a blank or reference. Finally, the instrument compares the absorption of the blank solvent and the sample; the

difference in absorption is then attributed to the sample. In addition, a preferable solvent does not absorb radiation between 200-700 nm ranges.

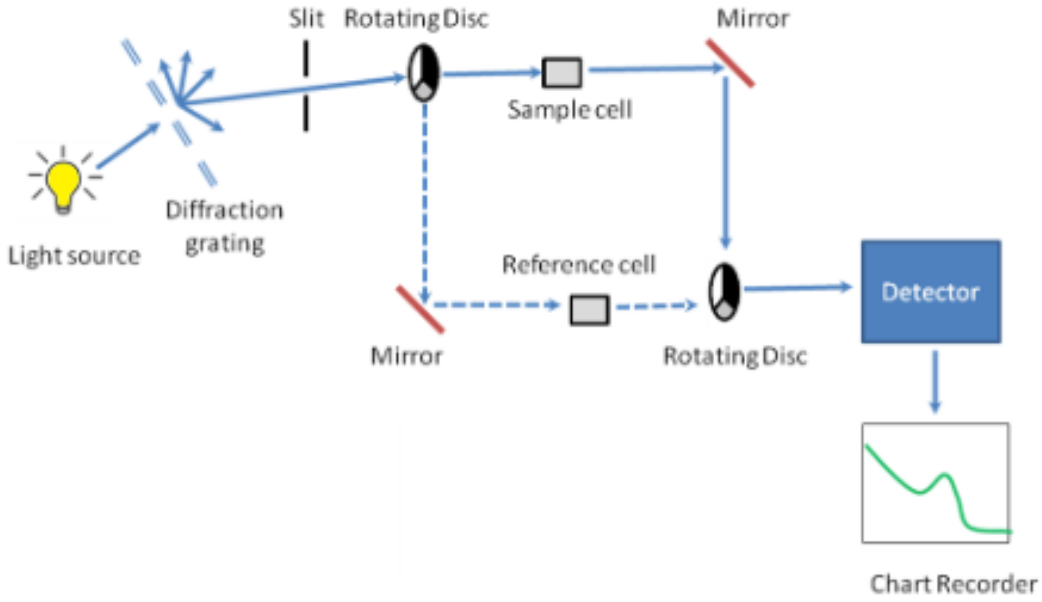

Figure 2.7: Schematics representation of UV-Vis spectrometer.[19]

Other than identification of samples, UV-Vis spectroscopy can be used to measure sample concentration. The concentration is determined using the Beer-Lambert Law:

$$A = log_{10}(I_0/I) = \varepsilon cL \qquad \text{(Equation 2.4)}$$

where A is absorbance, I_0 is the intensity of incident radiation, I is the intensity of transmitted radiation, ε is the molar extinction coefficient, c is the concentration of the sample, and L is the path length of the sample. The concentration of molecules in the sample is directly proportional to the absorbance. The above conclusion can only be drawn if the sample is diluted; therefore, the Beer-Lambert Law does not apply to samples with higher concentrations.

We used the Lambda XLS+ UV-Vis spectrometer to analyze our samples. The instrument can acquire data starting from 200 nm up to 900 nm. Before analysis, samples are dissolved or dispersed in Milli-Q deionized water, and the samples are monitored to ensure that their concentration remains diluted.

Reference

1. Williams, D. B.; Carter, C. B., *The Transmission Electron Microscope*. Springer: **1996**.

2. Cao, G.; Wang, Y., *Nanostructures and Nanomaterials, synthesis, properties, and applications*, 2nd ed.; World Scientific, **2011**.

3. Egerton, R.F. *Electron Energy-Loss Spectroscopy in the Electron Microscope,* 3rd ed.; Springer: New York, 2011.

4. Egerton, R.F. *Electron energy-loss spectroscopy in the TEM, Rep. Prog. Phys.* **2009**, 72, 1-25.

5. Pennycook, S. J., Nellist, P. D. *Scanning Transmission Electron Microscopy. Imaging and Analysis*. Springer: New York, **2011**.

6. Muller, D. A., Silcox, J. Delocalization in inelastic scattering. Ultramicroscopy, **1995**, 59, 195-213.

7. Willims, D. B., Carter, C. B. *The Transmission Electron Microscope*. *A textbook for materials Science.* Springer: New York, **2009**.

8. Silberberg, M. *Chemistry*, *The molecular Nature of Matter and Change*. McGraw-Hill: Boston, **2006**.

9. Van Olphen H, Parrish W., *X-ray And Electron Methods Of Analysis*. New York: Plenum Press; **1968**.

10. Aguiar, R. Synthesis, properties and applications of $AB(O,N)_3$ oxynitride perovskites, Ph.D. Dissertation, University of Augsburg, Germany, 2008.

11. Russ J., *Fundamentals Of Energy Dispersive X-ray Analysis*. London: Butterworths; **1984**.

12. Herglotz H, Birks L. *X-ray Spectrometry*. New York: M. Dekker; **1978**.

13. Energy dispersive X ray spectroscopy, https://www3.nd.edu/~kamatlab/facilities_physchar.html (accessed Aug 23, 2015).

14. Ferraro J, Basile L., *Fourier Transform Infrared Spectroscopy*. New York: Academic Press; **1985**.

15. Günzler H, Gremlich H., *IR Spectroscopy*. Weinheim: Wiley-VCH; **2002**.

16. Techniques Note, FT-IR spectroscopy, PerkinElmer Life and Analytical Sciences. http://www.utsc.utoronto.ca/~traceslab/ATR_FTIR.pdf (accessed Aug 23, 2015).

17. Everett D., Modern Chemical Techniques (Royal Society of Chemistry). *The Chemical Educator*, **1998**, 3, 1, 96-115.

18. Kotz, J., Treichel, P., Weaver, G., *Chemistry & Chemical Reactivity*. Belmont, CA: Thomson Brooks/Cole; 2006.

19. Wagner. A., Barron, A. R., Physical Methods in Chemistry and Nano Science, Connexions, Rice University, 2013.

CHAPTER 3

SYNTHESIS AND FUNCTIONALIZATION OF BORON/IRON OXIDE CORE/SHELL NANOPARTICLES

3.1 Introduction

Core/shell nanoparticles are zero-dimensional structures that are composed of two layers in which the layers are formed from different elements. For this project, the core is made of a lighter element boron and the shell is composed of a heavier iron oxide compound. Each layer is used for a specific purpose and to complement each other in order to enhance or alter a particular property. Core/shell nanomaterials can be used in many fields, but we are interested in biomedical application of these materials as biosensors, bio-imaging contrasts, and drug and gene delivery agents.[1] The biomedical application of boron-based nanostructures was discussed in the previous chapter; therefore, we will discuss the advantage of adding an iron oxide layer. Iron oxide core/shell structures are mainly synthesized via co-precipitation. Co-precipitation is a technique that uses a combination of reagents in aqueous media to form a final product that can be filtered out of the solution. This approach has been widely accepted for the synthesis of iron oxide core/shell nanoparticles because different parameters of the reaction such as pH and concentration can easily be controlled to produce particles with specific size distribution. Usually, iron (II) and iron (III) compounds are used to produce magnetite (Fe_3O_4). Gupta et al.

synthesized monodispersed Fe_3O_4 nanoparticles using iron (II) chloride ($FeCl_2$) and iron (III) chloride ($FeCl_3$) with base.[2]

The formation of the magnetite core or shell needs to be performed under inert atmosphere; thus, the system is purged with nitrogen gas. Figure 3.1[2] demonstrates a general co-precipitation process.

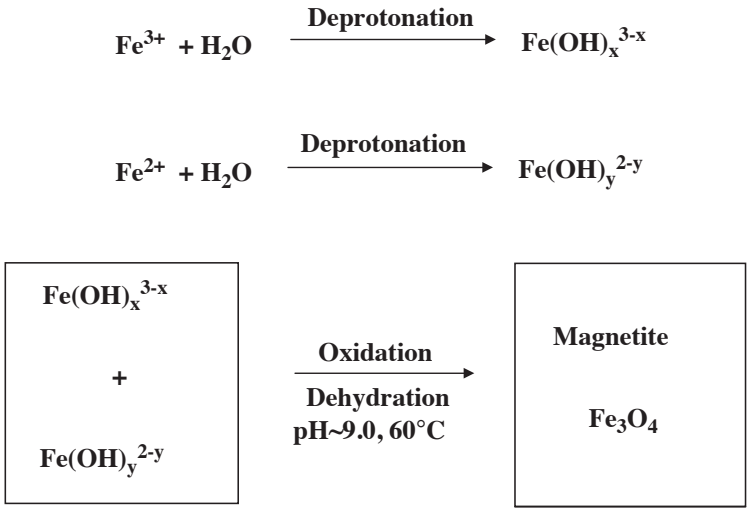

Figure 3.1: Schematic representation of co-precipitation reaction of $FeCl_2$ and $FeCl_3$.[2]

Iron oxide, specifically magnetite (Fe_3O_4), contains both Fe^{2+} and Fe^{3+} species that have four and five unpaired electrons in the 3d shell respectively creating a huge magnetic moment, which can be used for magnetic resonance imaging (MRI). Researchers showed that a cell can be located and traced using MRI as long as enough magnetic particles are accumulated inside the cell.[3] Furthermore, surface modification of magnetic nanoparticles with dextran and other organic molecules was undertaken to increase uptake. For example, dextran-coated magnetic nanoparticles have been used for liver[4] and node imaging.[5]

In addition to being a contrast agent for MRI, magnetic nanoparticles can be used to label cells and deliver drugs to specific cells. Cellular labeling is often used to track changes in

morphology or location of specific cells. Dextran,[4] carboxydextran,[6,7] carboxymethyl-dextran,[4] and citrate[8]-coated magnetic nanoparticles have been used for cellular labeling. On the other hand, the surface of magnetic nanoparticles can be modified via covalent or electrostatic interaction to increase water solubility of the particles and carry molecules that target cancer cells. For instance, magnetic nanoparticles have been used to deliver methotrexate,[9] and oxantrazole[10] to cancer cells in different parts of the body. Zhu et al.[11] used starch-coated magnetic nanoparticles to attach a carborane cage (1-R-2-butyl-ortho-$C_2B_{10}H_{10}$) and achieved 51.4 μg of boron/g of tumor with tumor/normal tissue ratios of around 10:1, which is the highest concentration of boron uptake reported to date. These nanoparticles can be guided to the target cell with an external magnet, which is the mechanism that allows a larger concentration of the drug to accumulate most easily. Also, uniform concentration of a compound can be achieved.

When nanoparticles are considered for drug delivery, one must consider the effect of particle size because it plays a key role on the concentration of the drug in the cell. To illustrate, particles that are too small or too large can be removed from the system before the drug targets the tumor cells; therefore, particles with a diameter between 10-100 nm are ideal for this purpose.[3] For our purposes we utilize all of the previously mentioned advantages of magnetic nanoparticles to deliver boron into a tumor cell for boron neutron capture therapy (BNCT). In addition, the iron oxide layer easily enables functionalization of the surface, which was a problem with boron nanoparticles.

In this chapter, we will discuss the synthesis of boron nanoparticles, boron/iron oxide core/shell nanoparticles, and functionalization of the core/shell nanoparticles. Boron nanoparticles can be prepared via chemical vapor deposition (CVD),[12] pyrolysis,[13] ball milling,[14] and arc discharge.[15] We have chosen to do pyrolysis of decaborane to produce boron

nanoparticles followed by co-precipitation of the iron precursor to form an iron oxide layer. Further, the particles were modified with organic groups such as amine-terminated PEG, folic acid, dopamine, starch, and α-D glucose that are excellent delivery agents for the core/shell nanoparticles.

3.2 Materials and Methods

3.2.1 Materials

All of the chemicals used in the experiment were purchased and used as received except decaborane, which was further purified via sublimation before use. A HERMLE Labortechnik centrifuge was used at 13,000 rpm for 10 minutes unless otherwise specified.

3.2.2 Synthesis of Boron Nanoparticles

Boron nanoparticles were generated via decomposition of decaborane at elevated temperature. A 0.7 g sample of purified decaborane (5.73 mmol) was taken in a round-bottom flask that is connected to a quartz tube placed inside a horizontal tube furnace. The other end of the tube was connected to a gas bubbler. The round-bottom flask and the quartz tube were purged with dry argon gas for 30 minutes, and the quartz tube was then heated to 700°C inside the tube furnace. Once the furnace reached the desired temperature, the round-bottom flask was heated to 105°C and the sublimed decaborane was passed through the quartz tube using a flow of dry argon gas with a rate of 0.22 L/min. The decaborane was decomposed over a period of six hours while passing through the quartz tube and the product deposited at the cooler end of the tube. The deposited dark powder was then collected and purified to isolate 305 mg of boron

nanoparticles (50% yield). The product was purified with either multiple ethyl acetate washes or directly dried in *vacuo* overnight.

3.2.3 Synthesis of Boron/Iron Oxide Core/Shell Nanoparticles

A 50 mg sample of boron nanoparticles (4.62 mmol), iron (II) chloride tetrahydrate ($FeCl_2.4H_2O$, 0.2068 g, 1.04 mmol), and iron (III) chloride hexahydrate ($FeCl_3.6H_2O$, 0.2728 g, 1.01 mmol) was added in a three-necked round-bottom flask. The flask was then purged with nitrogen followed by an addition of 75 mL of deionized (DI) water. The flask was stirred at 40°C while ammonium hydroxide solution (0.4 mL of NH_4OH in 4 mL of DI water) was added drop by drop. The pH of the solution was monitored, and more ammonium hydroxide solution was added until the pH reached 9-10. Once the intended pH was achieved, the reaction temperature was increased to 60°C and the solution was stirred for 30 minutes. The product was collected by centrifuging the reaction mixture and washing the product multiple times with DI water and ethanol. The final product was dried in *vacuo* overnight and then characterized.

A 100 mg sample of boron nanoparticles (9.25 mmol) prepared in the above step was dispersed in 25 mL DI water using ultrasonication. The mixture of $FeCl_3.6H_2O$ (0.675 g, 2.5 mmol) and $FeCl_2.4H_2O$ (0.248 g, 1.25 mmol) was added to the dispersion followed by dropwise addition of 15 mL 0.3 M sodium hydroxide solution. The resulting solution was stirred under argon atmosphere at room temperature for another 30 minutes. After completion, the product was collected by centrifuging the reaction mixture and washing the product multiple times with DI water and ethanol. The final product was dried in *vacuo* overnight and then characterized. Also, this reaction was repeated using twice as much of the reactant.

3.2.4 Functionalization of Boron Nanoparticles

3.2.4.1 Reaction with Bromine

A 0.115 g sample of boron nanoparticles (10.6 mmol) was dispersed in 20 mL of benzene for 20 minutes followed by an addition of 1 mL of bromine. The solution was stirred at room temperature for 24 hours. The product was collected by removal of the bromine and benzene under reduced pressure at 30°C. Finally, the product was dried in *vacuo* overnight.

The functionalization of boron nanoparticles with bromine is similar to the above procedure except the reaction time and the amount of bromine. A 0.116 g sample of boron nanoparticles (10.7 mmol) was dispersed in 20 mL of benzene for 20 minutes followed by an addition of 2.0 mL of bromine. The solution was stirred at room temperature for three days. The product was collected by removal of the bromine and benzene under reduced pressure at 30°C. The final product was dried in *vacuo* overnight.

3.2.4.2 Reaction with Amine-Terminated Polyethylene Glycol

Initially, an attempt was made to attach amine-terminated polyethylene glycol (PEG) directly on the surface of the boron nanoparticles. A 0.488 g sample of PEG and 0.020 g sample of boron nanoparticle (1.85 mmol) were placed in a round-bottom flask. Then the flask was vacuumed and purged with argon, and this step was repeated three times to remove oxygen from the system. Once the system was under argon, the contents were stirred at 60°C for three days. The product was then collected using centrifugation at 3,000 rpm for 30 minutes and purified by washing with water.

3.2.5 Functionalization of Boron/Iron Oxide Core/Shell Structure

3.2.5.1 Reaction with Oleic Acid

A one-pot synthesis and functionalization of boron/iron oxide core/shell nanoparticles were performed using oleic acid. A 100 mg sample of boron nanoparticles (9.25 mmol) prepared in the above step was dispersed in 25 mL DI water using ultrasonication. A mixture of $FeCl_3.6H_2O$ (0.675 g, 2.5 mmol) and $FeCl_2.4H_2O$ (0.248 g, 1.25 mmol) was added to the dispersion followed by dropwise addition of 15 mL 0.3 M sodium hydroxide solution. The resulting solution was stirred under argon atmosphere at room temperature for another 30 minutes. Then the flask was heated to 80°C followed by dropwise addition of 0.5 mL oleic acid for one hour. The resulting product was then collected via centrifugation and purified by washing with DI water and ethanol. Finally, the product was dried in *vacuo* overnight.

A 100 mg sample of boron/iron oxide core/shell nanostructure was taken in a round-bottom flask, and methanol (25 mL) was added. The solution was ultrasonicated to result in a uniform dispersion. The oleic acid (1 mL) was added to the solution, and the resulting mixture was then heated to 80°C with stirring for 4 hours. The resulting product was then collected via centrifugation and purified by washing with DI water and acetone. Finally, the product was dried in *vacuo* overnight. Scale-up synthesis was performed using this procedure with fivefold increase in the reagents.

3.2.5.2 Reaction with Citric Acid

A 120 mg sample of oleic acid functionalized boron/iron oxide core/shell nanoparticles was dispersed in a mixture of 7.5 mL of 1,2-dichlorobenzene (ODCB) and 7.5 mL of N,N'-dimethylformamide (DMF). After the addition of 0.1 g of citric acid to the solution, the resulting mixture was heated to 100°C with constant stirring for 24 hours. The product was then collected via extraction with ethyl ether. The resulting functionalized nanoparticles were centrifuged from the ether solution and purified by multiple acetone washings.

A 100 mg of sample boron/iron oxide core/shell nanoparticles was dispersed in a mixture of 7.5 mL of ODCB and 7.5 mL of DMF. After the addition of 0.1 g of citric acid to the solution, the resulting mixture was heated to 100°C with constant stirring for 24 hours. The product was then collected by adding ethyl ether and separating the ether layer from the aqueous layer. The resulting functionalized nanoparticles were centrifuged from the ether solution and purified by multiple acetone washings.

3.2.5.3 Reaction with Amine-Terminated PEG

Water-soluble nanoparticles were prepared using amine-terminated PEG. Specifically, 0.05 g of citric acid-coated boron/iron oxide core/shell nanoparticles was dispersed in DI water and the pH was adjusted to 9 by adding NaOH. A 0.1 g sample of bis (3-aminopropyl)-terminated polyethylene glycol, 0.06 g of *N*-hydroxysuccinimide (NHS), and 0.05 g of 1-ethyl-3-(3-dimethylamino-propyl) carbodiimide hydrochloride (EDC) were added to the basic solution of nanoparticles. The resulting mixture was then stirred for 48 hours and the final product was separated using a cellulose membrane dialysis tube, dried in *vacuo*, and then characterized.

3.2.5.4 Reaction with Dopamine

A 0.022 g sample of oleic acid functionalized boron/iron oxide core/shell nanoparticles was dispersed in 58 mL of chloroform for 30 minutes. A 0.1056 g of dopamine hydrochloride (DA.HCl) was dissolved in 4 mL methanol, and then this solution was added to the flask containing the nanoparticles in 0.5 mL aliquots. The flask was then stirred at room temperature for 4 hours. The product was collected via centrifugation at 4000 rpm for 10 minutes. The sediment was collected and rinsed with methanol followed by the removal of methanol using a rotary evaporator. The product was placed in a flask and DA.HCl solution was added (0.1097 g sample of DA.HCl dissolved in 40 mL methanol). The content in the flask was stirred overnight at room temperature. The final product was then collected via centrifugation at 4000 rpm for 10 minutes and purified by washing with methanol. Finally, the product was dried in *vacuo* overnight.

A 0.104 g of boron/iron oxide core/shell nanoparticles was dispersed in 10 mL of dimethyl sulfoxide (DMSO) for 35 minutes. In a beaker, 201.1 mg of DA.HCl was dissolved in 20 mL DMSO, and this solution was added to the flask containing the core/shell nanoparticles. The solution in the flask was stirred at room temperature overnight. The resulting product was then collected via centrifugation and purified by washing with a solution of 5:1 ratio of ethanol: hexane. Finally, the product was dried in *vacuo* overnight.

3.2.5.5 Reaction with Folic Acid

A 52.4 mg sample of boron/iron oxide core/shell nanoparticles was dispersed in 5 mL of DI water for 30 minutes. In a beaker, 1.2602 g of sodium bicarbonate was dissolved in 10 mL DI

water and this solution was added to the flask containing the core/shell nanoparticles. Then the content was further dispersed for 5 minutes. A 0.1036 g sample of folic acid was added, and the flask was stirred for 24 hours at room temperature. The addition of folic acid and the reaction following was performed in a dark room. The resulting product was centrifuged at 6000 rpm for 10 minutes. Next the precipitate was collected via centrifugation and purified by washing with DI water. Last, the product was dried in *vacuo* overnight.

A 52.6 g sample of dopamine functionalized boron/iron oxide core/shell nanoparticles was dispersed in 10 mL of sodium bicarbonate solution (0.84 g sample of sodium bicarbonate dissolved in 10 mL of DI water) for 40 minutes. The flask was transferred into a dark room, then 99.3 mg of folic acid and 51.8 mg of NHS were added, and the content was stirred for 5 minutes before the addition of 86.5 mg of EDC. The flask was stirred for 24 hours in dark. The resulting product was then collected via centrifugation and purified by washing with ethanol. Last, the product was dried in *vacuo* overnight.

3.2.5.6 Reaction with Starch

A 115 mg sample of boron/iron oxide core/shell nanoparticles was dispersed in 15 mL of DI water for 30 minutes. In a beaker, 1.152 g of modified starch was dissolved in 15 mL DI water while stirring at 70°C under reflux and this solution was added to the flask containing the core/shell nanoparticles. Afterward the content was dispersed for 15 minutes using a sonicator and then the content was stirred for 21 hours at room temperature. The resulting product was separated using a cellulose membrane dialysis tube, dried in *vacuo*, and then characterized.

3.2.5.7 Reaction with α-D Glucose

A 85 mg sample of oleic acid functionalized boron/iron oxide core/shell nanoparticles was dispersed in 15 mL of chloroform for 30 minutes. In a beaker, 1.503 g of α-D glucose was dissolved in 15 mL DMF while stirring at 65°C and the solution containing the functionalized core/shell nanoparticles was added to this flask. Afterward the content was stirred for 4 hours under reflux. Then the content in the flask was stirred for additional 21 hours at room temperature. The resulting product was then collected via centrifugation and purified by washing with ethanol. Finally, the product was dried in *vacuo* overnight.

3.2.6 Biological Studies

Cytotoxicity of the citric acid (Sample 1) and amine-terminated PEG (Sample 2) functionalized boron/iron oxide core/shell compounds were studied using a placenta cell line. A 111 mg of Sample 1 was dissolved in 500 μL phosphate-buffered saline (PBS), but the compound was not soluble. Therefore, 50 μL of DMSO was added. Concurrently, 138 mg of Sample 2 was dissolved in 500 μL PBS. Each sample was then filtered through mini-pore filters. Next a 100 μL of the sample was added to 100 μL cell suspension and was diluted with 100 μL of minimum essential medium (MEM) (Table 4.1). Afterward the cells were incubated at 37°C for 48 hours followed by a 3-Amino-7-dimethylamino-2-methylphenazine hydrochloride (natural red) uptake for one hour. Finally, the dye was extracted and analyzed using UV-Vis spectroscopy at 540 nm. On the other hand, cytotoxicity of the folic acid and dopamine functionalized boron/iron oxide core/shell compounds were studied using a triple negative breast cancer cell

line MDA-MB-231. A detailed description of the cytotoxicity studies can be found in Chapter 4 Section 4.2.5.

Table 3.1

Concentrations of Samples

Number (n)	Cell Suspension (2×10^5/ml)	Sample (μL)	MEM (μL)	Concentration	Final concentration
1	100 μL	100	0	$(1/2)^{n-1}$	$0.5\times(1/2)^{n-1}$
2	100 μL	100	100	$(1/2)^{1}$	0.25
3	100 μL	0	100	$(1/2)^{2}$	0.125
4	100 μL	0	100	$(1/2)^{3}$	0.0625
5	100 μL	0	100	$(1/2)^{4}$	0.0312
6	100 μL	0	100	$(1/2)^{5}$	0.0156
7	100 μL	0	100	$(1/2)^{6}$	0.00781
8	100 μL	0	100	$(1/2)^{7}$	0.0039
9	100 μL	0	100	$(1/2)^{8}$	0.00195
10	100 μL	0	100	$(1/2)^{9}$	0.000976
11	100 μL	0	100	$(1/2)^{10}$	0.000488
12	100 μL	0	100	$(1/2)^{11}$	0.000244

3.3 Results and Discussion

3.3.1 Synthesis of Boron Nanoparticles

Decomposition of decaborane at an elevated temperature under inert atmosphere was reported to form boron nanoparticles.[16] The methodology can be performed at 700°C or 900°C (Equation 3.1). However, we chose to use the lower temperature, 700°C, to prepare the same nanoparticles in a desired dimension.

$$B_{10}H_{14(s)} \xrightarrow{110°C} B_{10}H_{14(g)} \xrightarrow[6H]{700°C} 10B_{(s)} + 7H_{2(g)} \qquad \text{(Equation 3.1)}$$

The dimension of the product was determined by transmission electron microscopy (JEOL 2010 TEM). The diameter of the nanoparticles ranged from 10 to 100 nm. Nevertheless, more than 62% of the nanoparticles had a diameter between 25-55 nm (Figure 3.2), and the nanoparticles displayed quasi-spherical morphology (Figure 3.3).

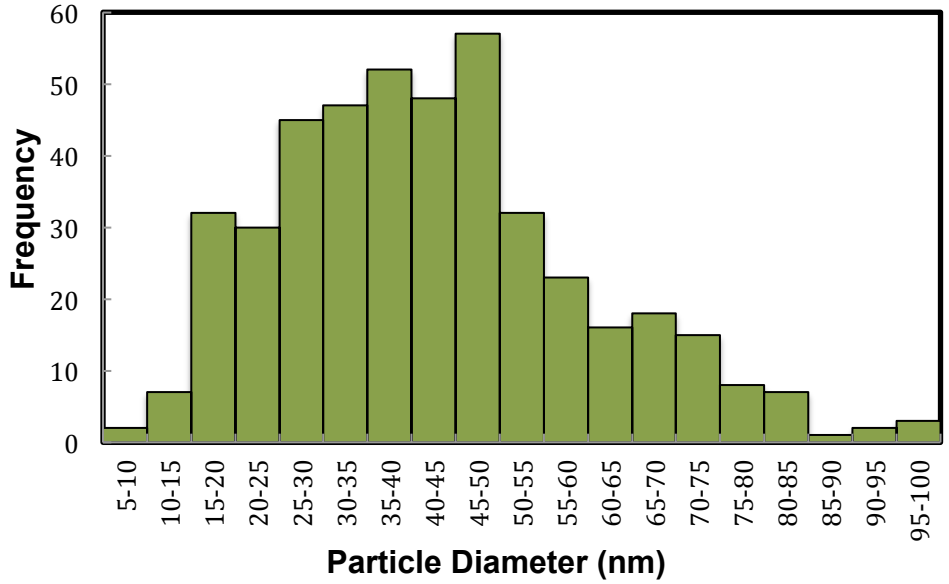

Figure 3.2: Particle size histogram of boron nanoparticle.

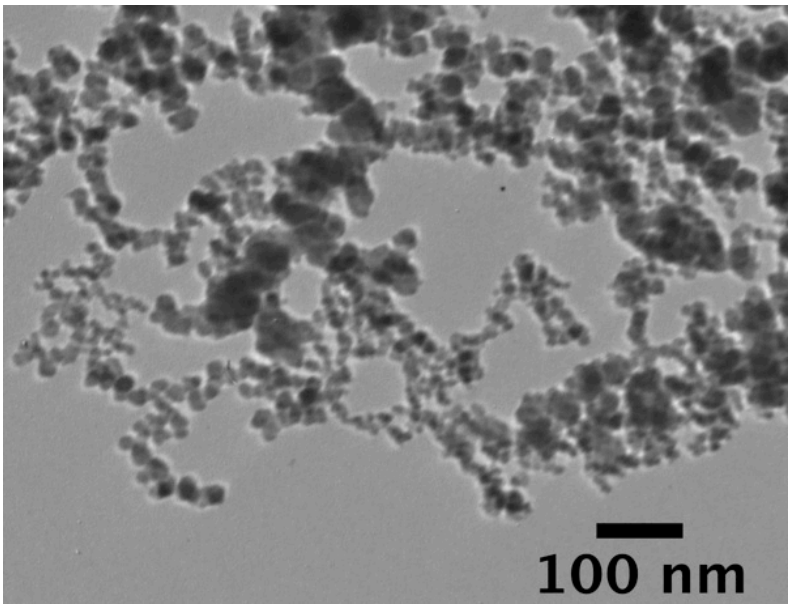

Figure 3.3: TEM image of boron nanoparticles.

The X-ray photoelectron spectroscopy (XPS) and energy-dispersive X-ray spectroscopy (EDX) data indicated high purity of the boron nanoparticle samples. The boron 1s peak appeared to be at 187.7 eV without any additional peaks, indicating that the sample consisted of elemental boron (Figure 3.4 a). The additional carbon peak at 285 eV and oxygen peak at 534 eV in the XPS data come from the carbon tape that was used to attach the powder sample to the sample holder during characterization (Figure 3.4 b). The EDX data establishes the purity of the sample (Figure 3.5) with almost 80% atomic weight of boron. However, surface oxidation of boron nanoparticles is a common phenomenon and has been reported in the literature.[17,18]

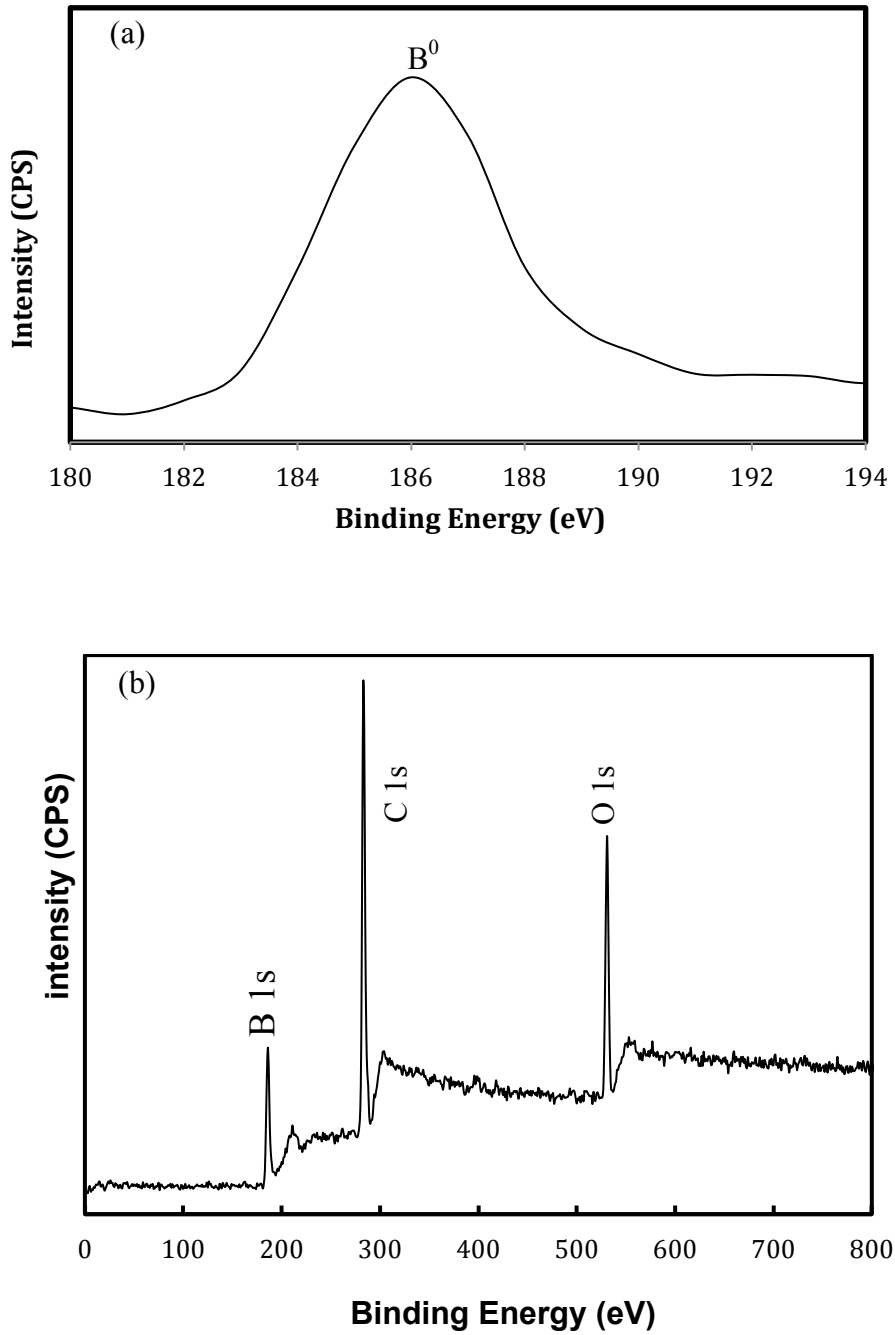

Figure 3.4: (a) B 1s XPS spectrum of boron nanoparticles and (b) XPS spectrum of boron nanoparticles.

(a)

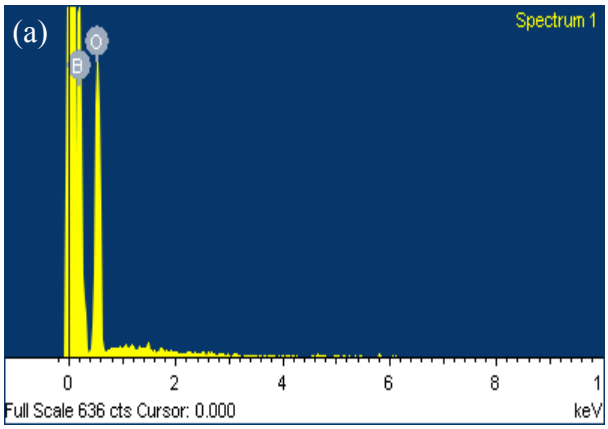

(b)

Element	Weight %	Atomic %
B	72.15	79.31
O	27.85	20.69
Total	100	100

Figure 3.5: (a) EDX spectrum of boron nanoparticles and (b) EDX data for boron nanoparticles.

Furthermore, a color variation was observed between nanoparticles. Specifically some nanoparticles were darker than others (red circles) (Figure 3.6) and these particles were analyzed using electron energy-loss spectroscopy (EELS). The EELS data shows that the particles have identical chemical composition. However, the darker particles (red circle 2) are denser so that the carbon peak around 280 eV, which is coming from the grid, is very weak. Figure 3.7 shows the decrease in intensity of the carbon peak as the particles become darker.

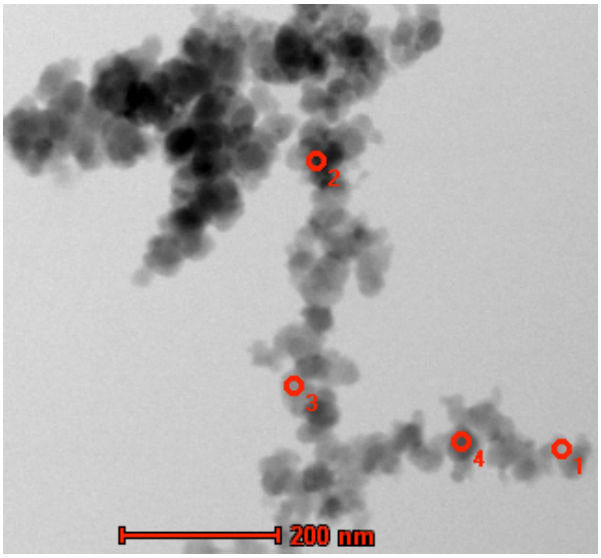

Figure 3.6: Bright-field TEM image of boron nanoparticles.

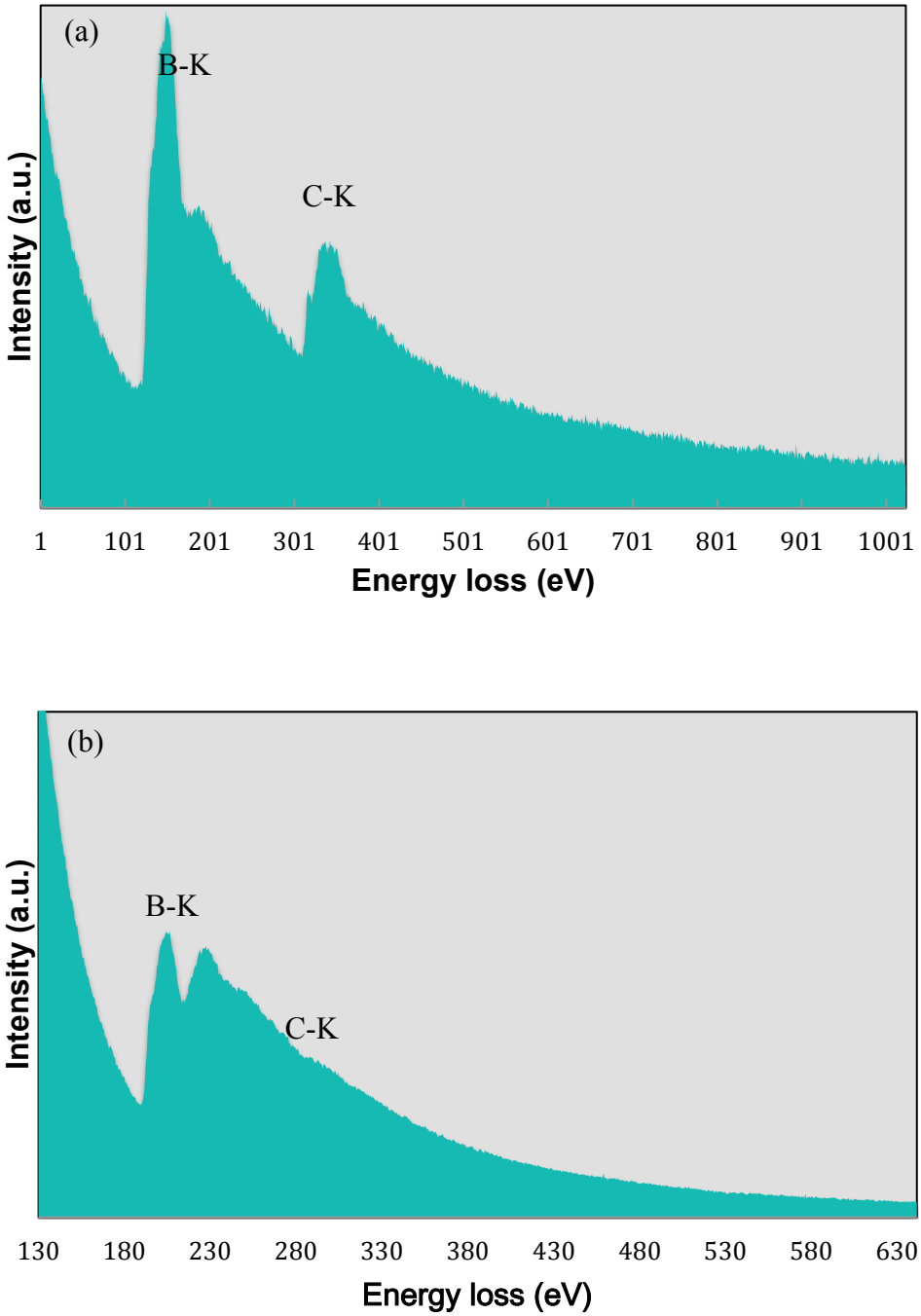

Figure 3.7: EELS spectrum of (a) light grey (1) boron nanoparticles and (b) black or dark (2) boron nanoparticles.

3.3.2 Synthesis of Boron/Iron Oxide Core/Shell Nanoparticles

The formation of the iron oxide shell was performed using co-precipitation of $FeCl_3.6H_2O$ and $FeCl_2.4H_2O$ with base (NH_4OH) in the presence of the boron nanoparticle. The TEM image shows the product of the first attempt contains nanoparticles and other amorphous structures (Figure 3.8).

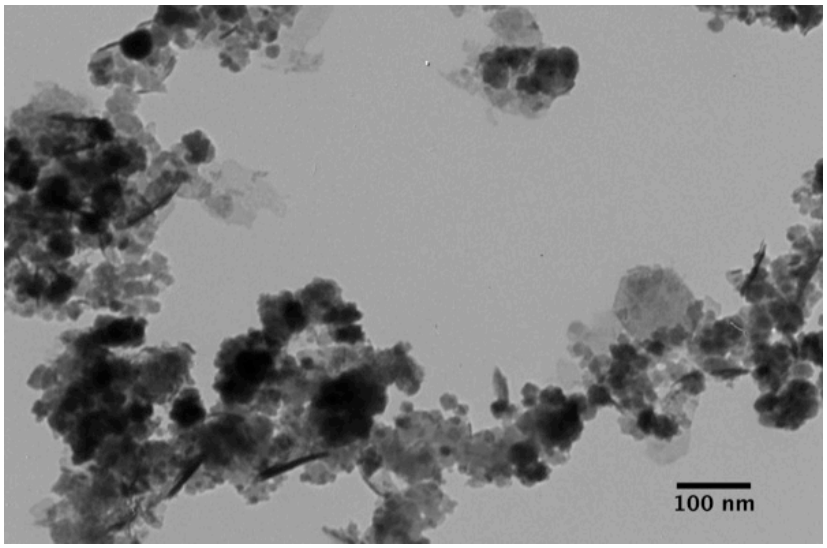

Figure 3.8: TEM image of boron/iron oxide core/shell nanoparticles.

Encapsulation of a mixture of magnetic nanoparticles (MNPs) and boron oxide has already been demonstrated.[19] A similar methodology was utilized to encapsulate boron nanoparticles with a mixture of iron (II) chloride tetrahydrate and iron (III) chloride hexahydrate after the first unsuccessful attempt (Figure 3.9). The resulting product only contains nanoparticles, and an average increase in the particle size of 8 nm was observed via high-resolution transmission electron microscopy (HRTEM) after encapsulation. HRTEM also

provides a clear visual distinction between the core and shell formation of the nanostructures (Figure 3.10).

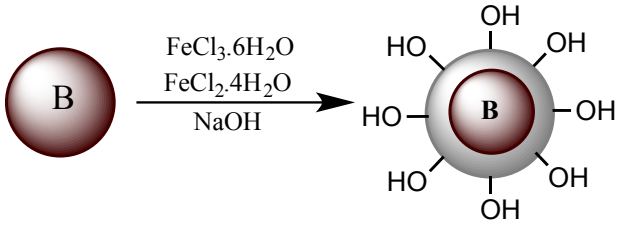

Figure 3.9: Synthesis of boron/iron oxide core/shell nanoparticles.

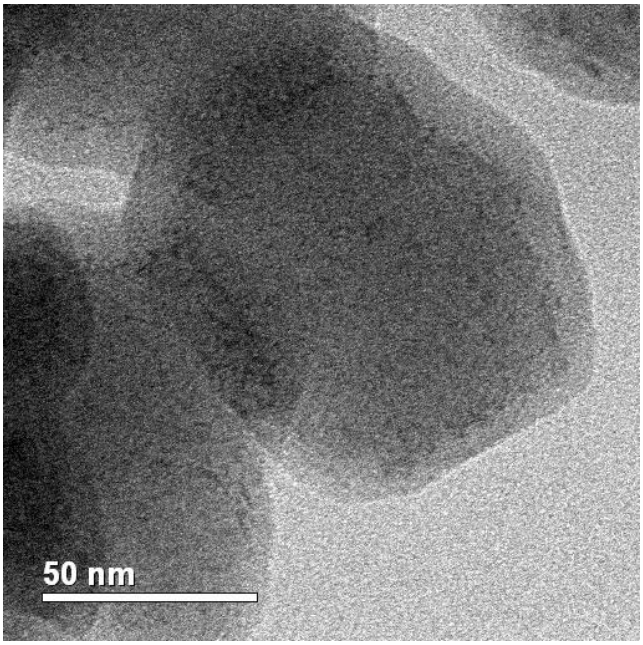

Figure 3.10: HRTEM image of boron/iron oxide core/shell nanoparticles.

The composition of the core/shell structure was identified by XPS, displaying binding energies for boron 1s, oxygen 1s, and iron 2p peaks at 187, 530, and 710 eV, respectively (Figure 3.11 a). These values are consistent with those published elsewhere.[20] The additional carbon peak seen in the spectrum comes from the carbon tape used during sample analysis. Furthermore

the B 1s XPS analysis suggested oxidation of the boron core during the formation of iron oxide shell, which is evident by the additional peak at 192 eV corresponding to boron oxide where boron has +3 oxidation state (Figure 3.11 b).

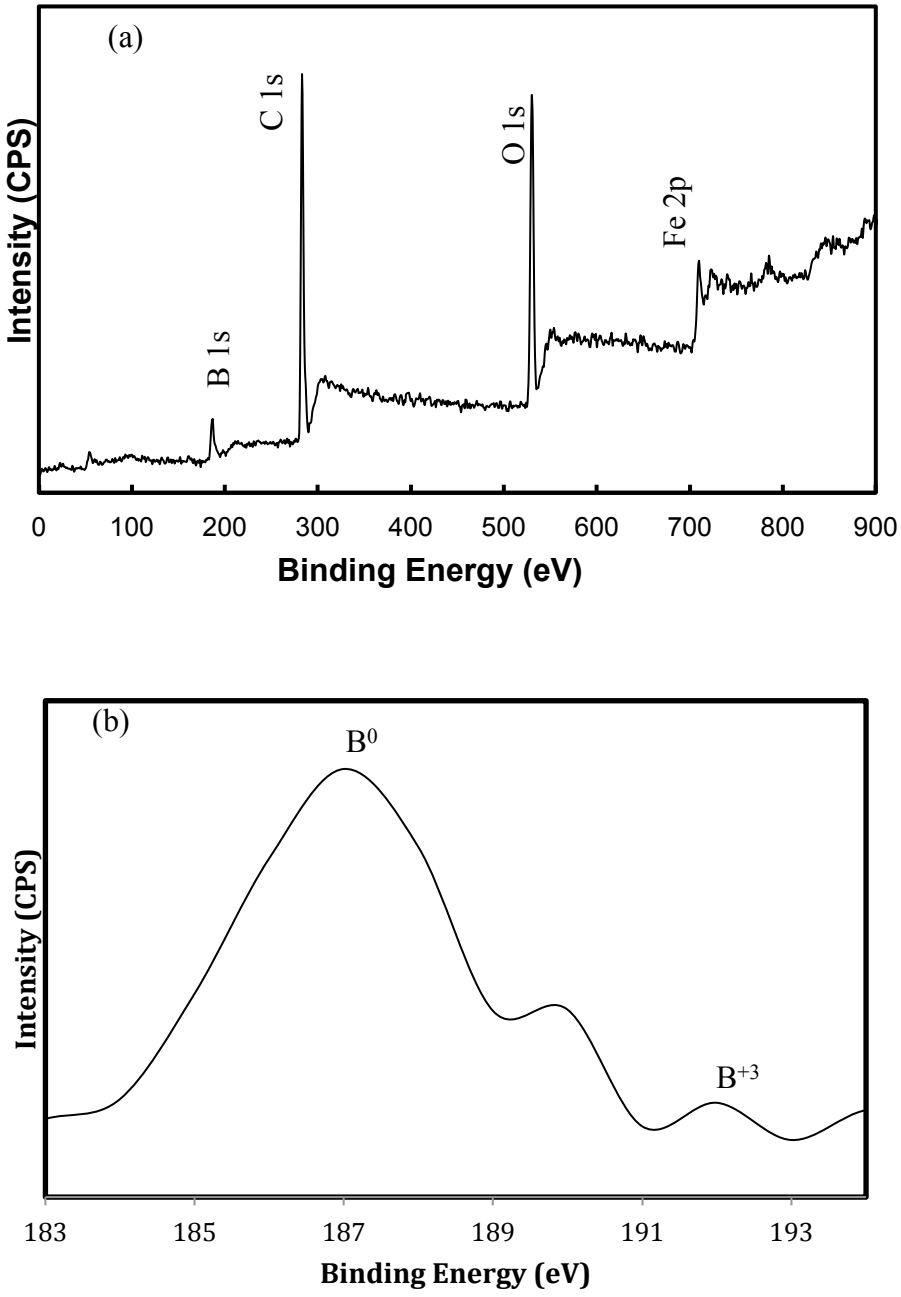

Figure 3.11: (a) XPS spectrum of boron/iron oxide core/shell nanoparticles and (b) B 1s XPS spectrum of boron/iron oxide core/shell nanoparticles.

Additional elemental analysis was performed using EELS with 200 kV energy and spot size 5. This method allows us to analyze the elemental composition of a single particle (Figure 3.12). EELS data of the dark particles shows energy loss peaks at 189, 285, 534, and 709 eV corresponding to B-K, C-K, O-K, and Fe-$L_{2,3}$, respectively (Figure 3.13), confirming a single particle is composed of boron and iron oxide. However, some of the particles that are lighter only contain B-K, C-K, and O-K energy loss peaks. The energy loss values are broken down into smaller values of 150 - 650 eV and 400 - 900 eV to allow easier peak identification. In addition, the HRTEM and the intensity of Fe-$L_{2,3}$ peaks from EELS indicate that the iron oxide layer has a smaller diameter compared to the boron core.

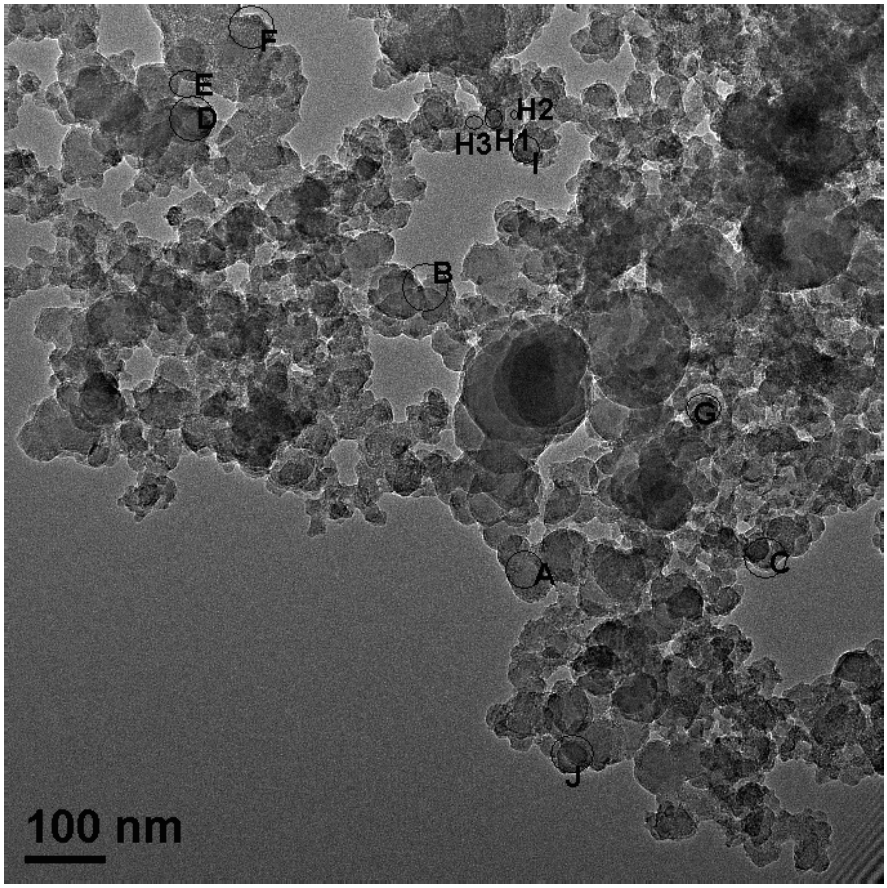

Figure 3.12: Bright-field TEM image of boron/iron oxide core/shell nanoparticles with marked single particles used for EELS analysis.

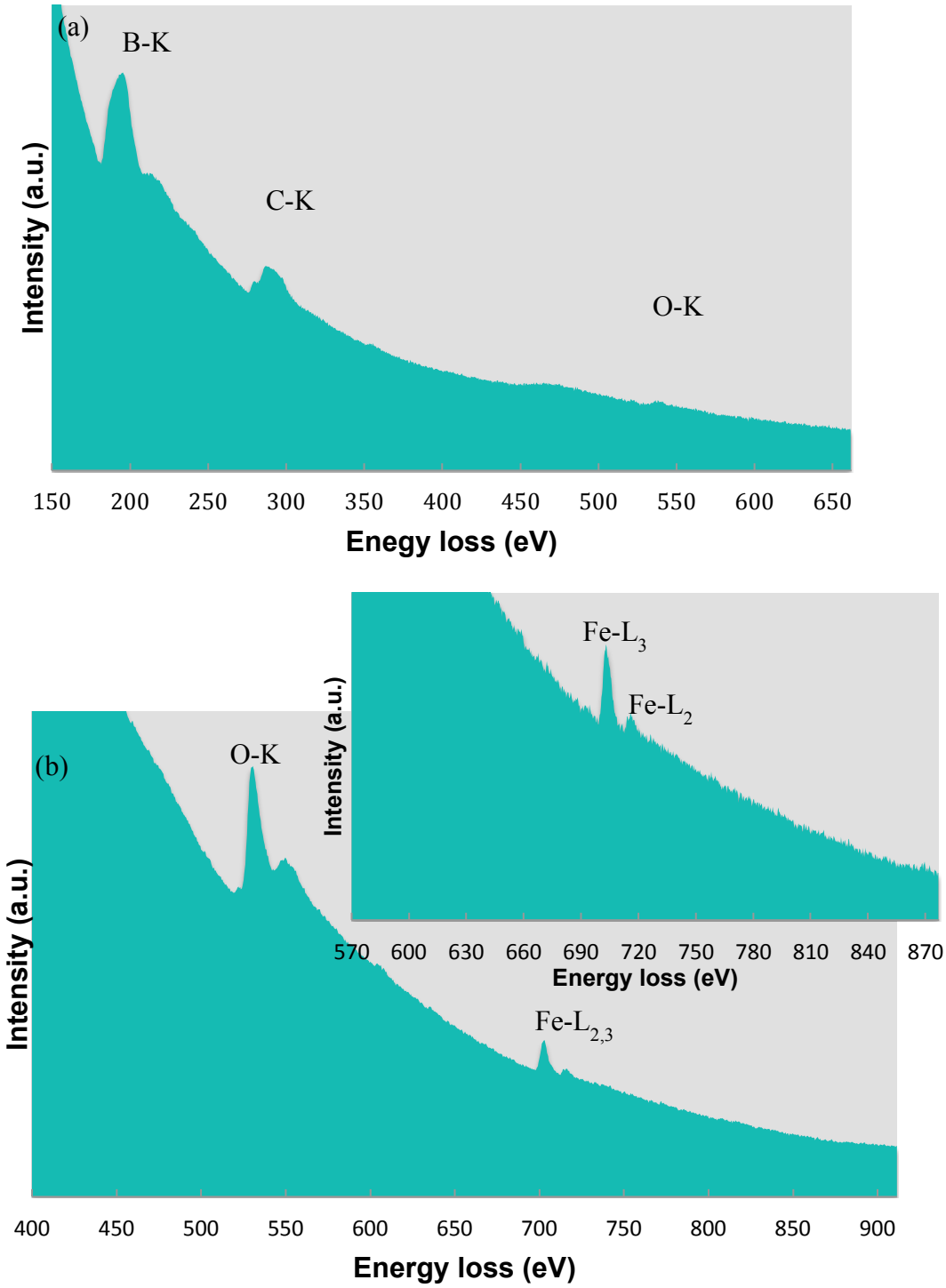

Figure 3.13: EELS spectrum of boron/iron oxide core/shell nanoparticles containing (a) B-K and C-K peaks and (b) O-K and Fe-$L_{2,3}$ peaks.

Furthermore, background subtraction was performed in order to simplify the spectrum and remove some of the noise (Figure 3.14). A background subtraction will reveal peaks in the zero loss regions, which will not be seen in normal circumstances. In our case, a silicon (Si-$L_{2,3}$) peak was detected at 100 eV. In order to determine the source of the silicon further analysis was done. The silicon contamination can come from the product or the carbon grid where the product is placed. Therefore, an area of the carbon grid without any core/shell nanoparticles was analyzed. The resulting spectrum contains the same silicon peaks. However, when a pure carbon grid was analyzed there was no silica peak observed above the background noise, suggesting the carbon grid was not the source of the silicon contamination (Figure 3.15). Therefore, the silica can possibly come from glasswares used during the synthesis and sample preparation process.

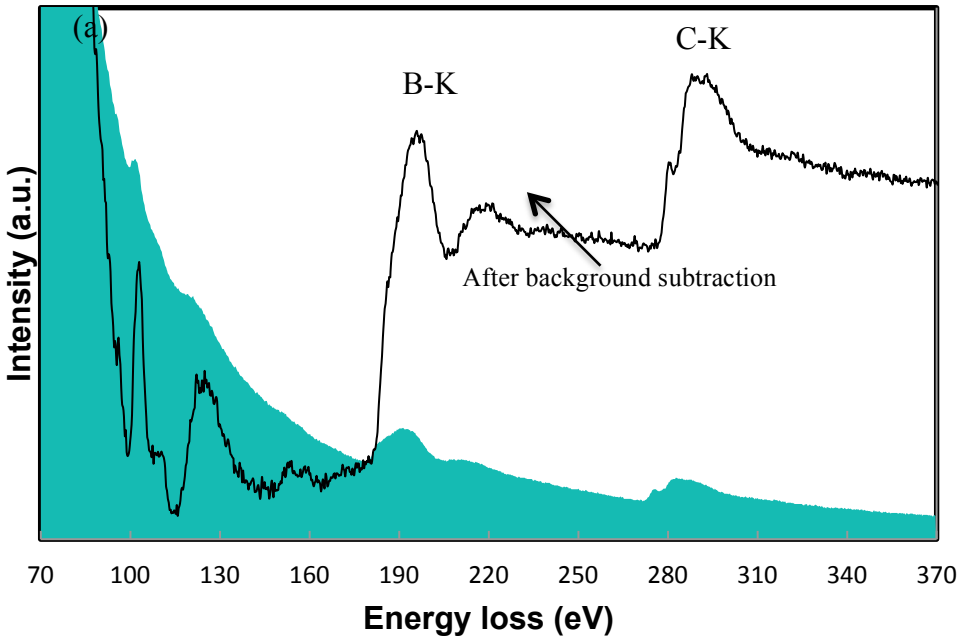

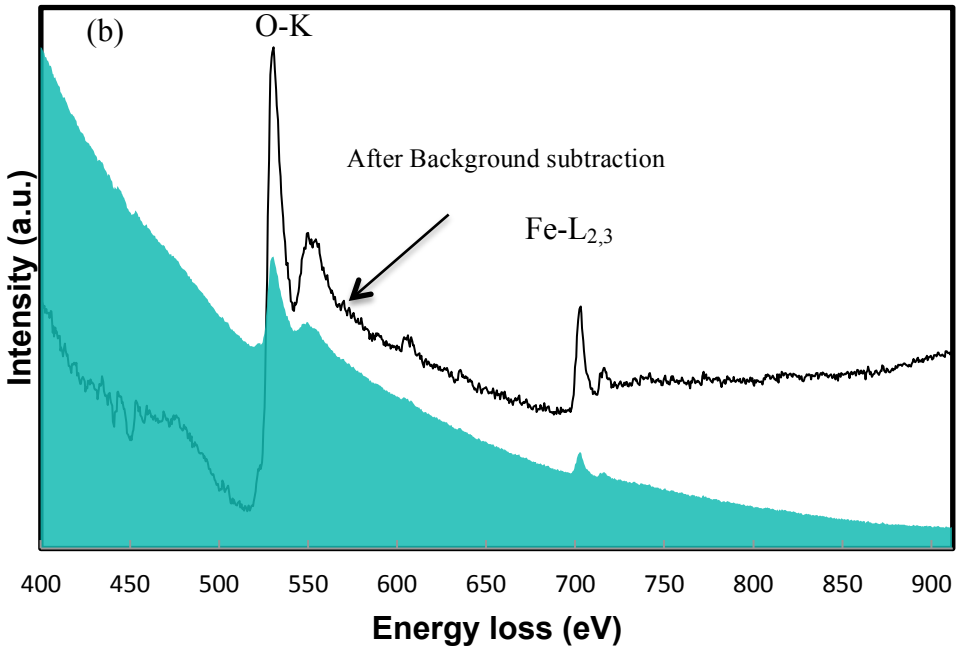

Figure 3.14: EELS spectrum of boron/iron oxide core/shell nanoparticles after background subtraction containing (a) B-K and C-K peaks and (b) O-K and Fe-$L_{2,3}$ peaks.

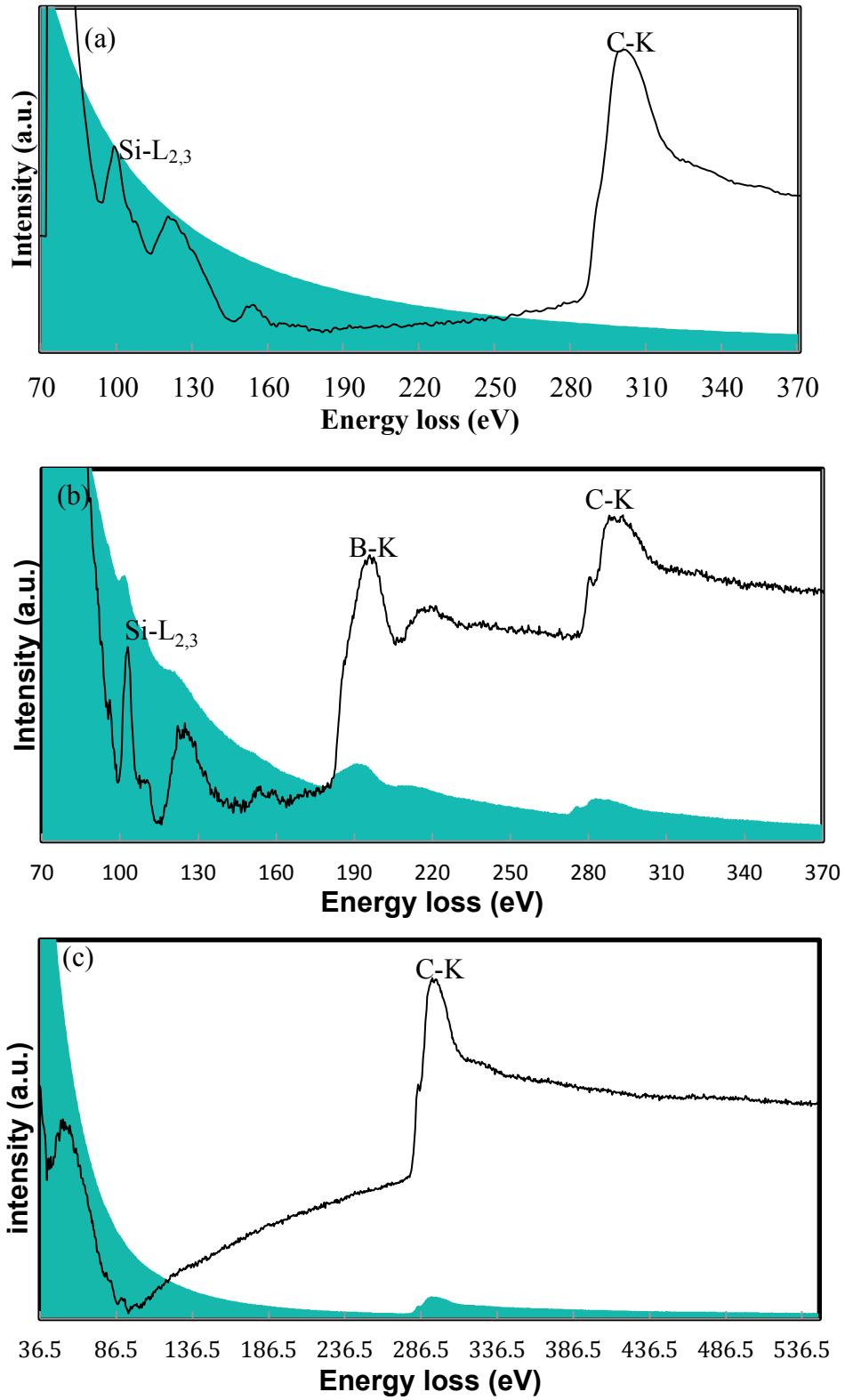

Figure 3.15: EELS spectrum of the zero loss regions. (a) Carbon grid support, (b) boron/iron oxide core/shell nanoparticles, (c) pure carbon grid.

The crystalline property of the boron/iron oxide core/shell nanoparticles was examined using an electron diffraction pattern in TEM. The result recovered from this analysis consists of evenly distributed circular patterns that are not well defined or spotty, indicating the core/shell nanoparticles are highly disordered (Figure 3.16).

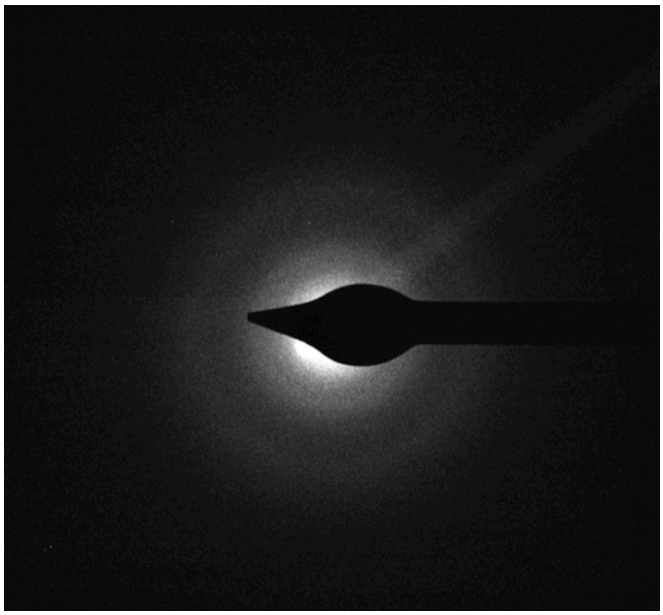

Figure 3.16: Electron diffraction pattern of boron/iron oxide core/shell nanoparticles.

3.3.3 Functionalization Of Boron Nanoparticles

3.3.3.1 Reaction with Bromine

Direct surface functionalization of boron nanoparticles is not well established because of boron's nature to readily oxidize and form boron oxide. However, boron is inert in forming bonds with elements other than oxygen. Bromination of the boron nanoparticle was attempted

using a published procedure.[15] The TEM image of the product shows the boron nanoparticles after surface modification with bromine maintained quasi-spherical morphology (Figure 3.17).

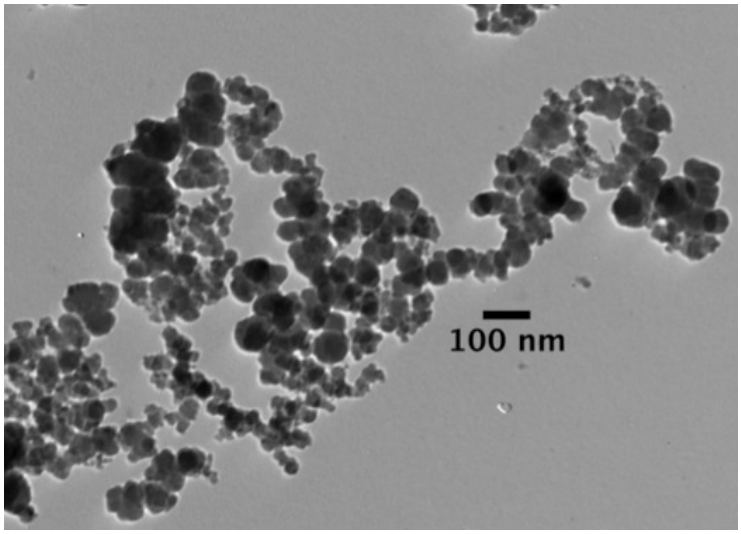

Figure 3.17: TEM image of brominated boron nanoparticles.

EDX analysis reveals a small concentration of bromine suggesting that the surface modification of the particles was not complete. Figure 3.18 shows that the product only contains 0.49% atomic weight of bromine. However, a larger concentration of bromine was achieved when the amount of bromine in the experiment was increased fourfold (Figure 3.19). The optimized reaction condition produced boron nanoparticles with 4.19% atomic weight bromine.

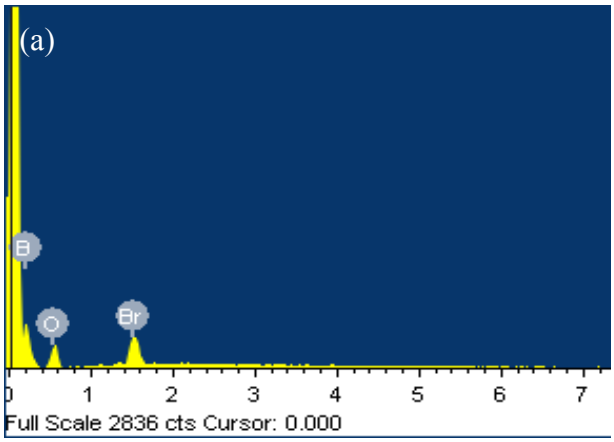

(b)

Element	Weight %	Atomic %
B	72.56	81.20
O	24.21	18.31
Br	3.23	0.49
Total	100	100

Figure 3.18**:** (a) EDX spectrum of brominated boron nanoparticles. (b) EDX data of brominated boron nanoparticles.

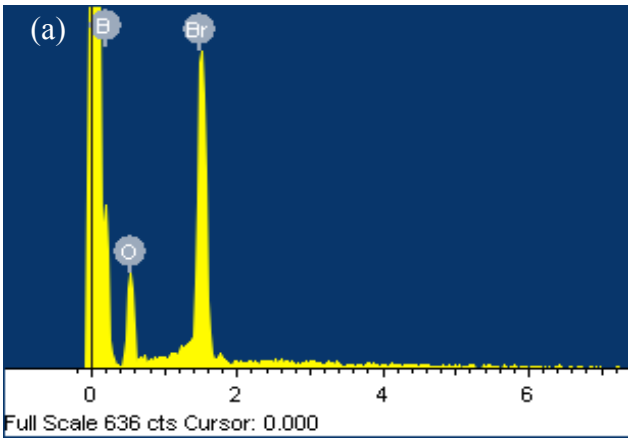

(b)

Element	Weight %	Atomic %
B	58.43	78.84
O	18.62	16.97
Br	22.95	4.19
Total	100	100

Figure 3.19**:** (a) EDX spectrum of optimized bromination reaction. (b) EDX data of optimized bromination boron nanoparticles.

3.3.3.2 Reaction with Amine-Terminated PEG

Functionalization of boron nitride nanotubes with amine-terminated PEG (NH_2-PEG-NH_2) was reported[21] and a similar idea was implemented to modify our boron nanoparticles. After performing the reaction, the product was collected from the aqueous part assuming that

boron nanoparticles that are functionalized with the polymer would be soluble and stay in the aqueous layer. However, the TEM image shows no evidence of boron nanoparticles in the product. Therefore, functionalization of boron nanoparticles with bis (3-aminopropyl)-terminated PEG was not successful.

3.3.4 Functionalization of Boron/Iron Oxide Core/Shell Structure

More than four boron carriers such as amine-terminated PEG, dopamine, folic acid, starch, and α-D glucose were used (Figure 3.20).

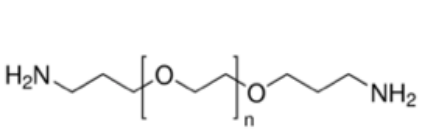

Amine-terminated polyethylene glycol

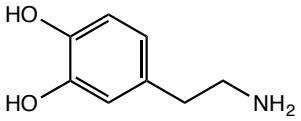

Dopamine

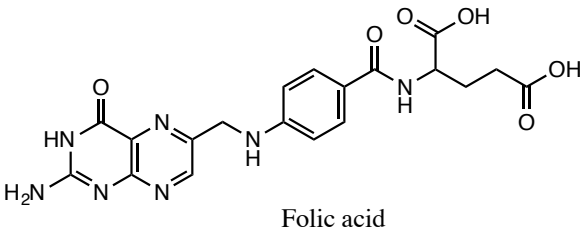

Folic acid

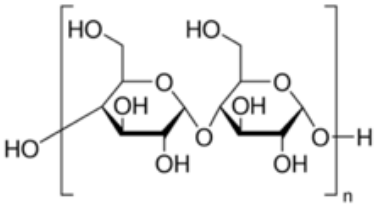

Starch

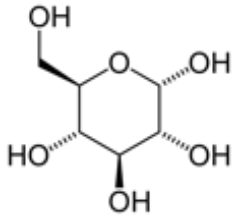

α-D glucose

Figure 3.20: Structure of various boron carriers used.

3.3.4.1 Reaction with Oleic Acid

Synthesis of oleic acid functionalized particles is shown in Figure 3.21. The reaction was performed while the core/shell structure was forming[22] or after the core/shell structure was purified.[23] We chose to functionalize the nanoparticles after recovering the pure core/shell nanoparticles to reduce any side reaction and impurity.

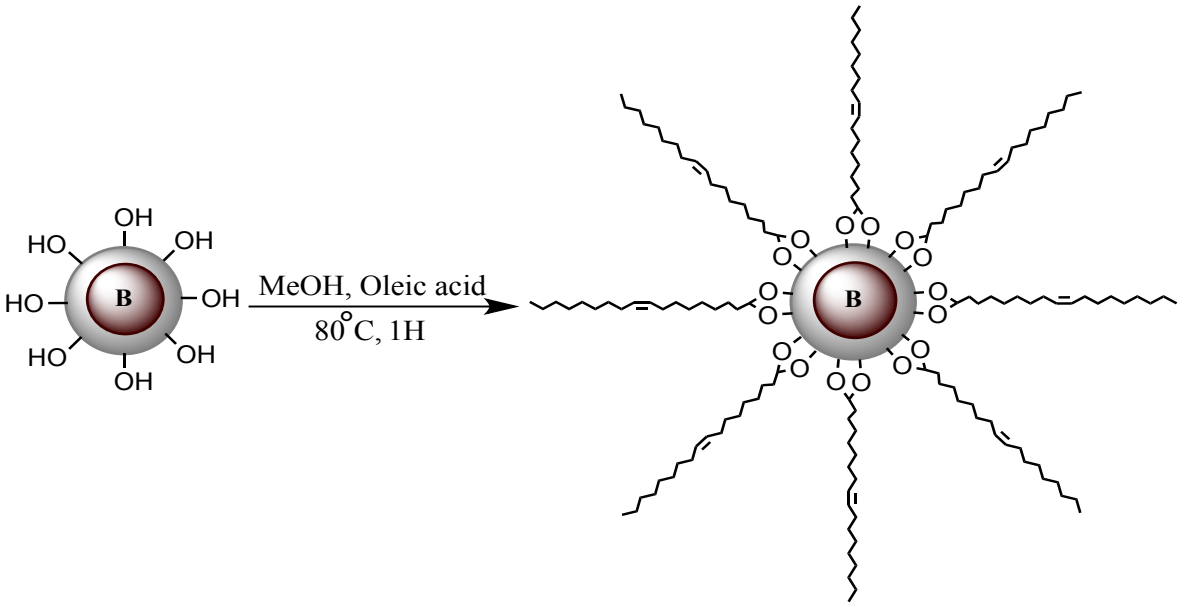

Figure 3.21: Synthesis of oleic acid functionalized boron/iron oxide core/shell nanoparticle.

Oleic acid forms bonds through carboxyl (COOH) moieties with the surface of the nanostructure as evident in the Fourier-transform infrared spectroscopy (ATR-FTIR) spectrum of the resulting functionalized product. The ATR-FTIR spectrum of oleic acid-coated core/shell nanostructure composite (Figure 3.22) exhibited a peak at 1625 cm^{-1} corresponding to the carboxyl group present in the product. Additional peaks at 2863 cm^{-1} and 2926 cm^{-1} are assigned to aliphatic C-H groups and the peak at 3315 cm^{-1} can be attributed to the OH group from the absorbed moisture.

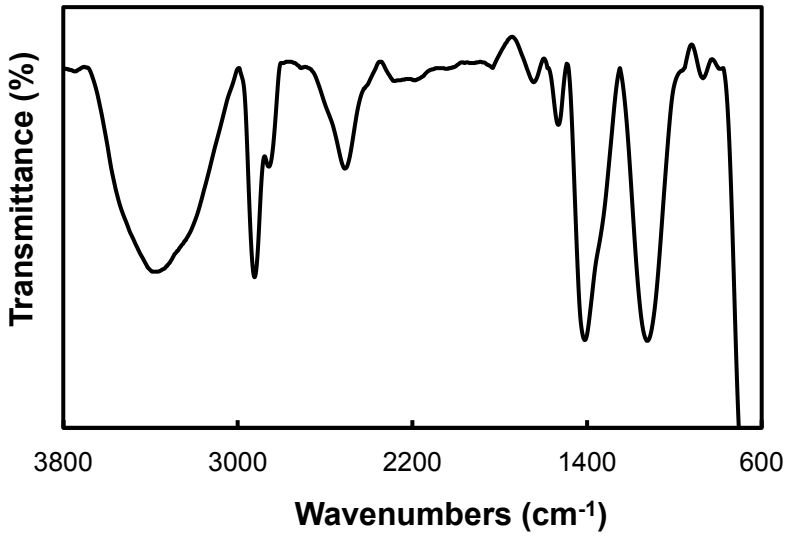

Figure 3.22: ATR-FTIR spectrum of oleic acid functionalized boron/iron oxide core/shell nanoparticles.

3.3.4.2 Reaction with Citric Acid

The boron/iron oxide core/shell nanostructure composite was further modified using a ligand exchange reaction with citric acid that has a higher affinity for the surface of iron oxide.[23] The ligand exchange reaction successfully produced citric acid-coated core/shell nanostructure composite and the higher affinity of citric acid towards iron oxide surface is evidently due to the presence of multiple carboxyl groups in citric acid. The ATR-FTIR spectrum of citric acid-coated boron/iron oxide nanostructure composite showed peaks at 2943 cm^{-1} and 3403 cm^{-1} that were due to aliphatic C-H and hydroxyl groups, respectively (Figure 3.23a).

Direct surface modification of boron/iron oxide core/shell nanostructure with citric acid was attempted instead of a ligand exchange reaction with oleic acid (Figure 3.24). The resulting product contains the same ATR-FTIR peaks as the ligand exchange reaction, confirming a

successful product formation. A direct functionalization can reduce the number of steps and chemicals consumed to achieve a citric acid functionalized boron/iron oxide core/shell nanoparticles.

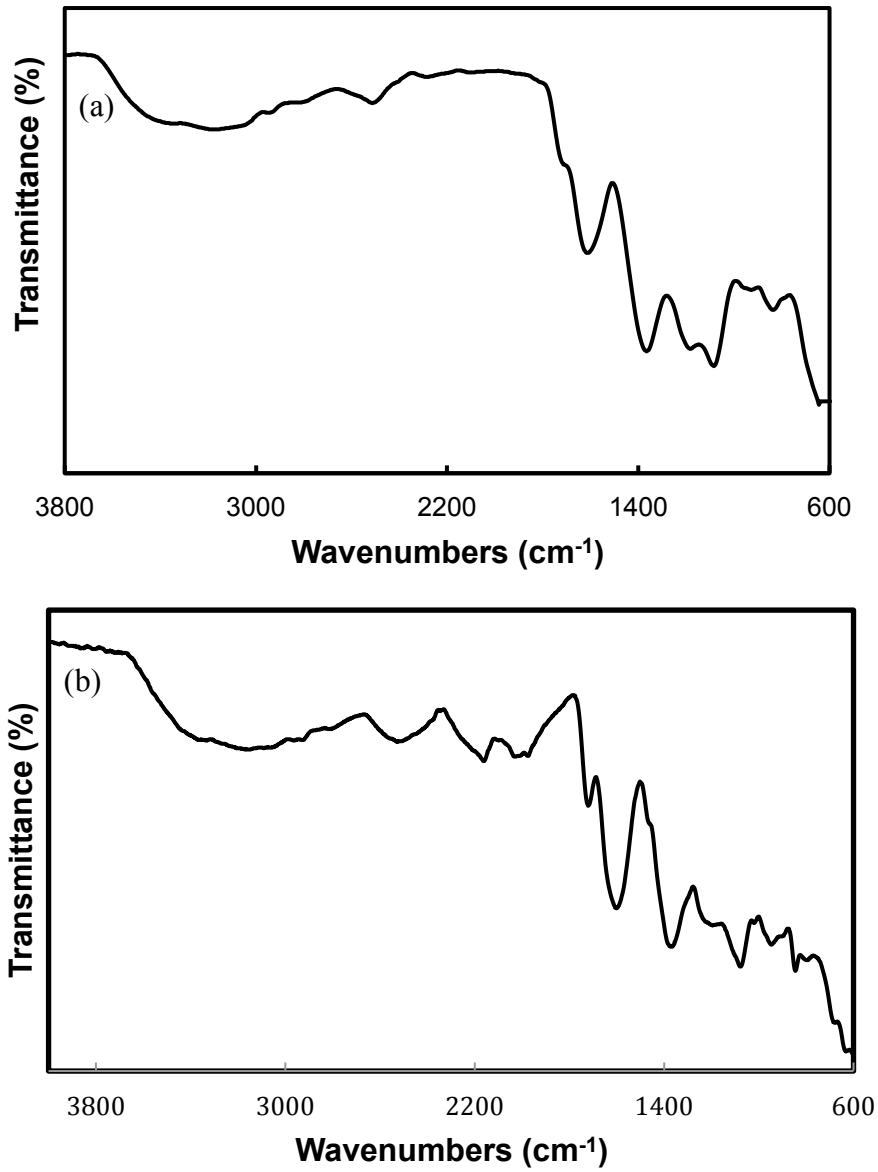

Figure 3.23: ATR-FTIR spectrum of citric acid functionalized boron/iron oxide core/shell nanoparticles prepared via (a) ligand exchange reaction and (b) direct surface functionalization.

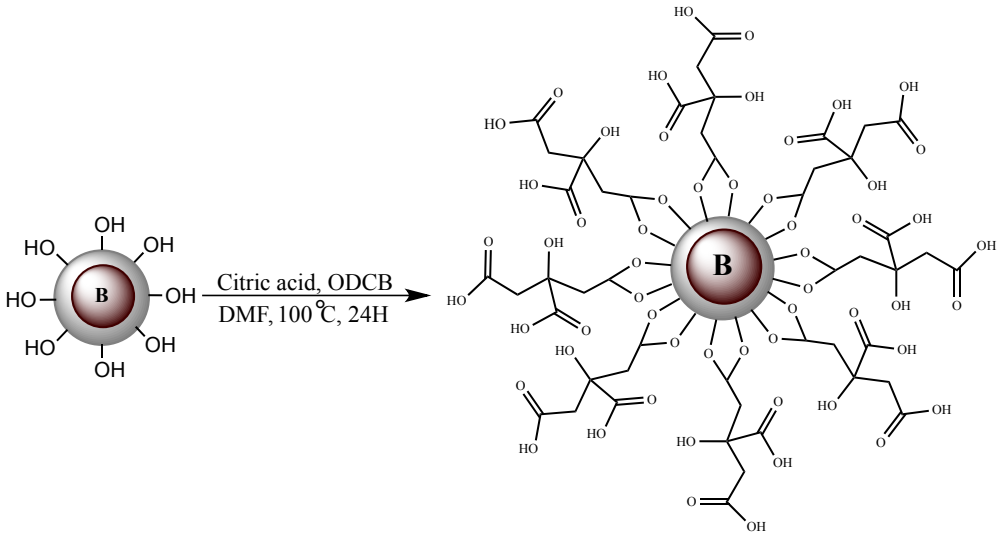

Figure 3.24: Synthesis of citric acid functionalized boron/iron oxide core/shell nanoparticle.

3.3.4.3 Reaction with Amine-Terminated PEG

The sequential functionalization of boron/iron oxide core/shell nanoparticles in a two-step process by reacting with citric acid and amine-terminated PEG produced water-soluble nanoparticles (Figure 3.25).[24] The final functionalization step included an EDC-assisted amidation reaction between amine-terminated PEG and the free carboxyl (COOH) groups of citric acid on the surface of boron/iron oxide core/shell nanostructure. EDC and NHS activate the carboxyl group of citric acid to form amides.

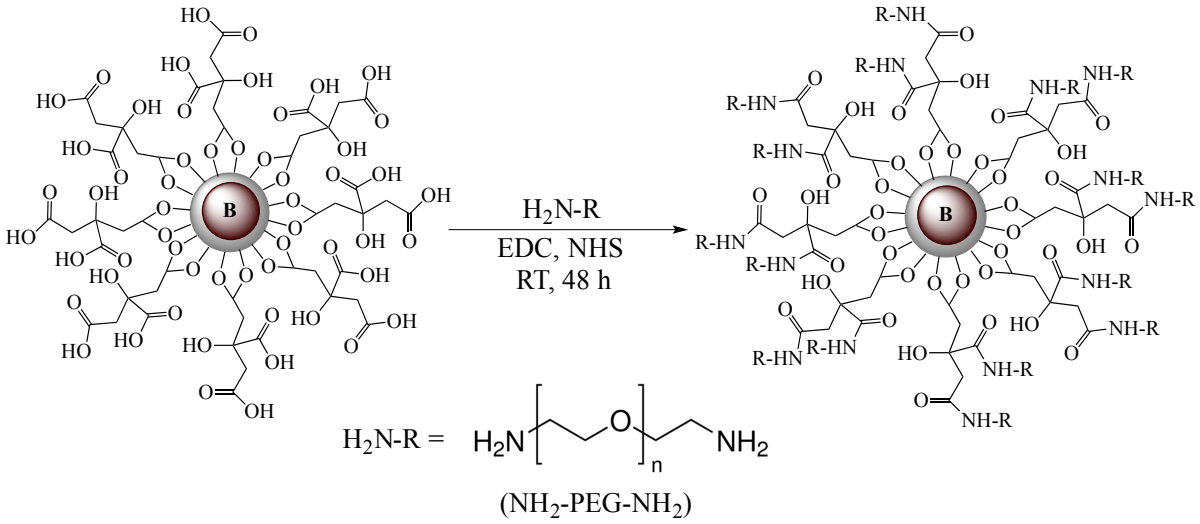

Figure 3.25: Synthesis of water-soluble boron/iron oxide core/shell nanoparticle.

The ATR-FTIR spectrum peaks at 1626 cm^{-1} and 1703 cm^{-1} correspond to carboxyl groups of citric acid (Figure 3.26). On the other hand, peaks at 2880 cm^{-1} and 3306 cm^{-1} are due to aliphatic C-H bonds and amine groups, respectively. All of the functionalized boron/iron oxide core/shell nanoparticles maintained quasi-spherical morphology as evident from TEM images (Figure 3.27). The final product was found soluble in aqueous media.

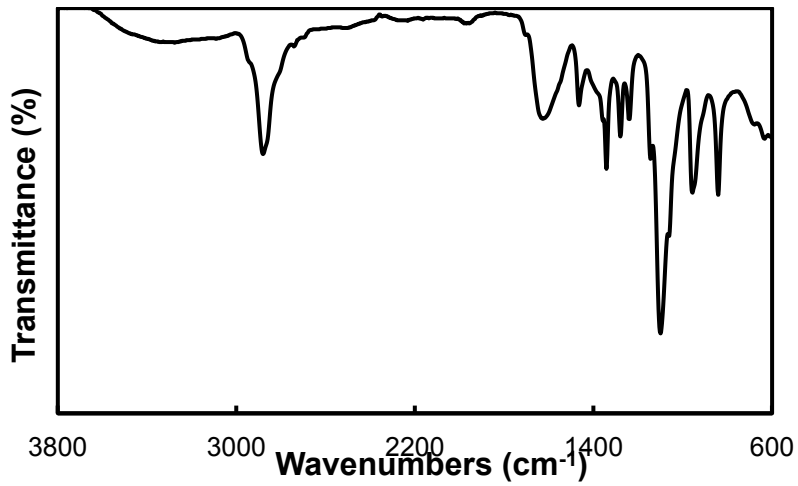

Figure 3.26: ATR-FTIR spectrum of amine-terminated PEG functionalized boron/iron oxide core/shell nanoparticles.

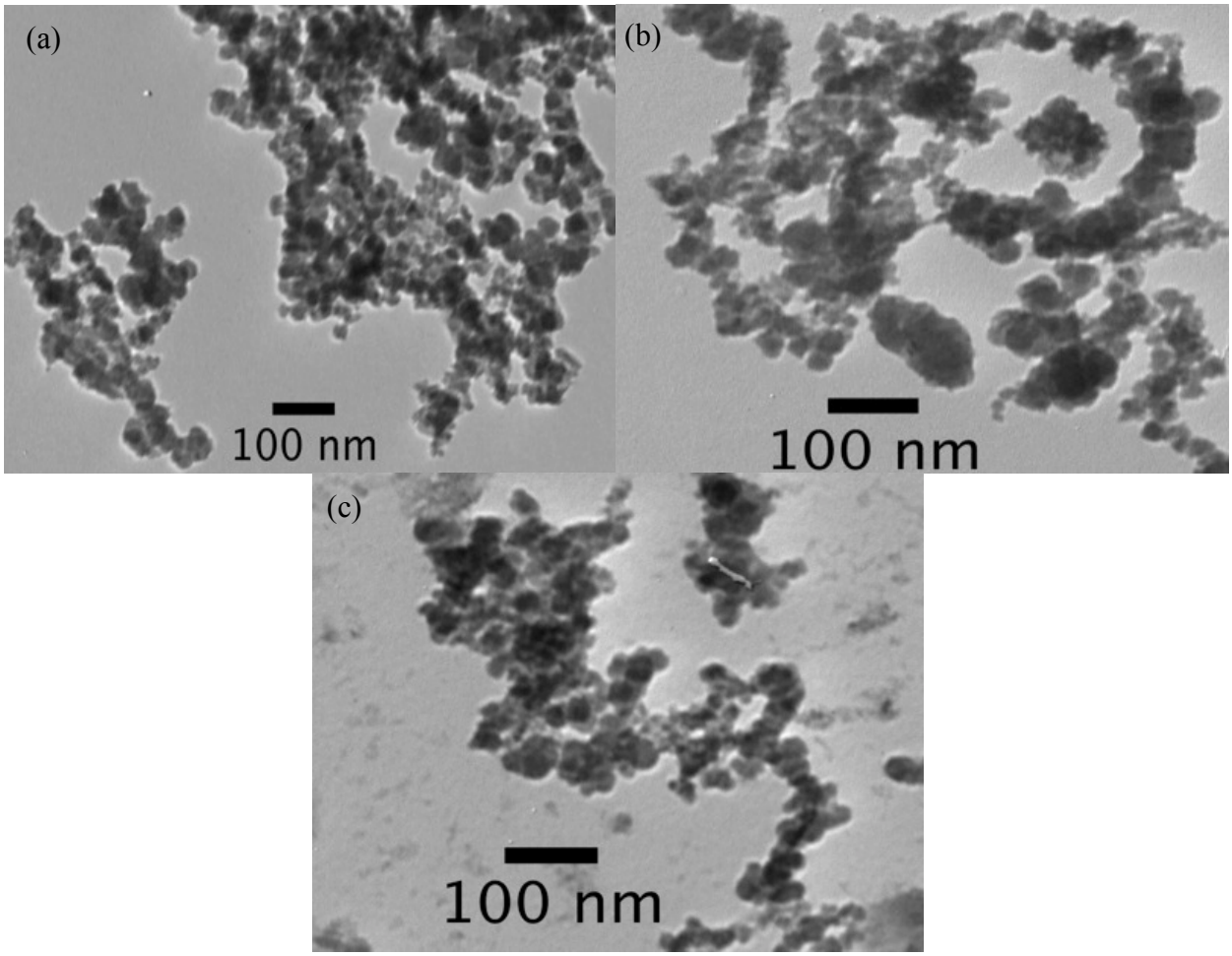

Figure 3.27**:** TEM image of (a) oleic acid functionalized boron/iron oxide core/shell nanoparticles, (b) citric acid functionalized boron/iron oxide core/shell nanoparticles, and (c) amine-terminated PEG functionalized boron/iron oxide core/shell nanoparticles.

3.3.4.4 Reaction with Dopamine

Functionalization of the core/shell nanoparticles with dopamine using ligand exchange reaction with oleic acid[25] as well as direct surface attachment[26] was successful (Figure 3.28). The ligand exchange reaction is similar to the previously mentioned reaction between oleic acid and citric acid. In this case, an excess amount of dopamine was used to guarantee the replacement of

oleic acid with dopamine. The TEM image shows that the product contained nanoparticles (Figure 3.29).

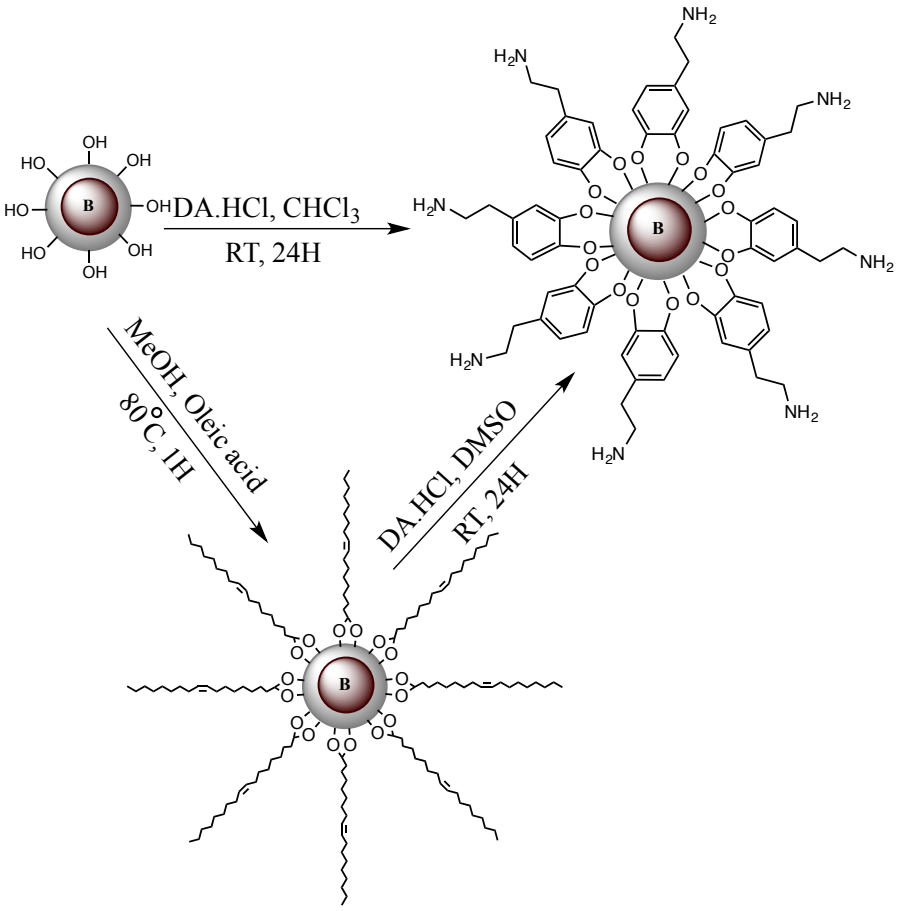

Figure 3.28: Synthesis of dopamine functionalized boron/iron oxide core/shell nanoparticle.

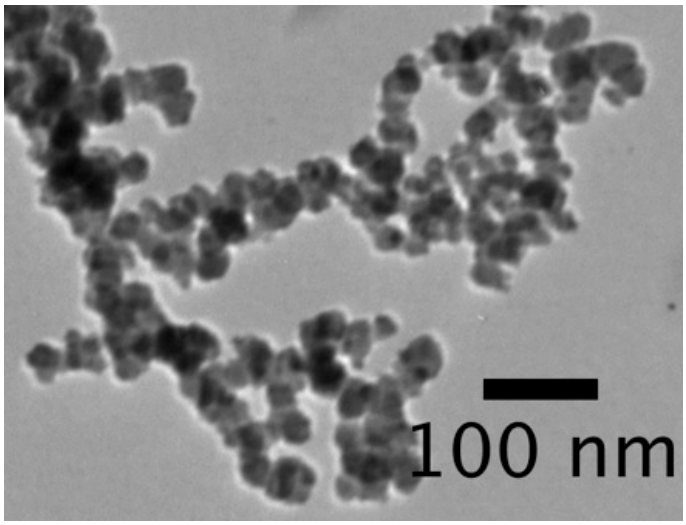

Figure 3.29**:** TEM image of dopamine functionalized boron/iron oxide core/shell nanoparticles.

Ultraviolet-visible spectroscopy (UV-Vis) analysis of the sample supports the functionalization of the core/shell nanoparticles (Figure 3.30). Pure dopamine has a UV-Vis absorption peak around 280 nm and the modified particles also have a peak at the same wavelength but the peak is much broader than pure dopamine which is caused by the scattering of nanoparticles.

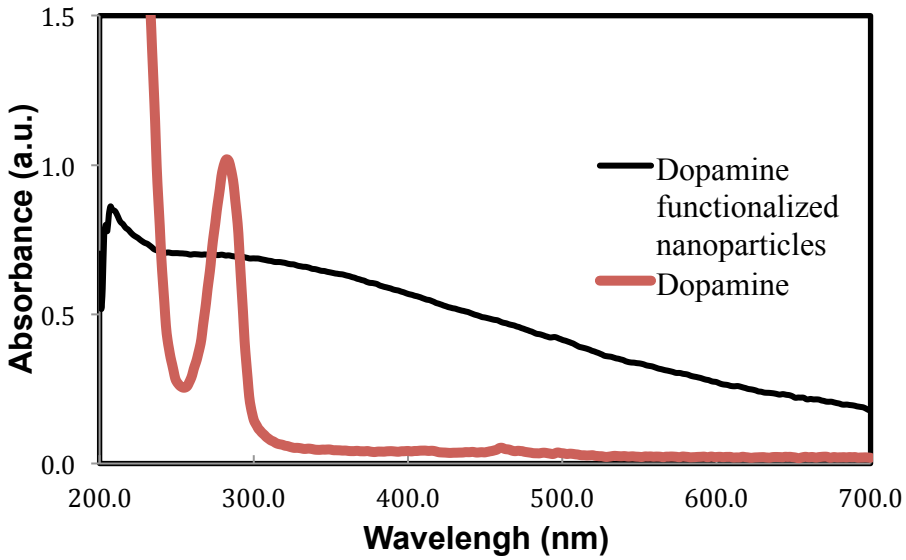

Figure 3.30**:** UV-Vis spectrum of dopamine functionalized boron/iron oxide core/shell nanoparticles.

3.3.4.5 Reaction with Folic Acid

Surface modification of the nanoparticles with folic acid without any intermediates was not effective. However, functionalization of boron/iron oxide nanoparticles with folic acid was accomplished via EDC-amidation reaction with dopamine. EDC-amidation reaction uses NHS and EDC to activate carboxyl groups of folic acid to form amide bonds with the amine moiety of dopamine (Figure 3.31). TEM image of the product confirmed the presence of quasi-spherical nanoparticles (Figure 3.32).

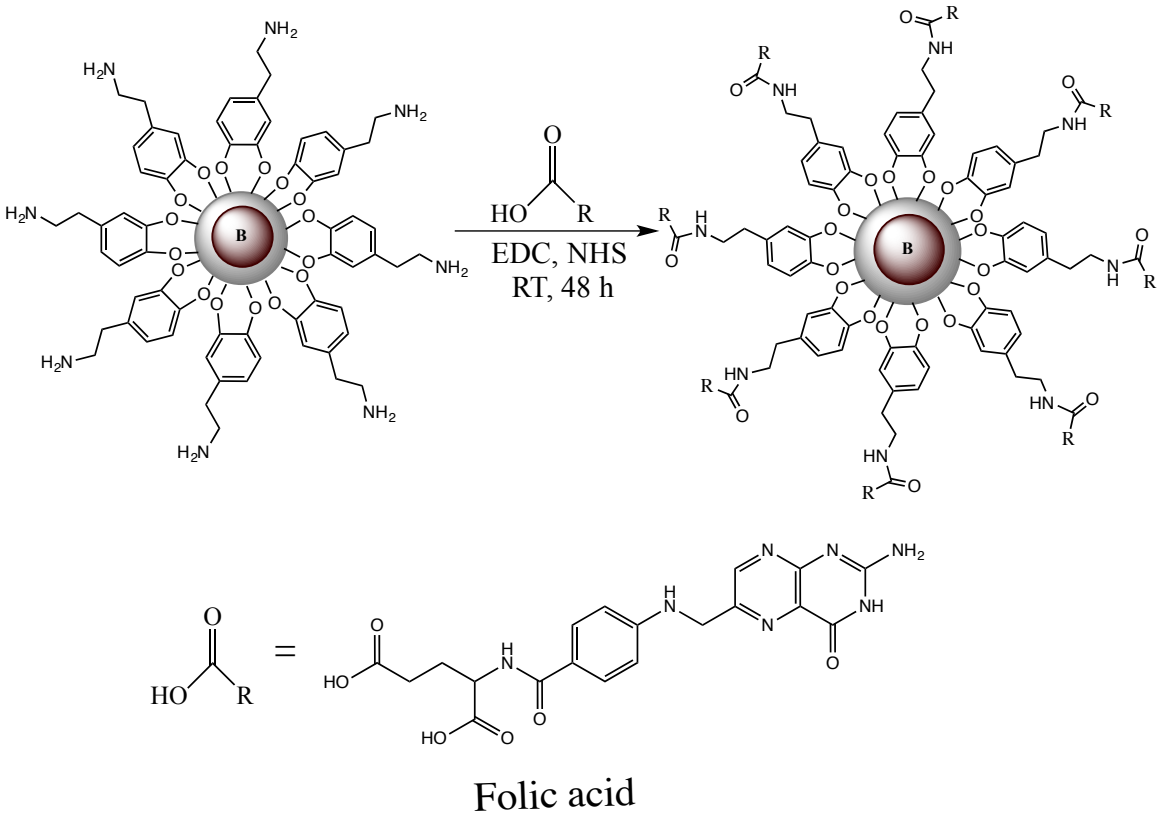

Figure 3.31: Synthesis of folic acid functionalized boron/iron oxide core/shell nanoparticle.

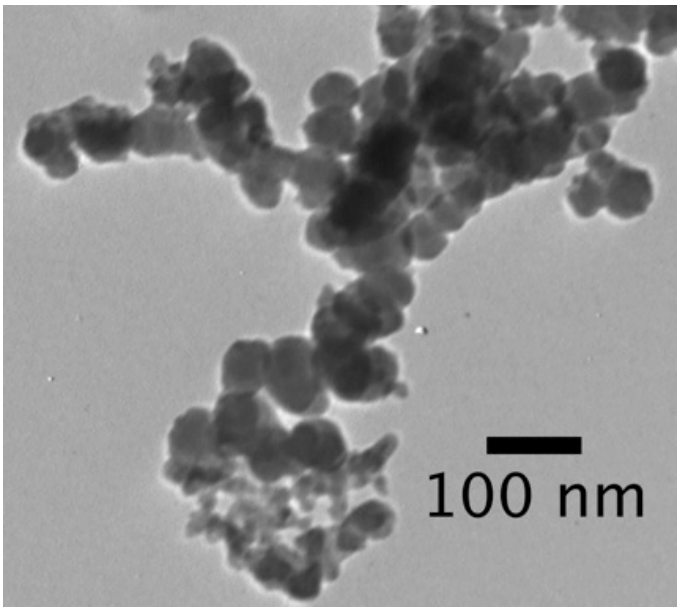

Figure 3.32: TEM image of folic acid functionalized boron/iron oxide core/shell nanoparticles.

UV-Vis analysis of the product shows two UV-Vis absorption peaks at 280 nm and 350 nm corresponding to folic acid. Both dopamine and folic acid have peaks around 280 nm; therefore, it is difficult to pinpoint if the peak is due to dopamine or folic acid. However, the shoulder peak at 350 nm can only arise from folic acid (Figure 3.33).

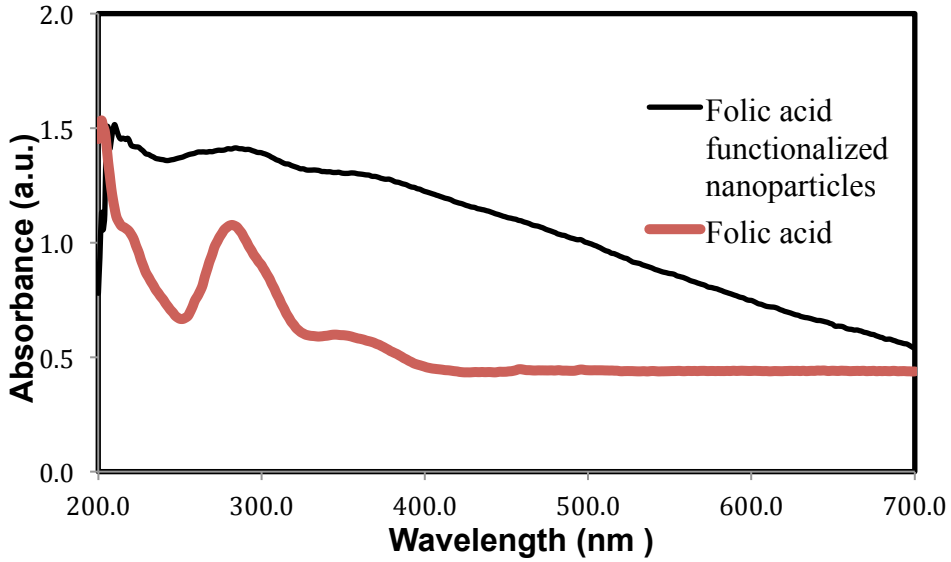

Figure 3.33: UV-Vis spectrum of folic acid functionalized boron/iron oxide core/shell nanoparticles.

3.3.4.5 Reaction With Starch

Starch-coated boron/iron oxide nanoparticles were prepared via direct surface modification using the hydroxyl group present on a starch molecule.[27] The hydroxyl oxygen forms a bond with the iron on the surface of the core/shell structure, which then creates a linkage between the nanoparticles and the starch molecule. TEM image of the final product indicated the product is composed of nanoparticles (Figure 3.34).

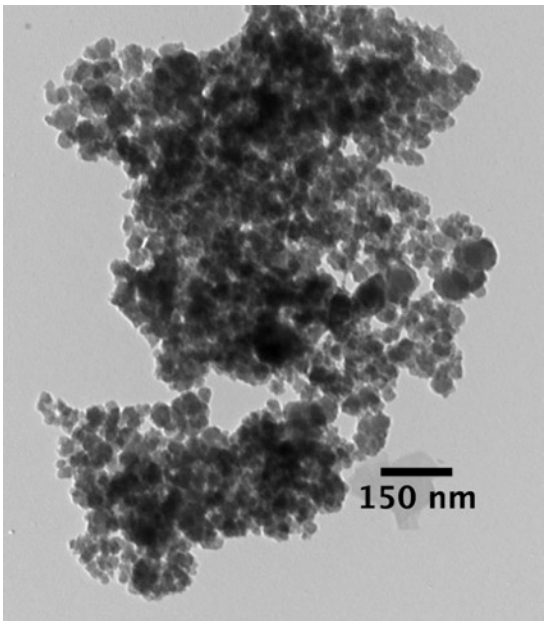

Figure 3.34**:** TEM image of starch functionalized boron/iron oxide core/shell nanoparticles.

An ATR-FTIR spectrum of the final product shows peaks at 1009 cm^{-1}, 1077 cm^{-1}, 1145 cm^{-1}, 1339 cm^{-1}, 2925 cm^{-1} and 32676 cm^{-1} correspond to C-O-C, C-O-H, C-C, C-O, C-H, and O-H, respectively (Figure 3.35). This peaks confirmed the functionalization of the core/shell nanoparticles with starch.

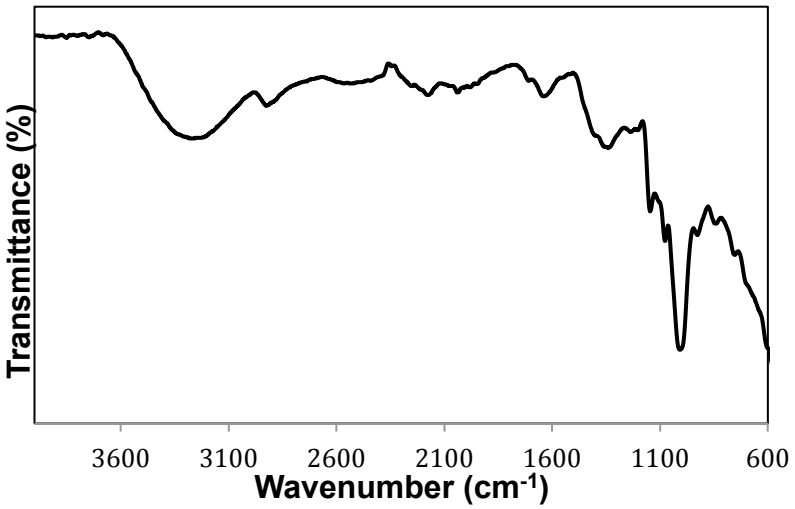

Figure 3.35: ATR-FTIR spectrum of starch functionalized boron/iron oxide core/shell nanoparticles.

3.3.4.5 Reaction with α-D Glucose

Oleic acid-coated boron/iron oxide nanoparticles were used to perform a ligand exchange reaction with α-D glucose, which replaced oleic acid with α-D glucose (Figure 3.36).[28] The presence of glucose on the surface of the core/shell nanoparticles will increase the consumption of these particles by cancer cells since cancer cells require a large amount of glucose to divide and grow. TEM image of the final product indicated the product is composed of nanoparticles (Figure 3.37).

ATR-FTIR spectrum of the product shows peaks at 1105 cm^{-1}, 1144 cm^{-1}, 1220 cm^{-1}, 1336 cm^{-1}, 1447 cm^{-1}, 2940 cm^{-1}, and 3301 cm^{-1} correspond to C-O, C-C, C-H, C-CH, O-CH, C-H, and O-H, respectively (Figure 3.38).

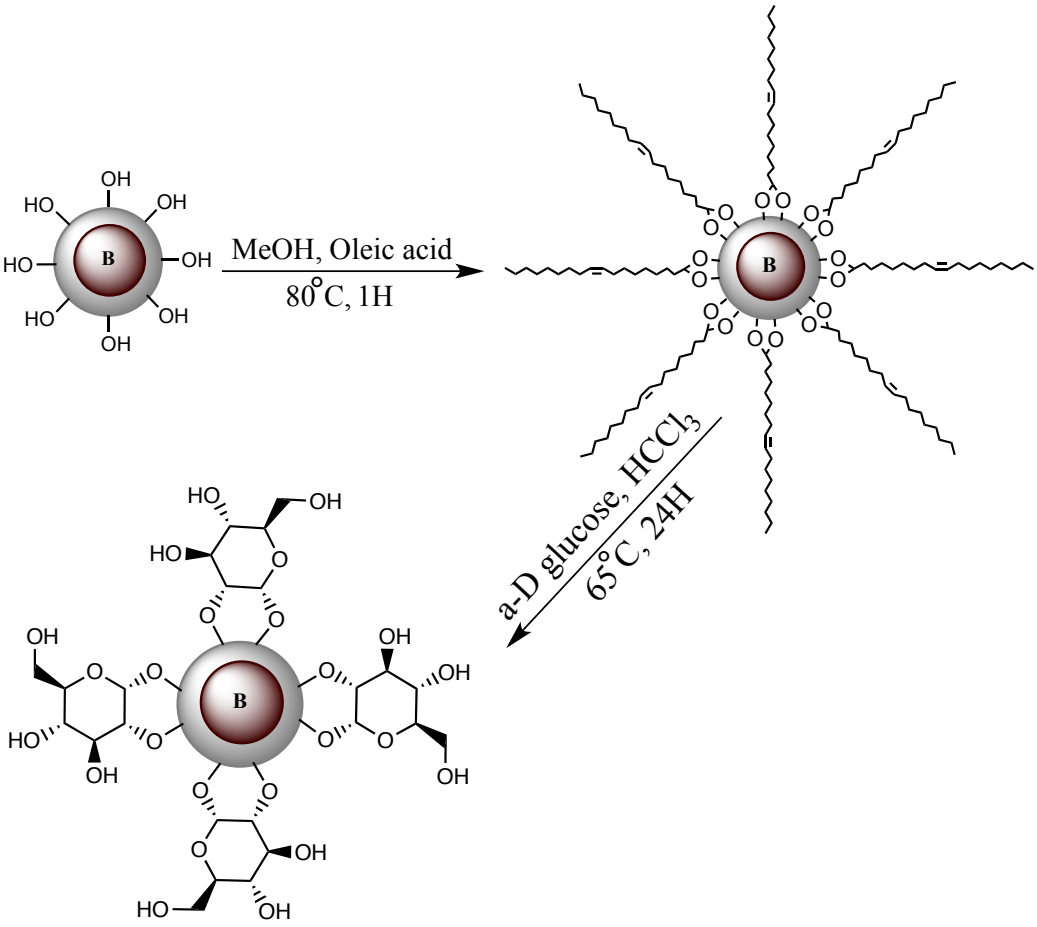

Figure 3.36: Synthesis of α-D glucose functionalized boron/iron oxide core/shell nanoparticle.

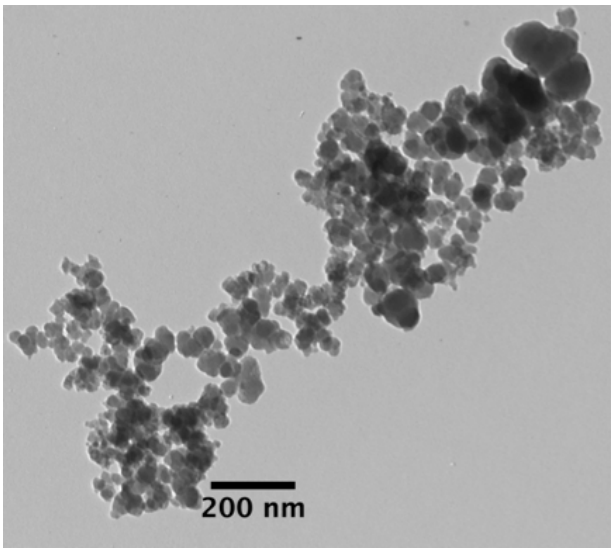

Figure 3.37**:** TEM image of α-D glucose functionalized boron/iron oxide core/shell nanoparticles.

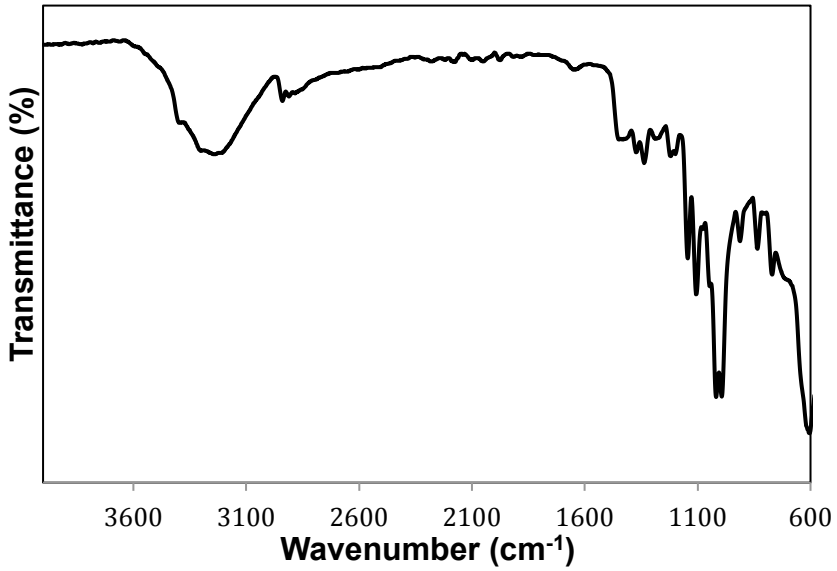

Figure 3.38: ATR-FTIR spectrum of α-D glucose functionalized boron/iron oxide core/shell nanoparticles.

3.3.5 Magnetic Studies

The magnetic property of boron/iron oxide core/shell nanoparticles and amine-terminated boron/iron oxide core/shell nanoparticles were analyzed at room temperature. The linear magnetization curve for the core/shell nanoparticles revealed the nanoparticles were paramagnetic. However, the functionalized core/shell nanoparticles were *soft* ferromagnetic with a nonlinear magnetization curve and have a saturation value of 1.93×10^{-4} emu (Figure 3.39). In other word, the core/shell nanoparticles were magnetic when an external magnetic field was applied whereas the functionalized core/shell nanoparticles maintained a permanent magnetic moment in the absence of external magnetic field. Identification of the functionalized core/shell nanoparticles as *soft* ferromagnetic materials was based on the small area within the loop of the magnetization hysteresis. The result supports that the water-soluble nanoparticles can be guided to cancer cells using an external magnetic field.

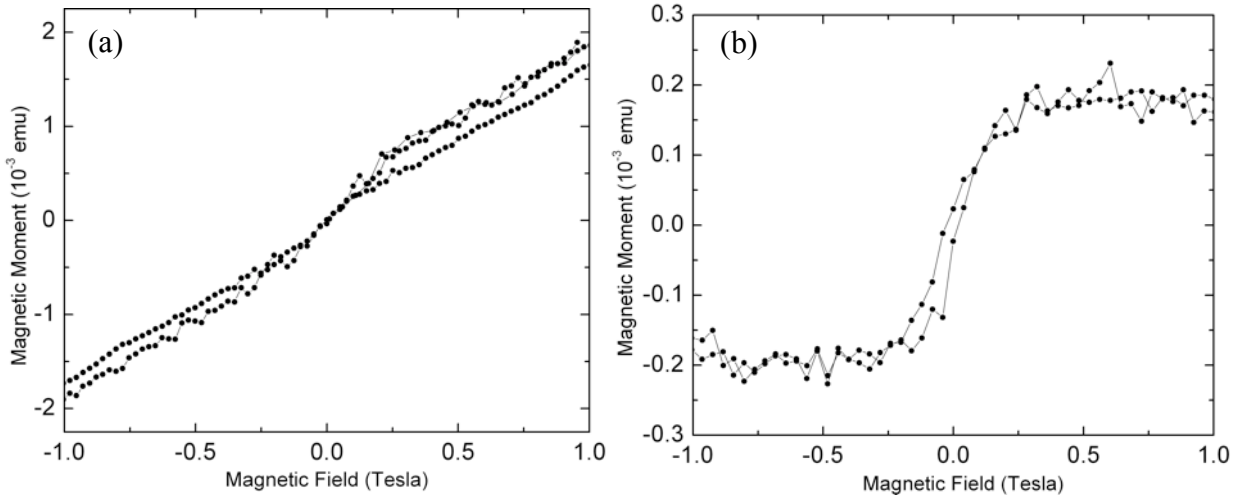

Figure 3.39: Magnetic hysteresis curve of (a) boron/iron oxide core/shell nanoparticles and (b) amine-terminated PEG functionalized boron/iron oxide core/shell nanoparticles.

3.3.6 Biological Studies

Citric acid functionalized boron/iron oxide core/shell nanoparticles (Sample 1) were not readily soluble in the PBS; as a result, a small amount of DMSO was added to increase the solubility. In contrast, the amine-terminated PEG functionalized core/shell nanoparticles (Sample 2) were soluble in PBS and did not require the addition of DMSO. Furthermore, Sample 1 was light yellow after filtration indicating most of the black-coloured nanoparticles were not passed through the filter (Figure 3.40). Both folic acid and dopamine functionalized boron/iron oxide core/shell nanoparticles were found to be nontoxic with IC_{50} value greater than 1μg/mL.

The concentration of the samples was calculated using both the PBS and DMSO; the results are 201.2 μg/μL and 276.0 μg/μL for Samples 1 and 2, respectively. Figure 3.41 shows the 12 different concentrations with natural red dye that were done in duplicates as well as a control with PBS.

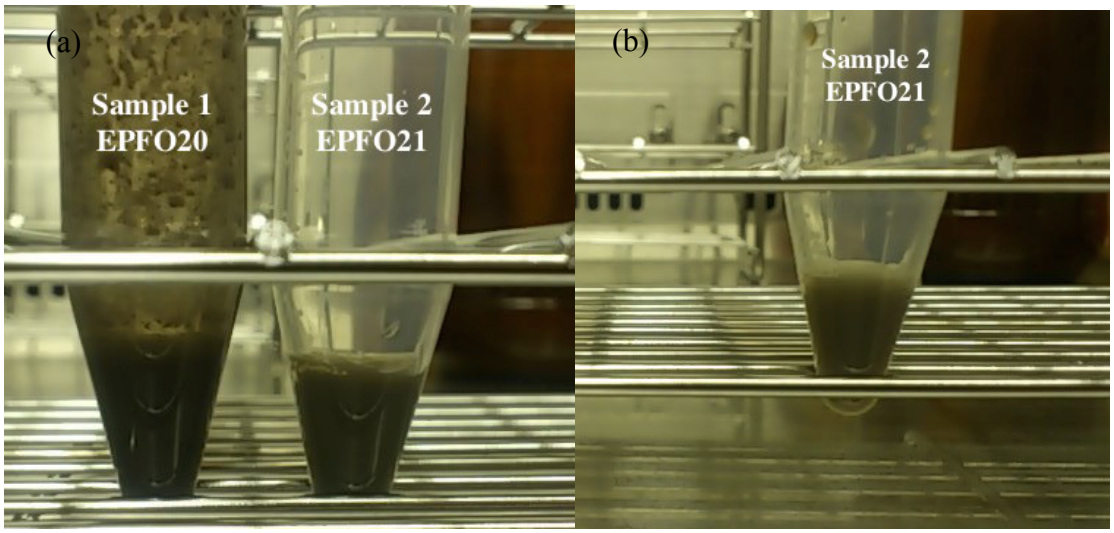

Figure 3.40: Image of Samples 1 and 2 (a) before filtration and (b) after filtration.

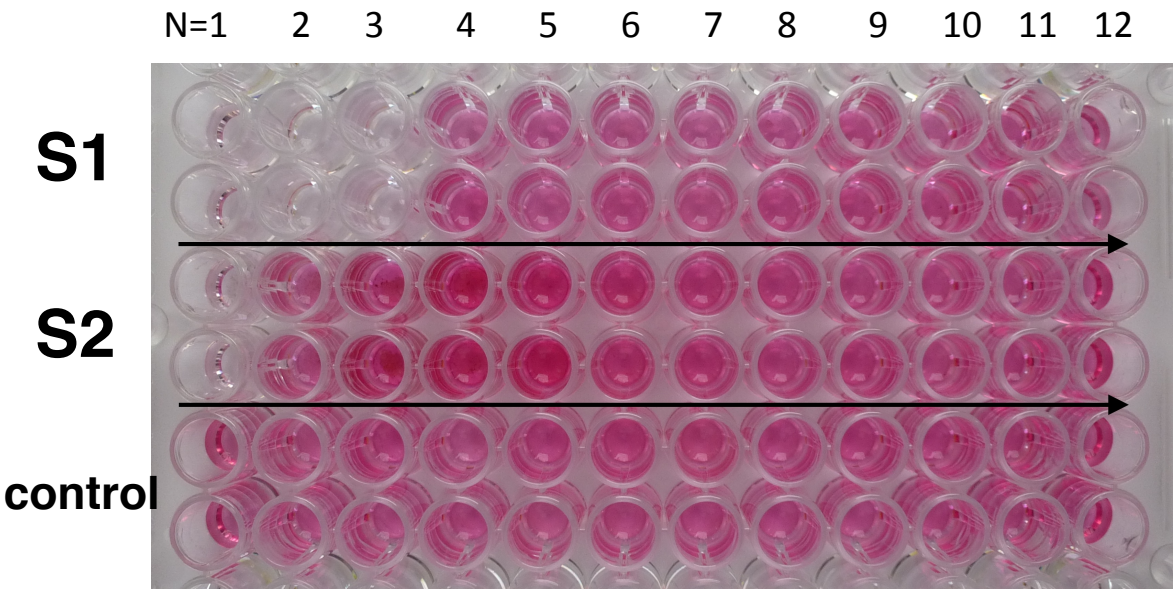

Figure 3.41: Image of Samples 1, 2, and control with the natural red dye.

The UV-Vis spectrum allows the determination of titer (n), which was used to calculate the IC_{50} values (Figure 3.42). Once the titer was known, the IC_{50} values were calculated as follow:

Sample 1, n=3.50

$201.2\ \mu g/\mu L \times 0.5 \times (1/2)^{n-1}$ n=3.50 = 17.8 µg/µL

Sample 2, n=1.81

$276.0\ \mu g/\mu L \times 0.5 \times (1/2)^{n-1}$ n=1.81 = 79.3 µg/µL

Therefore, the final IC_{50} values are 17.8 µg/µL and 79.3 µg/µL for citric acid and amine-terminated PEG functionalized boron/iron oxide core/shell nanoparticles, respectively. The absorbance (OD) vs. titer (n) plot had a typical sigmoid curve for Sample 1. However, Sample 2 did not exhibit a similar curve and the reason for this characteristic curve is under investigation.

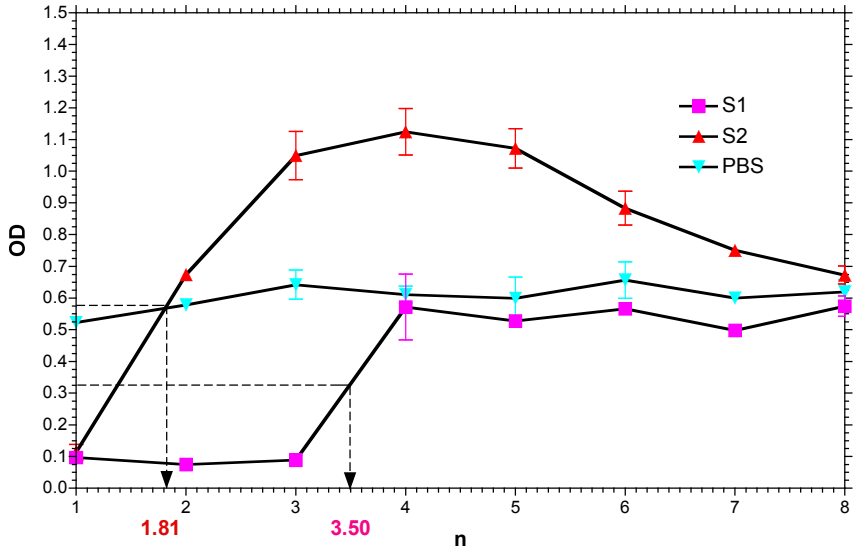

Figure 3.42: Plot of absorbance (OD) vs. titer (n) of amine-terminated PEG functionalized boron/iron oxide core/shell nanoparticles.

3.4 Summary and Conclusion

Synthesis of boron nanoparticles was accomplished via pyrolysis to produce boron nanoparticles with high purity. In addition, direct surface modification of the nanoparticles with bromine was performed to incorporate greater than 4% atomic weight of bromine. Furthermore, a core/shell structure of boron/iron oxide was synthesized and functionalized in two or three steps using oleic acid, citric acid, and amine-terminated PEG to produce water-soluble nanoparticles. Additional surface modification of the core/shell nanoparticles with dopamine, folic acid, starch, and α-D glucose was successful. The nanoparticles maintained quasi-spherical morphology even after surface modification. The products were characterized and found to be of high purity. Cytotoxicity studies of amine-terminated PEG, folic acid, and dopamine functionalized boron/iron oxide core/shell nanoparticles showed the compounds are not toxic to normal cells.

References

1. Chatterjee, K.; Sarkar, S.; Jagajjanani Rao, K.; Paria, S.; Core/Shell Nanoparticles In Biomedical Applications. *Advances in Colloid and Interface Science*, **2014**, 209, 8-39.

2. Gupta, A. K., Mona Gupta, M., Synthesis and surface engineering of iron oxide nanoparticles for biomedical applications. *Biomaterials*, **2005**, 26, 3995–4021.

3. Laurent, S.; Forge, D.; Port, M.; Roch, A.; Robic, C.; Vander Elst, L.; Muller, R.; Magnetic Iron Oxide Nanoparticles: Synthesis, Stabilization, Vectorization, Physicochemical Characterizations, And Biological Applications. *Chem. Rev.,* **2008**, *108*, 2064-2110.

4. Li, W.; Tutton, S.; Vu, A.; Pierchala, L.; Li, B.; Lewis, J.; Prasad, P.; Edelman, R.; First-Pass Contrast-Enhanced Magnetic Resonance Angiography In Humans Using Ferumoxytol, A Novel Ultrasmall Superparamagnetic Iron Oxide (USPIO)-Based Blood Pool Agent. *Journal of Magn. Reson. Imaging,* **2005**, *21*, 46-52.

5. McLachlan, S.; Morris, M.; Lucas, M.; Fisco, R.; Eakins, M.; Fowler, D.; Scheetz, R.; Olukotun, A.; Phase I Clinical Evaluation Of A New Iron Oxide MR Contrast Agent. *J. Magn. Reson. Imaging,* **1994**, *4*, 301-307.

6. Reimer, P.; Marx, C.; Rummeny, E.; Müller, M.; Lentschig, M.; Balzer, T.; Dietl, K.; Sulkowski, U.; Berns, T.; Shamsi, K.; Peters, P. E.; SPIO-Enhanced 2D-TOF MR Angiography Of The Portal Venous System: Results Of An Intraindividual Comparison. *J. Magn. Reson. Imaging,* **1997**, *7*, 945-949

7. Simon, G.; von Vopelius-Feldt, J.; Fu, Y.; Schlegel, J.; Pinotek, G.; Wendland, M.; Chen, M.; Daldrup-Link, H. Ultrasmall Supraparamagnetic Iron Oxide-Enhanced Magnetic Resonance Imaging Of Antigen-Induced Arthritis**:** a comparative study between SHU 555 C, ferumoxtran-10, and ferumoxytol. *Invest. Radiol.,* **2006**, *41*, 45-51.

8. Taupitz, M.; Wagner, S.; Schnorr, J.; Kravec, I.; Pilgrimm, H.; Bergmann-Fritsch, H.; Hamm, B.; Phase I Clinical Evaluation Of Citrate-Coated Monocrystalline Very Small Superparamagnetic Iron Oxide Particles As A New Contrast Medium For Magnetic Resonance Imaging. *Invest. Radiol.,* **2004**, *39*, 394-405.

9. Kohler, N.; Sun, C.; Fichtenholtz, A.; Gunn, J.; Fang, C.; Zhang, M.; Methotrexate-Immobilized Poly(Ethylene Glycol) Magnetic Nanoparticles For MR Imaging And Drug Delivery. *Small,* **2006**, *2*, 785-792.

10. Gallo, J. M; Varkonyi, P.; Hassan, E. E; Groothius, D. R.; Targeting Anticancer Drugs To The Brain: II. Physiological Pharmacokinetic Model Of Oxantrazole Following Intraarterial Administration To Rat Glioma-2 (RG-2) Bearing Rats. *J. Pharmacokinet. Biopharm.,* **1993**, *21*, 575-592.

11. Zhu, Y.; Lin, Y.; Zhu, Y. Z.; Lu, J.; Maguire, J. A; Hosmane, N. S.; Boron Drug Delivery Via Encapsulated Magnetic Nanoparticless: A New Approach For BNCT In Cancer Treatment. *J. Nanomater*., **2010**, 1-8.

12. He, X.: Joo, S.: Liang, H., Boron-Based Nanoparticles for Chemical-Mechanical Polishing of Copper Films. *ECS Journal of Solid State Science and Technology,* **2013**, 2 (1), 20-25.

13. Bellott, B. J.; Noh, W.; Nuzzo, R.G.; Girolami, G.S., Nanoenergetic materials: boron nanoparticles from the pyrolysis of decaborane and their functionalization. *Chem. Commun.,* **2009**, 3214–3215

14. Perez, P.L.; McMahon, B.W.; Schneider, S.; Boatz, J.A.; Hawkins, T.W.; McCrary, P.D.; Beasley, P.A.; Kelley, S.P.; Rogers, R.D, Anderson, S.L., Exploring the Structure of Nitrogen-Rich Ionic Liquids and Their Binding to the Surface of Oxide-Free Boron Nanoparticles. *J. Phys. Chem. C,* **2013**, 117, 5693−5707.

15. Si, P. Z.; Zhang, M.; You, C. Y.; Geng, D. Y.; Du, J. H; Zhao, X. G.; Ma, X. L.; Zhang, Z. D., Amorphous boron nanoparticles and BN encapsulating boron nano-peanuts prepared by arc-decomposing diborane and nitriding. *J. Mater. Sci.* **2003,** 38, 689– 692.

16. Bellott, B. J.; Noh, W.; Nuzzo, R.G.; Girolami, G.S.; *Chem. Commun,* **2009**, 3214–3215.

17. Devener, B.V.; Perez, P.L.; Anderson, S.L.; *J. Mater. Res.,* **2009**, 24 (11), 3462-3464.

18. Chakrabarti, A.; Xu, T.; Paulson, L. K.; Krise, K. J.; Maguire, J. A.; Hosmane, N. S. *J. Nanomater*., **2010**, 1-5.

19. Gao, S.; Liu, X.; Xu, T.; Ma, X.; Shen, Z.; Wu, A.; Zhu, Y.; Hosmane, N.S; *ChemistryOpen* **2013**, 2, 88 – 92.

20. Grosvenor, A. P.; Kobe, B. A.; Biesinger,M. C.; McIntyre, N. S; *Surf. Interface Anal.* **2004**, 36, 1564–1574.

21. Xie, S.; Wang, W.; Fernando, K.; Wang, X.; Lin, Y.; Sun, Y.; Solubilization Of Boron Nitride Nanotubes. *Chem. Commun.* **2005**, 3670-3672.

22. Sun, Y.; Ding, X.; Zheng, Z.; Cheng, X.; Hu, X.; Peng, Y.; Magnetic Separation Of Polymer Hybrid Iron Oxide Nanoparticles Triggered By Temperature. *Chem. Commun.,* **2006**, 2765-2767.

23. Patil, R. M; Shete, P. B.; Thorat, N. D; Otari, S. V.; Barick, K. C.; Prasad, A.; Ningthoujam, R. S.; Tiwale, B. M.; Pawar, S. H.;Non-Aqueous To Aqueous Phase Transfer Of Oleic Acid Coated Iron Oxide Nanoparticles For Hyperthermia Application. *RSC Adv.,* **2014**, *4*, 4515-4522.

24. Lattuada, M.; Hatton, T. A.; *Langmuir,* **2007,** 23*,* 2158-2168.

25. Korpany, K.; Habib, F.; Murugesu, M.; Blum, A. Stable Water-Soluble Iron Oxide Nanoparticles Using Tiron. *Mater. Chem. Phys.,* **2013**, *138*, 29-37.

26. Wang, Z.; Zhu, J.; Chen, Y.; Geng, K.; Qian, N.; Cheng, L.; Lu, Z.; Pan, Y.; Guo, L.; Li, Y.; Gu, H.; Folic Acid Modified Superparamagnetic Iron Oxide Nanoparticless For Targeted Hepatic Carcinoma MR Imaging. *RSC Advances,* **2014**, *4*, 7483-7490.

27. Jafarpour, M.; Rezaeifard, A.; Yasinzadeh, V.; Kargar, H. Starch-Coated Maghemite Nanoparticles Functionalized By A Novel Cobalt Schiff Base Complex Catalyzes Selective Aerobic Benzylic C–H Oxidation. *RSC Adv.* **2015**, *5*, 38460-38469.

28. Huang, J.; Wang, L.; Lin, R.; Wang, A.; Yang, L.; Kuang, M.; Qian, W.; Mao, H. Casein-Coated Iron Oxide Nanoparticles For High MRI Contrast Enhancement And Efficient Cell Targeting. *ACS Appl. Mater. Interfaces,* **2013**, *5*, 4632-4639.

CHAPTER 4

SYNTHESIS AND FUNCTIONALIZATION OF BORON/SILICA CORE/SHELL NANOPARTICLES

4.1 Introduction

The importance of core/shell structures in general is discussed in the introduction to Chapter 3. Therefore, we will focus on the benefit of silica-based core/shell nanoparticles. Mesoporous silica nanoparticles were first discovered in the 1970's but did not gain any attention until the 1990's.[1] Silica, also known as silicon dioxide, can be synthesized using three different methods, namely, chemical vapor deposition (CVD), reverse microemulsion, and sol-gel. CVD method utilizes high temperature and volatile liquids such as silicon tetrachloride. On the other hand, reverse microemulsion uses surfactant to form micelles in the presence of water. Under normal conditions the hydrophilic head of the micelle will orient itself to be exposed to the surroundings. However, in reverse microemulsion the hydrophilic head is inside while the hydrophobic tail is exposed and the silica nanoparticles are formed in the hydrophilic cavity. The last method is sol-gel or Stöber process, which follows two steps: hydrolysis and condensation (Figure 4.1). First, the hydrolysis of silica source by alcohol occurs; then the addition of a base or acid to the system leads to condensation of silicon alkoxides, usually tetraethoxysilane.[2] The first two methods are expensive and in reverse microemulsion the removal of the surfactant is mostly

difficult. Therefore, sol-gel process is the extensively used approach to synthesizing silica nanoparticles or silica-based core/shell nanoparticles.[3]

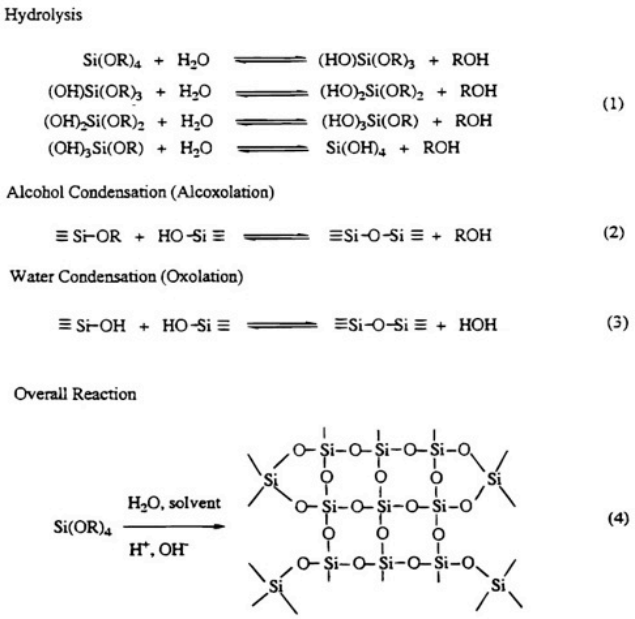

Figure 4.1: Synthesis of silica nanoparticles via sol-gel process.[3]

Silica nanoparticles have been used in polymer nanocomposites to increase fracture toughness, deformation resistance,[4] dielectric constant, thermal stability,[5] microhardness,[6] elasticity, yield and storage modulus,[7,8] as well as tensile and peel strength.[8] In addition, fluorescent dye-tagged mesoporous silica or silica nanoparticles can be used for biomedical applications to image cancer cells,[9] study interactions between ligand and receptors,[10,11] identify pathogens,[11-13] and deliver drugs.[14] Silica nanoparticles that are functionalized with ligands like hyaluronic acid and folic acid can be used for targeting cell lines that contain receptor sites for these molecules. Targeting drug delivery can accumulate a large concentration of functionalized particles in cancer cells since there is an overexpression of receptor sites.[15]

Fan et al. reported the use of mesoporous silica-coated $NaYF_4$:Yb/Er/Tm/Gd upconversion nanoparticles to deliver mitomycin C (MMC) to the nuclei of breast cancer cells (MCF-7) and drug-resistant MCF-7 (MCF-7/ADR).[16] Mitomycin is an anti-cancer drug used to treat anal, breast, and bladder cancer by triggering cell death via DNA crosslinking. The mitomycin C was loaded into the mesoporous silica structure and the core/shell structure was functionalized with adenosine-5'-(γ-thio)-triphosphate ligand which improves the uptake of the compound into the cell. The *in vivo* result showed the cell uptake was greater than 4.35% ID/g and the cell death increased significantly after X-ray radiation.

Silica nanostructures are generally nontoxic and biocompatible. However, the particle size plays an important role in determining cytotoxicity and cellular uptake of the compound. For example, the uptake of mesoporous silica by Hela cells was determined to be the highest when the mesoporous silica has a diameter of 50 nm comparing to a diameter of 30 nm, 110 nm, and 280 nm nanoparticles.[17] Furthermore, the compounds' retention time in different organs increases as the particle size decreases;[18] also cytotoxicity of the nanoparticles is higher than those of microscale particles.[19] In addition to particle size other parameters such as surface modification also have a large influence in cytotoxicity and uptake. For instance, polyethylene glycol functionalized silica nanoparticles can stay in the blood for an extended period of time with limited removal of the particles from the body.[18, 20- 22]

The synthesis of boron/silica core/shell nanoparticles and surface modification of the core/shell nanoparticles with organic moieties like 3-(amino propyl) triethoxy silane, 3-(2-aminoethyleamino)propyltrimethoxysilane, citric acid, folic acid, amine-terminated polyethylene glycol, and O-(2-Carboxyethyl)polyethylene glycol will be investigated in this chapter.

4.2 Materials and Methods

4.2.1 Materials

All of the chemicals used in the experiment were purchased and used as received except decaborane, which was further purified via sublimation before use. HERMLE Labortechnik centrifuge was used at 13,000 rpm for 10 minutes unless specified.

4.2.2 Synthesis of Boron Nanoparticles

Synthesis of boron nanoparticles was performed in a similar fashion as described in Chapter 3. Boron nanoparticles were generated via decomposition of decaborane at an elevated temperature. A 0.7 g sample of purified decaborane (5.73 mmol) was taken in a round-bottom flask that was connected to a quartz tube placed inside a horizontal tube furnace. The other end of the tube was connected to a gas bubbler. The round-bottom flask and the quartz tube were purged with dry argon gas for 30 minutes and the quartz tube was then heated to 700°C inside the tube furnace. Once the furnace reached the desired temperature, the round-bottom flask was heated to 105°C and the sublimed decaborane was passed through the quartz tube using a flow of dry argon gas with a rate of 0.22 L/min. The decaborane was decomposed over a period of six hours while passing through the quartz tube and the product deposited at the cooler end of the tube. The deposited dark powder was then collected and purified. The product was purified with multiple ethyl acetate wash or directly dried in *vacuo* overnight.

4.2.3 Synthesis of Boron/Silica Core/Shell Nanoparticles

A 109.3 mg sample of boron nanoparticles was dispersed in a solution containing 30 mL of ethanol and 3.5 mL of deionized (DI) water for 30 minutes. Then 0.75 mL of ammonium hydroxide (NH_4OH, 14.8 M) and 0.5 mL of tetraethoxysilane (TEOS) were added to the content in the flask. The solution was stirred at room temperature for 24 hours. The product was then collected via centrifugation and purified by washing with DI water and ethanol. Finally the product was dried in *vacuo* overnight.

A 21.3 mg sample of boron nanoparticles was dispersed in 23 mL of 95% ethanol for 30 minutes. A 1 mL of NH_4OH (14.8 M) and 0.1 mL of TEOS was added to the dispersed mixture in the flask. The mixture was stirred at room temperature for 20 minutes. The product was collected and washed twice with 95% ethanol. The final product was dried under *vacuo* overnight.

The above reaction was performed with a larger amount of starting materials to increase the mass of the final product.

A 43 mg sample of boron nanoparticles was dispersed in 46 mL of 95% ethanol for 30 minutes followed by an addition of 2 mL NH_4OH (14.8 M) and 0.2 mL of TEOS. The mixture was stirred at room temperature for 20 minutes. The product was collected and washed with 95% ethanol. The final product was dried under *vacuo* overnight.

4.2.4 Functionalization Of Boron/Silica Core/Shell Structure

4.2.4.1 Reaction with 3-(Amino Propyl) Triethoxy Silane

A 30 mg sample of boron/silica core/shell nanoparticles was dispersed in a 50 mL solution of 50:50 DI water and ethanol. The content in the flask was heated to 40°C and 0.7 mL of 3-(amino propyl) triethoxy silane (APTES) was added while stirring. The resulting mixture was refluxed for 21 hours. The product was then collected via centrifugation and purified by washing with DI water and ethanol. The final product was dried in *vacuo* overnight.

A 90 mg sample of boron/silica core/shell nanoparticles was dispersed in 12 mL of toluene for ten minutes. A 0.24 mL of APTES was added to the solution while stirring and the flask was transferred into an oil bath. The solution was heated to 92°C and refluxed for 20 hours. The product was then collected via centrifugation at 7,000 rpm for 30 minutes and purified by washing with ethanol. The final product was dried in *vacuo* overnight.

A 100.7 mg sample of boron/silica core/shell nanoparticles was dispersed in 50 mL tetrahydrofurane (THF) for ten minutes. Then 10.7 mL of APTES was added to the dispersed solution. The solution was stirred at room temperature for 24 hours. The product was then collected via centrifugation and purified by washing with THF and DI water. The final product was dried in *vacuo* overnight.

4.2.4.2 Reaction with 3-(2-Aminoethyleamino)Propyltrimethoxysilane

A 59.0 mg sample of boron/silica core/shell nanoparticles was added to a flask containing 6 mL of DI water. The flask was heated to 80°C, then 0.2 mL of acetic acid and 0.1 mL of 3-(2-

aminoethyleamino)propyltrimethoxysilane (AEAPS) were added to the flask. The solution in the flask was refluxed for 20 hours. The product was then collected via centrifugation and purified by washing with THF and DI water. The final product was dried in *vacuo* overnight.

4.2.4.3 Reaction with Citric Acid

A 53.0 mg sample of APTES functionalized boron/silica core/shell nanoparticles was dispersed in 3 mL of ethanol for 30 min. In a separate flask, 103 mg of citric acid, 50 mg of 1-ethyl-3-(3-dimethyl aminopropyl) carbodiimide hydrochloride (EDC) and 63 mg of N-hydroxy succinimide (NHS) were dispersed in 7 mL of ethanol for ten minutes. The solution containing the particles was transferred into the flask containing the citric acid mixture. The resulting mixture was stirred at room temperature for three days. The product was then collected via centrifugation and purified by washing with ethanol. The final product was dried in *vacuo* overnight.

4.2.4.4 Reaction with Folic Acid

A 64 mg sample of APTES functionalized boron/silica core/shell nanoparticles was dispersed in 2 mL of DMSO for 30 minutes. In a separate flask, 444 mg of folic acid, 158 mg of EDC and 115 mg of NHS were stirred for 20 hours in 20 mL of DMSO. The solution with the particles was transferred into the flask containing the folic acid solution. The resulting mixture was stirred at room temperature for three days. The product was then collected via centrifugation and purified by washing with DI water. The final product was dried in *vacuo* overnight.

4.2.4.5 Reaction with Amine-Terminated PEG

A 55.0 mg sample of citric acid-coated boron/silica core/shell nanoparticles was dispersed in DI water and the pH was adjusted to 9 by adding NaOH. A 102 mg sample of bis (3-aminopropyl)-terminated polyethylene glycol (PEG), 64 mg of NHS and 51 g of EDC was added to the basic solution of nanoparticles. The resulting mixture was then stirred for 48 hours and the final product was separated using a cellulose membrane dialysis tube, dried in *vacuo* and then characterized.

4.2.4.6 Synthesis of O-(2-Carboxyethyl) PEG

A 5 g sample of PEG ($PEG_{3400}(OH)_2$, 0.00147mole) in 25 mL of DI water containing 8 mL of concentrated sulfuric acid (96%) was added to an aqueous solution of 0.235 g of CrO_3 in 5 mL of DI water. The orange solution was stirred for eight hours at room temperature. The product was purified via the addition of 25 mL of DI water followed by extraction with 100 mL of dichloromethane (CH_2Cl_2) several times. The organic layers were combined and washed with 25 mL of DI water and 25 mL of saturated NaCl solution. The resulting organic layers were combined and dried with $MgSO_4$. Finally, the PEG-carboxylate was precipitated by the addition of 150 mL of ether. The final product was filtered and dried.

4.2.4.7 Reaction with O-(2-Carboxyethyl) PEG

A 52 mg sample of APTES functionalized boron/silica core/shell nanoparticles was dispersed in 4 mL of ethanol for 30 minutes. In a separate flask, 102 mg of O-(2-carboxyethyl) PEG (OH-PEG-COOH), 102 mg of EDC, and 122 mg of NHS were stirred for three hours in 10

mL of ethanol. The solution with the particles was added into the flask containing the O-(2-carboxyethyl) PEG solution. The resulting mixture was stirred at room temperature for two days. The product was then collected via centrifugation and purified by washing with ethanol. The final product was dried in *vacuo* overnight.

4.2.5 Biological Studies

Cytotoxicity of two compounds (namely, folic acid and amine-terminated PEG functionalized boron/silica core/shell compounds) were studied in a triple negative breast cancer cell line MDA-MB-231. The MDA-MB-231 culture media contains Dulbecco's modified Eagle medium (DMEM), 10% fetal bovine serum (FBS) and 1% penicillin-streptomycin. From the culture, $5x10^4$ cells/mL were transferred into 96-well plates and incubated at 37°C with 5% CO_2 atmosphere for 18-24 hours. The test compounds were dissolved in DMSO and a series of dilution was performed to vary the concentration starting from 1µg/mL to 0.008µg/mL. A one hundred microliters of these solutions was added to the plates and were incubated for 72 hours. Then 10µL of 3-(4,5-dimethylthiazol-2-yl)-2,5-diphenyltetrazolium bromide (5mg of MTT in 1mL of 1X PBS) was added to each well and incubated for four hours followed by the addition of 100µL of SDS-HCl (1g SDS in 10mL 0.01N HCl) into each well and further incubated for four hours. Finally the absorbance of each sample was measured using UV-Vis spectroscopy at 570 nm.

4.3 Results and Discussion

4.3.1 Synthesis of Boron Nanoparticles

The production of boron nanoparticles was done via pyrolysis. The process resulted in good yield of pure boron nanoparticles. A detailed discussion of the synthesis results of boron nanoparticles was done in Chapter 3 Section 3.3.1.

4.3.2 Synthesis of Boron/Silica Core/Shell Nanoparticles

The core/shell nanoparticles were formed using a seed-mediated synthesis. Previously synthesized boron nanoparticles were used as a seed for nucleation and growth of the silica shell. The silica shell was formed via base condensation with TEOS and ammonium hydroxide (Figure 4.2). The first procedure that used ethanol and water produced fused particles with amorphous structures (Figure 4.3).

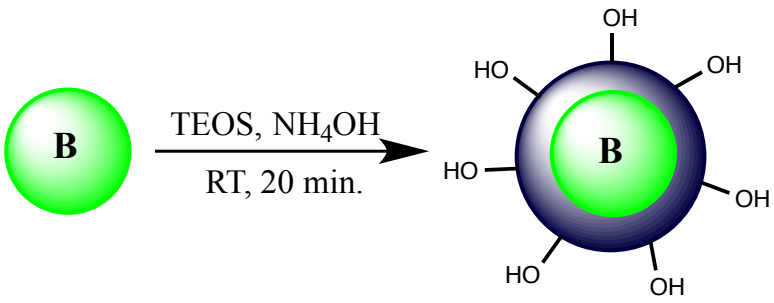

Figure 4.2: Synthesis of boron/silica core/shell nanoparticles.

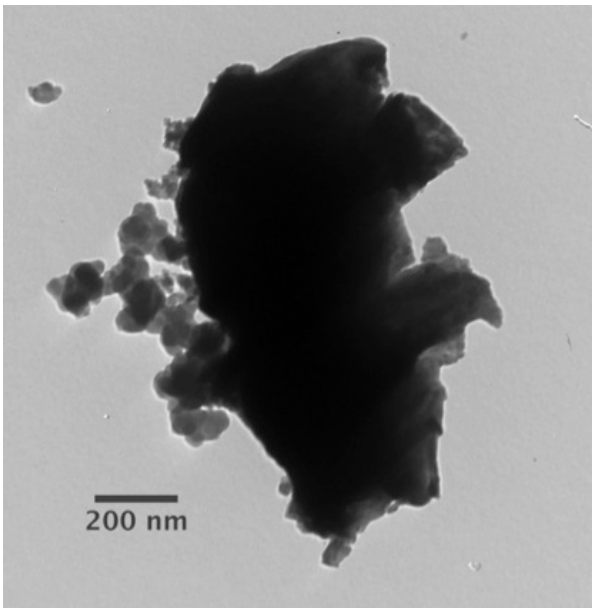

Figure 4.3: Transmission electron microscopy (TEM) image of boron/silica core/shell nanoparticles.

The second attempt was done using a published procedure by Hu and Sun.[23] Hu and Sun coated iron oxide nanoparticles with silica, and a similar procedure was implemented to coat boron instead of iron oxide. High-resolution TEM (HRTEM) showed the formation of two layers and an increase of the particles' diameter with an average silica shell diameter of 12 nm (Figure 4.4). The silica shell is known to carry terminal hydroxyl groups, which are attached to the silica through surface adsorption to cap the dangling silica bonds. In addition, the hydroxyl group was utilized for further surface functionalization of the nanoparticles.

Elemental analysis of the boron/silica core/shell nanoparticles was performed using energy-dispersive X-ray spectroscopy (EDX) and showed that the boron concentration is larger than 83% atomic weight, which corresponds to the core/shell structure mainly composed of boron with a small silica shell (Figure 4.5). The high purity of the sample can also be established since the product does not contain any other elements or impurities.

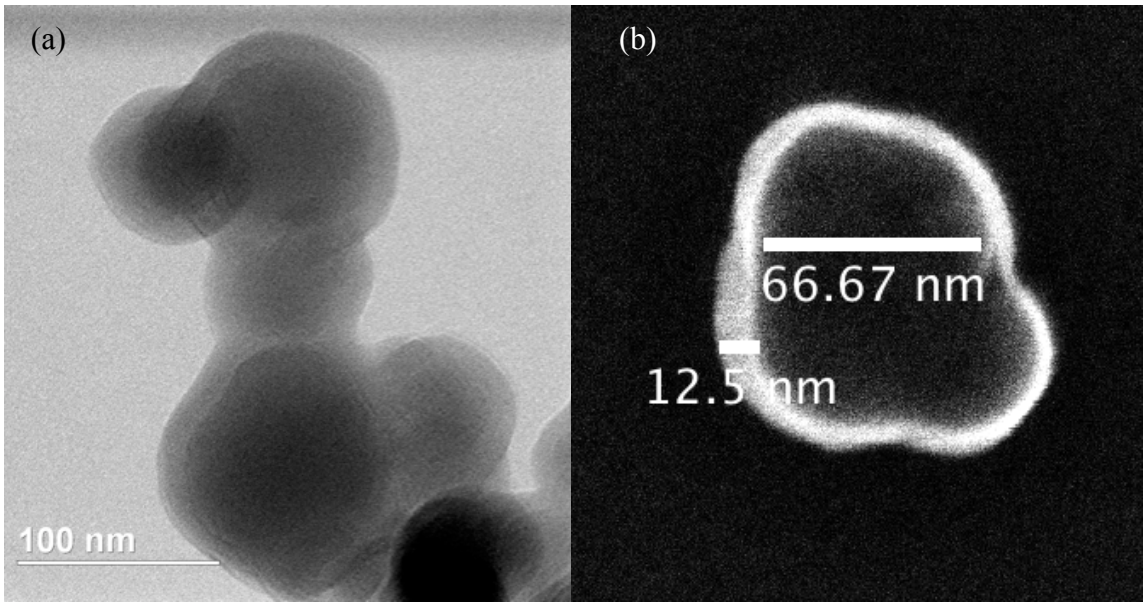

Figure 4.4: (a) HRTEM images of boron/silica core/shell nanoparticles and (b) HAADF image of single boron/silica core/shell nanoparticles.

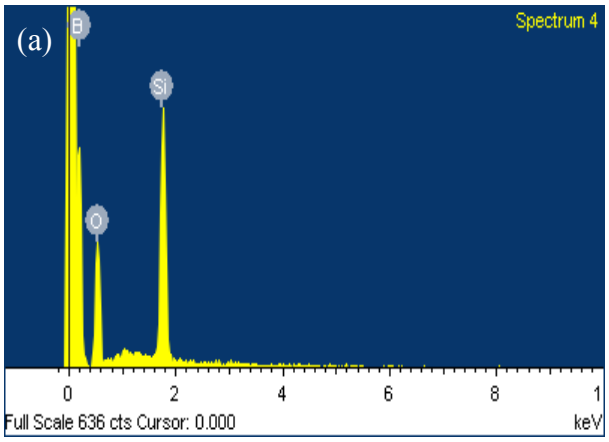

(b)

Element	Weight %	Atomic %
B	75.45	83.85
O	17.47	13.12
Si	7.08	3.03
Total	100	100

Figure 4.5: (a) EDX spectrum of boron/silica core/shell nanoparticles and (b) EDX data of boron/silica core/shell nanoparticles.

Furthermore, a scale-up synthesis was done following a similar procedure with twice as much starting materials. TEM images of the resulting product contained core/shell nanoparticles (Figure 4.6) and EDX analysis revealed the same chemical composition as shown above.

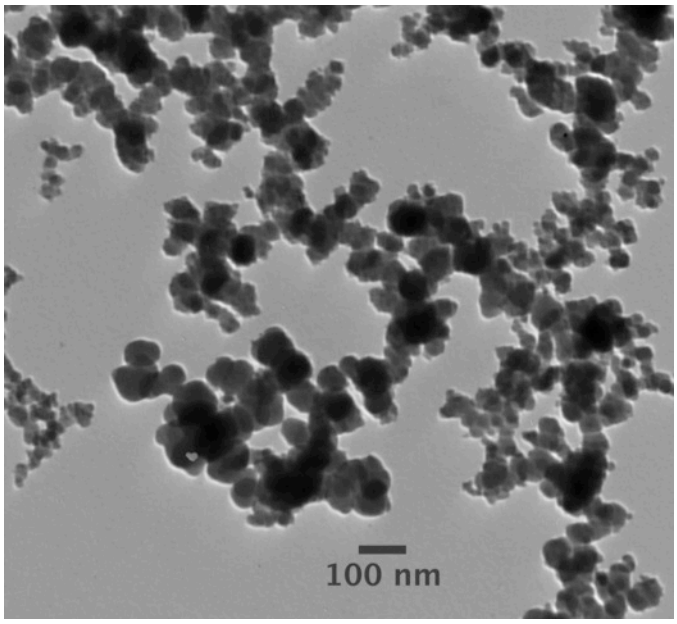

Figure 4.6: TEM image of boron/silica core/shell nanoparticles after scale-up synthesis.

4.3.3 Functionalization of Boron/Silica Core/Shell Structure

4.3.3.1 Reaction with APTES

Three different methods were used to modify the surface of boron/silica core/shell nanoparticles. Lehman et al. examined the functionalization of silica core/shell nanoparticles in toluene under reflux;[24] also, the same functionalization was done in THF at room temperature[25] and in 50:50 DI water and ethanol solution. These experiments produced APTES functionalized

boron/silica core/shell nanoparticles but the first and the third procedures required heat while the second method was done at room temperature (Figure 4.7). Since the second method consumes the least amount of energy, it was chosen as the standard procedure for subsequent functionalization of the nanoparticles with APTES. Figure 4.8 shows the TEM images of APTES functionalized boron/silica core/shell nanoparticles.

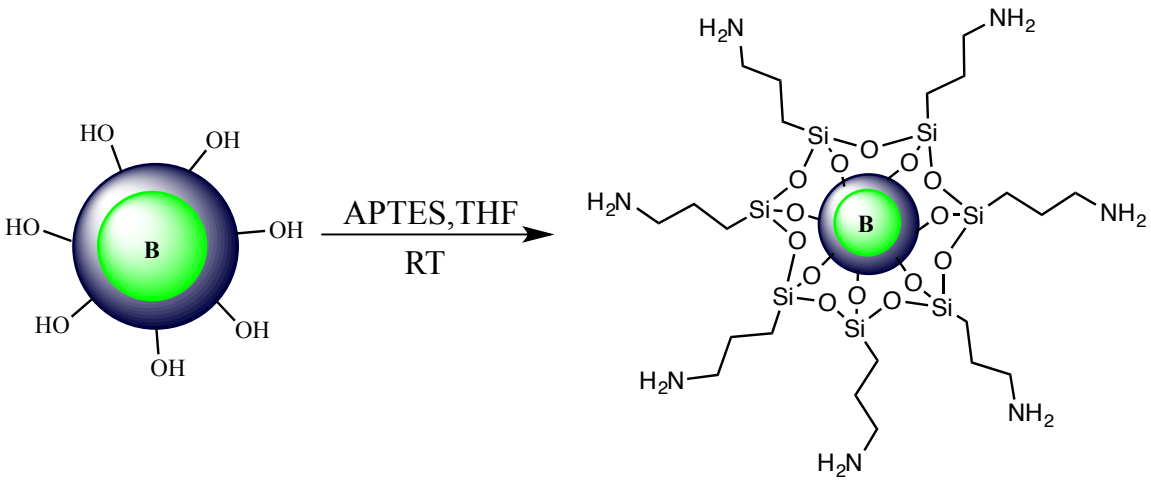

Figure 4.7: Synthesis of APTES functionalized boron/silica core/shell nanoparticles.

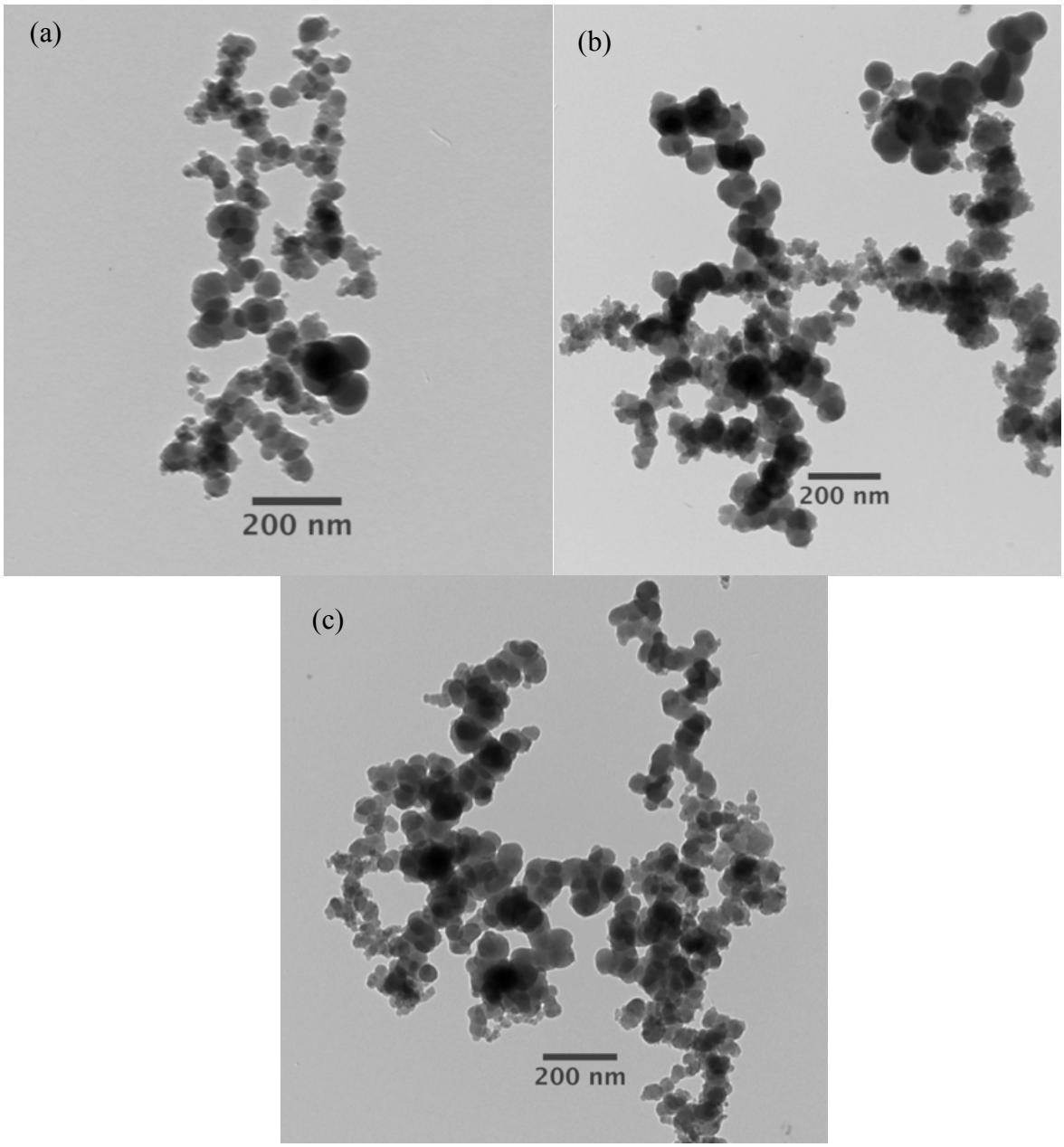

Figure 4.8: TEM images of boron/silica core/shell nanoparticle synthesis (a) in 50:50 DI water and ethanol, (b) in toluene, and (c) in tetrahydrofurane (THF).

Fourier-transform infrared spectroscopy (ATR-FTIR) spectrum of APTES functionalized boron/silica core/shell nanoparticles did not contain any additional peaks compared to bare boron/silica core/shell nanoparticles. The spectra peaks at 795 cm^{-1}, 940 cm^{-1}, 1060 cm^{-1}, and

3322 cm^{-1} correspond to symmetric Si-O vibration, asymmetric Si-OH vibration, asymmetric Si-O vibration, and OH group from water or moisture, respectively (Figure 4.9). Other researchers also observed the absence of additional peaks when silica nanoparticles are modified with APTES as well.[25,26]

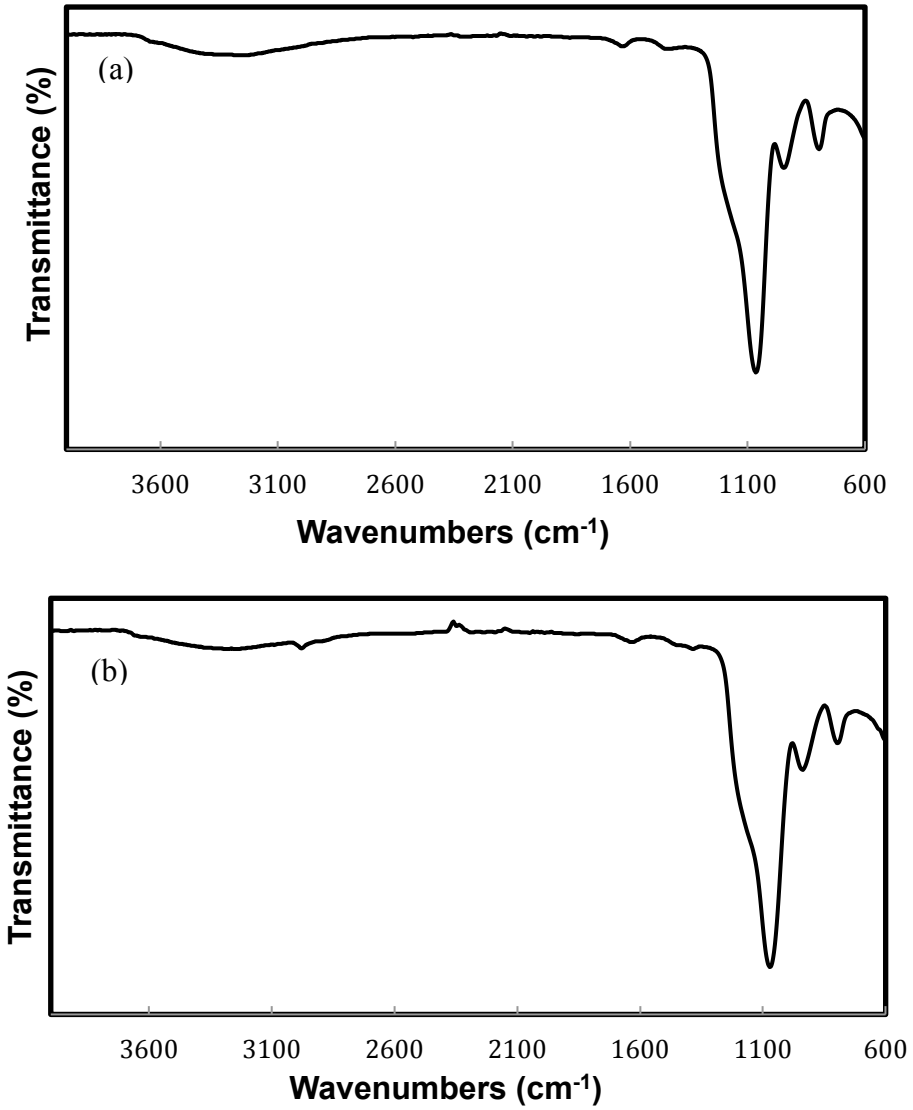

Figure 4.9: (a) ATR-FTIR spectrum of bare boron/silica core/shell nanoparticles and (b) ATR-FTIR spectrum of APTES functionalized boron/silica core/shell nanoparticles.

4.3.3.2 Reaction with AEAPS

Surface modification of silica nanoparticles with AEAPS has been studied for some time.[27] A similar procedure was used to functionalize the boron/silica core/shell nanoparticles. An acetic acid-induced simple condensation reaction between the surface OH of the core/shell nanoparticles and AEAPS to form a siloxane bond (-Si-O-Si-) resulted a modified nanoparticle. Based on the TEM images, the functionalized nanoparticles maintained a quasi-spherical morphology (Figure 4.10).

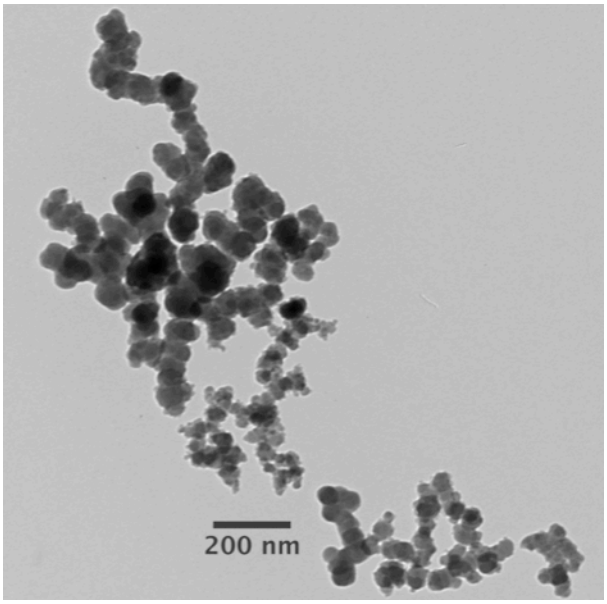

Figure 4.10: TEM images of AEAPS functionalized boron/silica core/shell nanoparticles.

ATR-FTIR spectrum of AEAPS-modified nanoparticles is identical to APTES functionalized boron/silica core/shell nanoparticles and bare boron/silica core/shell nanoparticles (Figure 4.11). In order to confirm the success of surface modification with AEAPS, scientists use the ninhydrin reaction, which causes ninhydrin to become a purple-colored product in the

presence of amine-containing compounds.[28] Figure 4.12 shows the ninhydrin reaction mechanism.

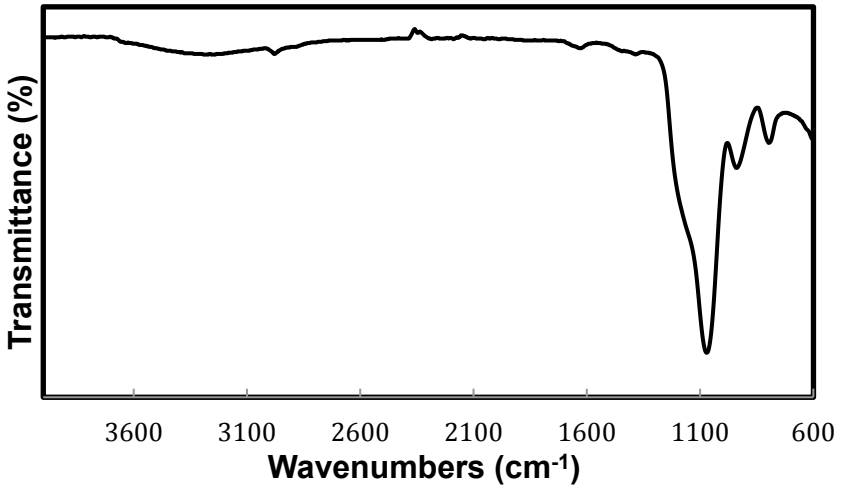

Figure 4.11: ATR-FTIR spectrum of AEAPS functionalized boron/silica core/shell nanoparticles.

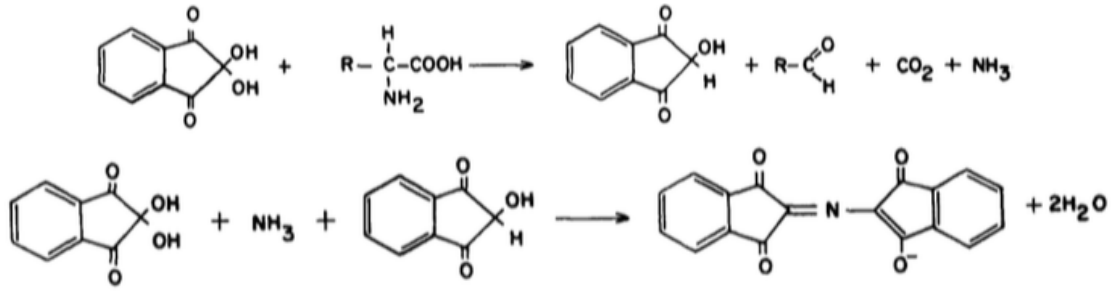

Figure 4.12: Mechanism of ninhydrin reaction. [28]

4.3.3.3 Reaction with Citric Acid

APTES-modified boron/silica core/shell nanoparticles were subjected to further reaction with citric acid to increase water solubility. EDC amidation reaction using NHS and EDC formed an amide bond between the amine of the APTES-modified nanoparticles and citric acid (Figure 4.13). The reaction requires activation of carbonyl groups of citric acid before the

addition of amine-containing nanoparticles. TEM images showed that the product only contains nanoparticles (Figure 4.14).

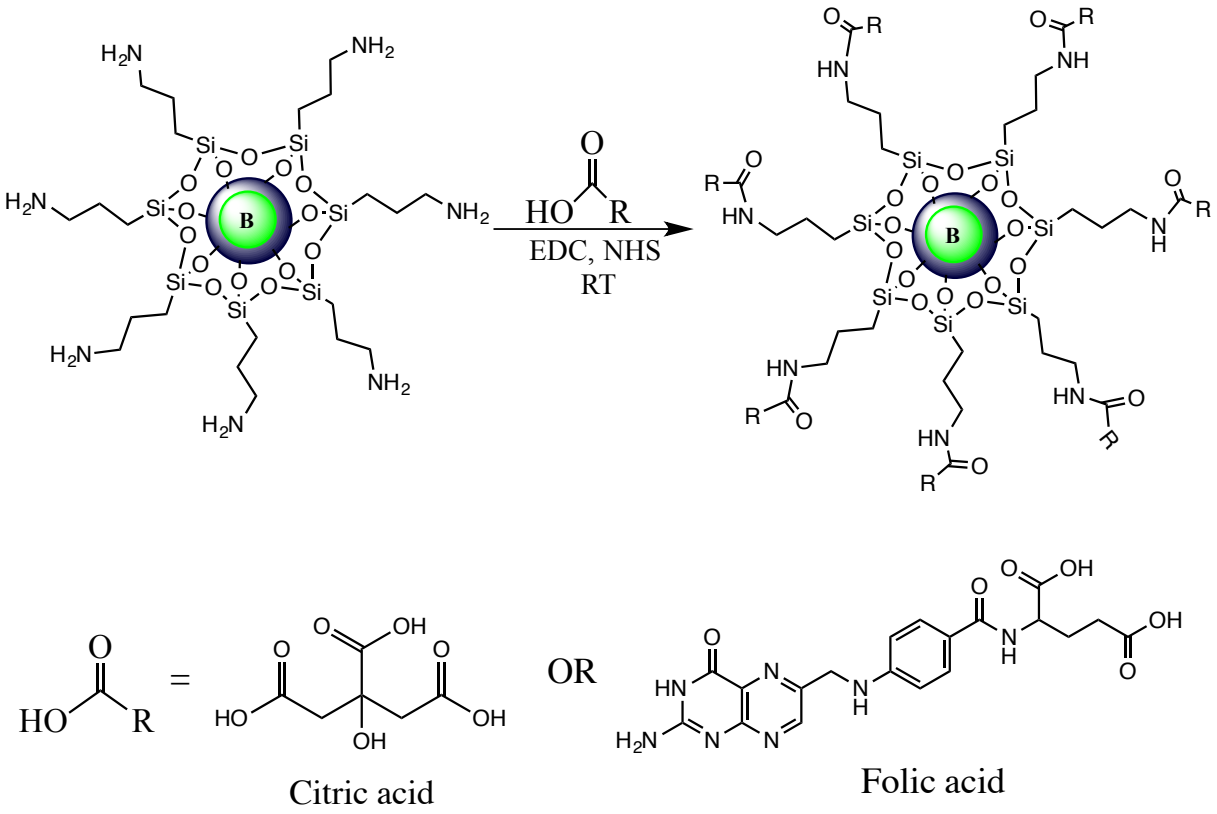

Figure 4.13: Synthesis of citric acid or folic acid functionalized boron/silica core/shell nanoparticles.

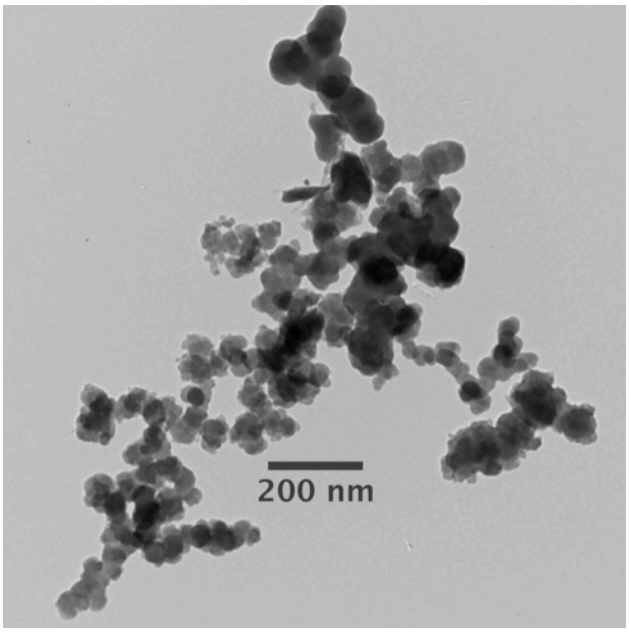

Figure 4.14: TEM image of citric acid functionalized boron/silica core/shell nanoparticles.

Citric acid functionalization of boron/silica core/shell nanoparticles was proven using ultraviolet-visible spectroscopy (UV-Vis) analysis. Pure citric acid has two signature UV-Vis absorption peaks at 206 nm and 263 nm. Similarly, the citric acid functionalized boron/silica core/shell nanoparticles contain both peaks. However, the nanoparticle spectrum has broad peaks caused by nanoparticles scattering. Furthermore, the original APTES functionalized boron/silica core/shell nanoparticles do not have the signature peaks of citric acid (Figure 4.15).

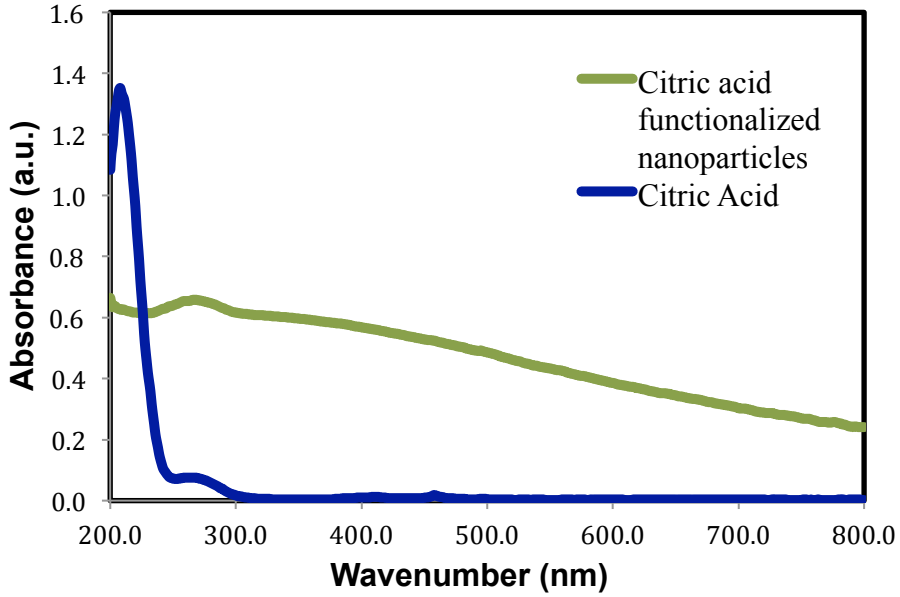

Figure 4.15: UV-Vis spectrum of citric acid functionalized boron/silica core/shell nanoparticles.

4.3.3.4 Reaction with Folic Acid

Receptor-targeting drug delivery has been widely used in recent years. This method exploits the fact that certain compounds such as folic acid can be recognized by receptor sites and then transported across the cell membrane into the cell.[29,30] Moreover, a high concentration of anti-cancer compounds can be accumulated in cancer cells using this approach. Therefore, folic acid was chosen as a boron delivery agent. The reaction mechanism is similar to citric acid functionalization mentioned above.[31] The EDC amidation reaction mechanism is shown below (Figure 4.16)

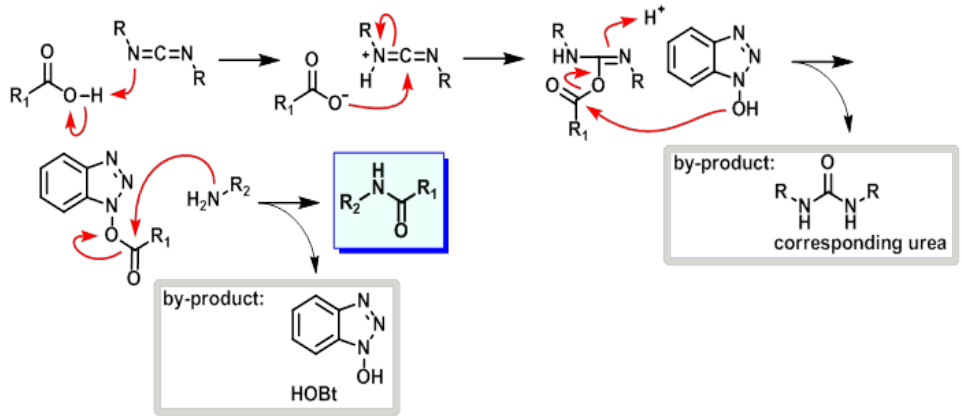

Figure 4.16: EDC-amidation reaction mechanism.

UV-Vis spectroscopy was used to establish the incorporation of folic acid on the surface of boron/silica core/shell nanoparticles. The spectrum displays three different peaks at 212 nm, 275 nm, and 345 nm for both free folic acid and folic acid functionalized boron/silica core/shell nanoparticles (Figure 4.17).

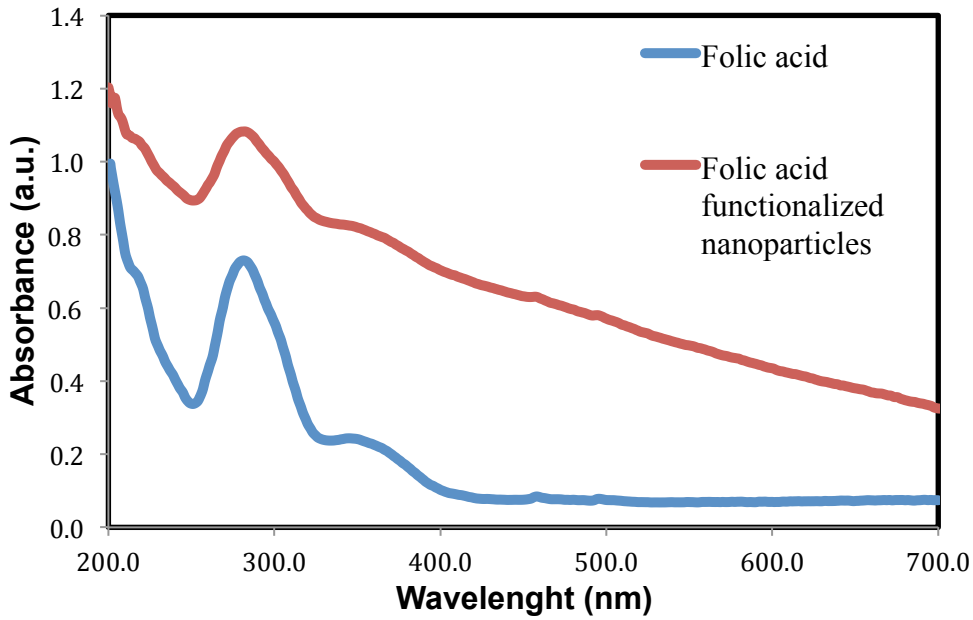

Figure 4.17: UV-Vis spectrum of folic acid functionalized boron/silica core/shell nanoparticles.

4.3.3.5 Reaction with Amine-Terminated PEG and O-(2-Carboxyethyl) PEG

PEG functionalized nanostructures lead to decreased toxicity and the elimination of the nanostructures from the cell. In addition, pegylated nanoparticles can stay in the blood for an extended period of time and are less likely to enter the reticuloendothelial system or macrophage system, particularly the liver and spleen. As a result, the probability of nanoparticles being captured by tumor cells increases. The boron/silica core/shell nanoparticles were modified using two PEG compounds. Both bis (3-aminopropyl)-terminated PEG and O-(2-Carboxyethyl) PEG were attached to nanoparticles via an amide bond with citric acid and APTES, respectively (Figure 4.18). All of the functionalized boron/silica core/shell nanoparticles maintained a quasi-spherical morphology (Figure 4.19).

The ATR-FTIR spectrum of amine-terminated PEG functionalized boron/silica core/shell nanoparticles displayed peaks at 960 cm^{-1}, 1059 cm^{-1}, and 1634 cm^{-1} which corresponded to Si-OH, Si-O of the silica shell, and carboxyl groups of citric acid, respectively (Figure 4.20). On the other hand, peaks at 2881 cm^{-1} and 3292 cm^{-1} were due to aliphatic C-H bonds and amine groups, respectively. In contrast, the O-(2-Carboxyethyl) PEG functionalized boron/silica core/shell nanoparticles did not show any signature peaks coming from O-(2-Carboxyethyl) PEG when characterized using ATR-FTIR and UV-Vis spectroscopy. The absence of peaks indicates the functionalization process did not produce the intended product.

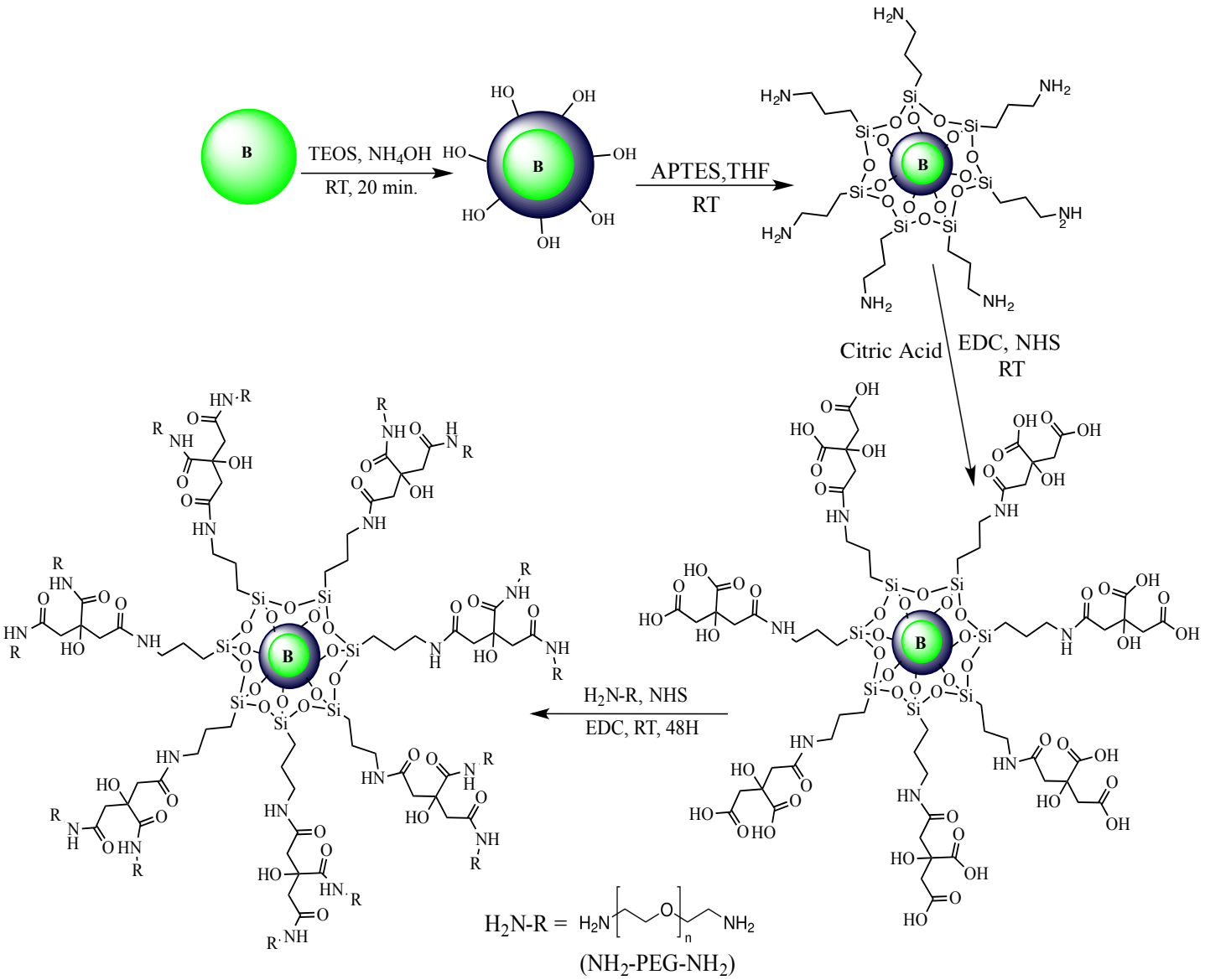

Figure 4.18: Synthesis of amine-terminated PEG functionalized boron/silica core/shell nanoparticles.

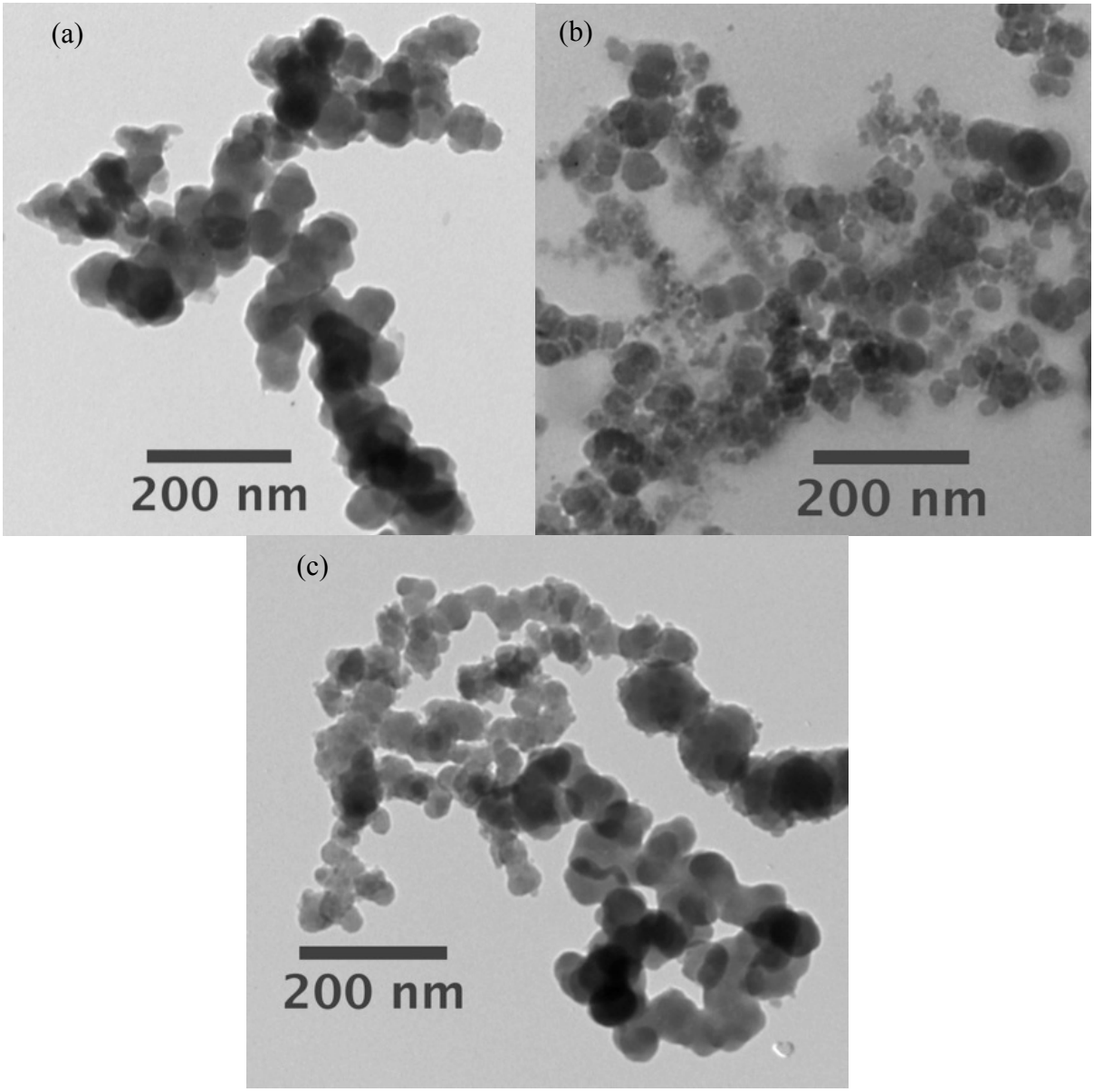

Figure 4.19: TEM images of (a) folic acid functionalized boron/silica core/shell nanoparticles, (b) amine-terminated PEG functionalized boron/silica core/shell nanoparticles, and (c) O-(2-Carboxyethyl) PEG functionalized boron/silica core/shell nanoparticles.

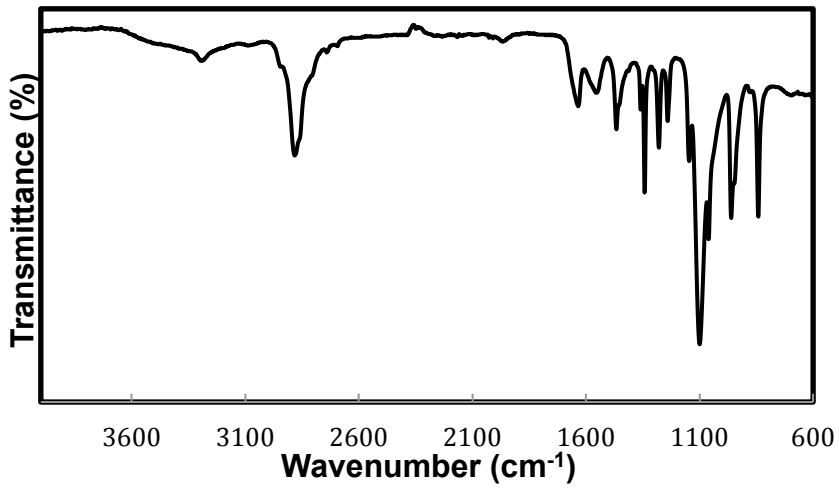

Figure 4.20: ATR-FTIR spectrum of amine-terminated PEG functionalized boron/silica core/shell nanoparticles.

4.3.3.6 Synthesis of O-(2-Carboxyethyl) PEG

O-(2-Carboxyethyl) PEG was synthesized using PEG with an average molecular weight of 3,400.[32] The procedure utilized chromium trioxide (CrO_3) to convert one of the terminal hydroxyl groups to a carboxylic group (Figure 4.21). The amount of chromium trioxide was only limited to 1.1 electron equivalents to ease the removal of Cr (IV) from the polymer. If the Cr (IV) is not completely eliminated the polymer will have a green-blue color.

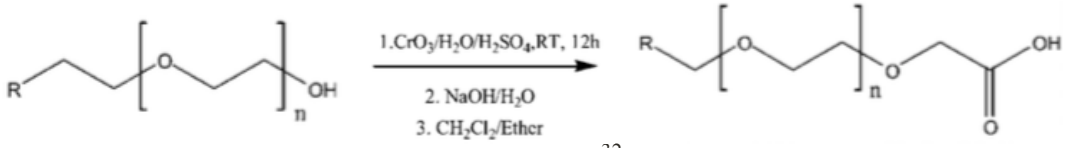

Figure 4.21: Synthesis of O-(2-Carboxyethyl) PEG.[32]

Proton nuclear magnetic resonance (H-NMR) of the product confirmed the formation of COOH with peaks at 3.6 ppm and 4.07 ppm corresponding to methylene protons and CH_2COOH, respectively (Figure 4.22). The peak at 4.6 ppm came from the solvent (D_2O) used

to dissolve the compound, and the intensity of the CH_2COOH peak was smaller than that of methylene. This is because there was only one unit of CH_2COOH compared to a large number of repeating methylene units.

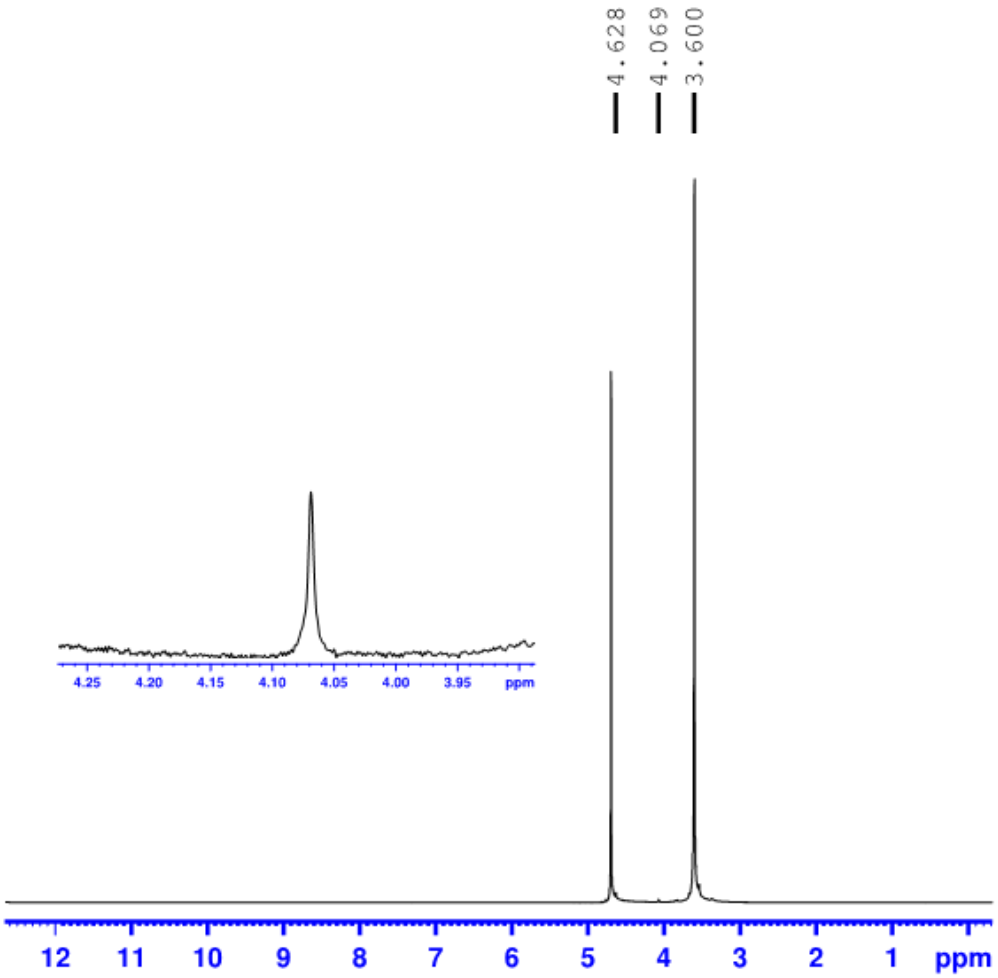

Figure 4.22: ^{1}H NMR spectra of O-(2-Carboxyethyl) PEG.

4.3.4 Biological Studies

Cytotoxicity of the compounds was conducted using MTT assay. The assay uses NAD(P)H-oxidoreductase enzymes of living cells to reduce 3-(4,5-dimethylthiazol-2-yl)-2,5-diphenyltetrazolium bromide to a purple solid called formazan. The precipitate formazan is dissolved in surfactant sodium dodecyl sulfate (SDS) in dilute hydrochloric acid and the absorbance of the solution is measured at 570 nm. The intensity of the absorption peak reflects the number of living cells. In other words, more living cells in the culture leads to a higher rate of MTT reduction to formazan and higher absorption intensity. The study was done in triplet to establish the consistency and reproducibility of the method. The percent of cell survival is calculated using equation 4.1:

$$\% \text{ Survival} = \left({}^{A_t}/_{A_c}\right) \times 100 \qquad \text{(Equation 4.1)}$$

where A_t is absorbance of test compound, A_c is absorbance of control and the growth media was used as a control. Subsequently, IC_{50} value of the compound was determined by plotting log concentration vs. % Survival in Graphpad Prism software. Figure 4.23 shows that the entire cell line survived in the concentration range (0.0081μg/mL-1μg/mL); the amine-terminated PEG functionalized boron/silica core/shell nanoparticles were tested implying that the IC_{50} value is greater than 1μg/mL. The IC_{50} value for folic acid and O-(2-Carboxyethyl) PEG functionalized boron/silica core/shell nanoparticles are also greater than 1μg/mL.

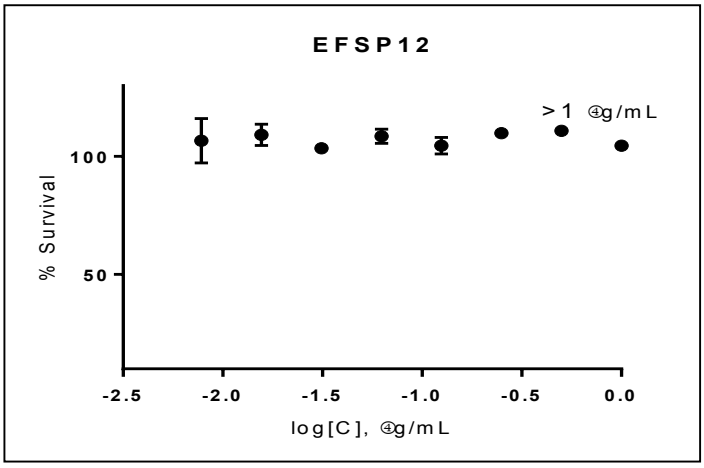

Figure 4.23: Plot of logC vs. %Survival of amine-terminated PEG functionalized boron/silica core/shell nanoparticles.

4.4 Summary and Conclusion

The synthesis of silica in the presence of boron nanoparticles formed core/shell nanoparticles. HRTEM of the core/shell nanoparticles showed the two layers distinctively. Once the boron/silica core/shell nanoparticles were prepared, the surface of silica was functionalized with APTES, AEAPS, citric acid, folic acid, and amine-terminated PEG. Three procedures using different solvents were tested to functionalize the core/shell structure with APTES. Although all of them accomplished the intended product, only one was selected because of its minimum energy consumption. Then APTES-functionalized nanoparticles were used for amidation reaction with citric acid and folic acid. Furthermore, citric acid-conjugated nanoparticles underwent another amidation reaction to attach amine-terminated PEG. The formation of the intended product after each step was established using UV-Vis, ATR-FTIR, or NMR. Cytotoxicity of folic acid and amine-terminated PEG functionalized boron/silica core/shell

nanoparticles was determined using a triple negative breast cancer cell line MDA-MB-231. In addition, the IC_{50} value of the compounds was greater than 1μg/mL.

References

1. Vallet-Regí, M. Mesoporous Silica Nanoparticles: Their Projection In Nanomedicine. *ISRN Materials Science,* **2012**, 1-20.

2. Wen, J.; Wilkes, G. L., Organic/inorganic hybrid network materials by the sol-gel approach. *Chemistry of Materials* **1996,** *8*, 1667-1681.

3. Rahman, I.; Padavettan, V.; Synthesis Of Silica Nanoparticles By Sol-Gel: Size-Dependent Properties, Surface Modification, And Applications In Silica-Polymer Nanocomposites—A Review. *J. Nanomater*., **2012**, 1-15.

4. Yao, X.; Zhou, D.; Yeh, H. Macro/Microscopic Fracture Characterizations Of Sio2/Epoxy Nanocomposites. *Aerospace Science and Technology,* **2008**, *12*, 223-230.

5. Liu, W.; Zhu, B.; Zhang, J.; Xu, Y. Preparation And Dielectric Properties Of Polyimide/Silica Nanocomposite Films Prepared From Sol–Gel And Blending Process. *Polym. Adv. Technol.,* **2007**, *18*, 522-528.

6. Zhang, H.; Zhang, Z.; Friedrich, K.; Eger, C. Property Improvements Of In Situ Epoxy Nanocomposites With Reduced Interparticle Distance At High Nanosilica Content. *Acta Materialia,* **2006**, *54*, 1833-1842.

7. Bondioli, F.; Cannillo, V.; Fabbri, E.; Messori, M. Epoxy-Silica Nanocomposites: Preparation, Experimental Characterization, And Modeling. *Journal of Applied Polymer Science* 2005, *97*, 2382-2386.

8. Vega-Baudrit, J.; Navarro-Bañón, V.; Vázquez, P.; Martín-Martínez, J. Addition Of Nanosilicas With Different Silanol Content To Thermoplastic Polyurethane Adhesives. *International Journal of Adhesion and Adhesives* **2006**, *26*, 378-387.

9. Wan, J.; Meng, X.; Liu, E.; Chen, K. Incorporation Of Magnetite Nanoparticle Clusters In Fluorescent Silica Nanoparticles For High-Performance Brain Tumor Delineation. *Nanotechnology,* **2010**, *21*, 235104.

10. Yang, L.; Chen, Z. Direct Evaluation Of Ligand-Receptor Interaction By A Novel Imaging Model Based On Fluorescent Silica Nanoparticle As Ligand Probe And Molecular Imprinting Polymer As Artificial Receptor. *Anal. Lett.* **2011**, *44*, 687-697.

11. Wang, X.; Ramström, O.; Yan, M. Dye-Doped Silica Nanoparticles As Efficient Labels For Glycans. *Chem. Commun.,* **2011**, *47*, 4261.

12. Qin, D.; He, X.; Wang, K.; Tan, W. Using Fluorescent Nanoparticles And SYBR Green I Based Two-Color Flow Cytometry To Determine Mycobacterium Tuberculosis Avoiding False Positives. *Biosens. Bioelectron.,* **2008**, *24*, 626-631.

13. Wang, Z.; Miu, T.; Xu, H.; Duan, N.; Ding, X.; Li, S. Sensitive Immunoassay Of Listeria Monocytogenes With Highly Fluorescent Bioconjugated Silica Nanoparticles Probe. *J. Microbiol. Methods,* **2010**, *83*, 179-184.

14. Wang, L.; Zhao, W.; Tan, W. Bioconjugated Silica Nanoparticles: Development And Applications. *Nano Res.,* **2008**, 1, 99-115.

15. Argyo, C.; Weiss, V.; Bräuchle, C.; Bein, T. Multifunctional Mesoporous Silica Nanoparticles As A Universal Platform For Drug Delivery. *Chem. Mater.* **2014**, *26*, 435-451.

16. Fan, W.; Shen, B.; Bu, W.; Zheng, X.; He, Q.; Cui, Z.; Zhao, K.; Zhang, S.; Shi, J. Design Of An Intelligent Sub-50 Nm Nuclear-Targeting Nanotheranostic System For Imaging Guided Intranuclear Radiosensitization. *Chem. Sci.,* **2015**, *6*, 1747-1753.

17. Lu, F.; Wu, S.; Hung, Y.; Mou, C. Size Effect On Cell Uptake In Well-Suspended, Uniform Mesoporous Silica Nanoparticles. *Small,* **2009,** *5*, 1408-1413.

18. He, Q.; Zhang, Z.; Gao, F.; Li, Y.; Shi, J. In Vivo Biodistribution And Urinary Excretion Of Mesoporous Silica Nanoparticles: Effects Of Particle Size And Pegylation. *Small,* **2011**, *7*, 271-280.

19. He, Q.; Zhang, Z.; Gao, Y.; Shi, J.; Li, Y. Intracellular Localization And Cytotoxicity Of Spherical Mesoporous Silica Nano- And Microparticles. *Small*, **2009**, *5*, 2722-2729.

20. Cauda, V.; Argyo, C.; Bein, T. Impact Of Different Pegylation Patterns On The Long-Term Bio-Stability Of Colloidal Mesoporous Silica Nanoparticles. *J. Mater. Chem.*, **2010**, *20*, 8693-8699.

21. Tao, Z.; Toms, B.; Goodisman, J.; Asefa, T. Mesoporosity And Functional Group Dependent Endocytosis And Cytotoxicity Of Silica Nanomaterials. *Chem. Res. Toxicol.* **2009**, *22*, 1869-1880.

22. He, Q.; Zhang, J.; Shi, J.; Zhu, Z.; Zhang, L.; Bu, W.; Guo, L.; Chen, Y. The Effect Of Pegylation Of Mesoporous Silica Nanoparticles On Nonspecific Binding Of Serum Proteins And Cellular Responses. *Biomaterials,* **2010**, *31*, 1085-1092.

23. Hu, Y.; Sun, Y. A Generic Approach For The Synthesis Of Dimer Nanoclusters And Asymmetric Nanoassemblies. *J. Am. Chem. Soc.* **2013**, *135*, 2213-2221.

24. Lehman, S.; Tataurova, Y.; Mueller, P.; Mariappan, S.; Larsen, S. Ligand Characterization Of Covalently Functionalized Mesoporous Silica Nanoparticles: An NMR Toolbox Approach. *J. Phys. Chem. C,* **2014**, *118*, 29943-29951.

25. Ataee-Esfahani, H.; Nemoto, Y.; Wang, L.; Yamauchi, Y. Rational Synthesis Of Pt Spheres With Hollow Interior And Nanosponge Shell Using Silica Particles As Template. *Chem. Commun.,* **2011**, *47*, 3885-3887.

26. Chandran, S. P.; Hotha, S.; Prasad, B. L. V.; Tunable Surface Modification of Silica nanoparticles Through 'Click' Chemistry. Curr. Sci., **2008**, 95, 1327-1333.

27. Kneuer, C.; Sameti, M.; Bakowsky, U.; Schiestel, T.; Schirra, H.; Schmidt, H.; Lehr, C. A Nonviral DNA Delivery System Based On Surface Modified Silica-Nanoparticles Can Efficiently Transfect Cells In Vitro. *Bioconjugate Chem.,* **2000**, *11*, 926-932.

28. Bottom, C.; Hanna, S.; Siehr, D. Mechanism Of The Ninhydrin Reaction. *Biochemical Education,* **1978**, *6*, 4-5.

29. Roger, E.; Kalscheuer, S.; Kirtane, A.; Guru, B.; Grill, A.; Whittum-Hudson, J.; Panyam, J. Folic Acid Functionalized Nanoparticles For Enhanced Oral Drug Delivery. *Mol. Pharmaceutics,* **2012**, *9*, 2103-2110.

30. Venkatasubbu, G.; Ramasamy, S.; Avadhani, G.; Ramakrishnan, V.; Kumar, J. Surface Modification And Paclitaxel Drug Delivery Of Folic Acid Modified Polyethylene Glycol Functionalized Hydroxyapatite Nanoparticles. *Powder Technology,* **2013**, *235*, 437-442.

31. Tran, T.; Nguyen, C.; Kim, D.; Lee, Y.; Huh, K. Microfluidic Approach For Highly Efficient Synthesis Of Heparin-Based Bioconjugates For Drug Delivery. *Lab Chip,* **2012**, *12*, 589-594.

32. Fishman, A.; Acton, A.; Lee‐Ruff, E. A Simple Preparation Of PEG‐Carboxylates By Direct Oxidation. *Synth. Commun.,* **2004**, *34*, 2309-2312.

CHAPTER 5

SYNTHESIS AND CHARACTERIZATION OF BORON NANORODS

5.1 Introduction

Boron nanorods are one-dimensional nanomaterials with a wide variety of applications including electronics and medicine. Currently there have been different approaches using both bottom-up and top-down synthesis methods to fabricate boron nanorods. Bottom-up methods include chemical vapor deposition (CVD) of diborane between 700-950°C done by Yang et al.[1] On the other hand, top-down synthesis via ball milling was performed by Zhu and Kisi.[2] Zhu and Kisi ball milled boron powder followed by annealing the powder at 1200°C. This synthetic approach produced boron nanorods as well as amorphous boron nanostructures. In addition, elemental analysis of the product reveals contamination with iron. Overall, both CVD and ball milling approaches have disadvantages such as contamination, structural defects, toxic starting materials, requirement of high temperature, and prolonged reaction period. Therefore, there is a need to develop a synthetic approach that will avoid the drawbacks listed above.

In 2010, Chakrabarti et al.[3] published a paper describing a new methodology to prepare boron nanorods. This approach used lithium to reduce boron oxide into boron nanorods. The synthesis was performed at significantly lower temperatures compared to 700-950°C used by Yang et al. and 1200°C used by Zhu and Kisi. In addition, a non-toxic and widely available starting material, which costs between $4-$8 per kilogram, was used. Therefore, a new greener

and cost-effective synthetic approach was introduced. However, this procedure has a major flaw, which is the formation of boron nanoparticles alongside boron nanorods. This problem leads to my project that is to overcome or decrease the formation of side products, specifically, the presence of boron nanoparticles. We will discuss multiple optimization techniques and approaches taken to resolve this issue.

5.2 Materials and Methods

5.2.1 Materials

All of the chemicals used in the experiment were purchased and used as received except boron oxide, which was dried overnight at 110°C before use. A Fisher Scientific FB120 sonicator with a frequency of 20 kHZ and an innovative technology glovebox was used.

5.2.2 Synthesis of Boron Nanorods

Boron nanorods were synthesized following a published procedure.[3] In a typical preparation, a 0.3 g (43.1 mmol) sample of boron oxide (B_2O_3) was placed in a 10 mL nickel crucible which is inside a thermowell. Then the crucible was heated to 200°C. Once the lithium melts, 0.5 g of boron oxide (7.18 mmol) was added in small increments at a time. During the addition of boron oxide the content in the crucible was mixed via sonication. After all of the boron oxide was added, the temperature was increased to 250°C and the crucible was left under sonication for two hours. After the reaction is complete the crucible was taken out of the thermowell and cooled to room temperature. All of the above steps were performed inside an argon glovebox that is maintained with less than 10 ppm of oxygen.

Finally the nickel crucible was taken out of the glovebox and purified. The purification process starts with an addition of methanol, which helps remove the product out of the crucible. Following the removal of methanol the product was subjected to multiple washes with hot deionized (DI) water, 0.1 M potassium hydroxide (KOH), 0.1 M hydrochloric acid (HCl), and DI water. The final product was dried in *vacuo* overnight and then characterized.

The synthetic procedure was altered to scale up the production of boron nanorods before any optimization was performed. Therefore, the amount of starting materials was increased in fourfold. The reaction was performed following the same procedure mentioned above in a 25 mL nickel crucible. Furthermore, synthesis of boron nanorods using a different metal, namely sodium, was attempted. A 0.5 g sample of sodium was melted at 100°C and 0.26 g of B_2O_3 was added while the content was sonicated at 50% amplitude. After the entire B_2O_3 was added, the temperature was increased to 150°C and the reaction was sonicated for another two hours. The product was purified with methanol and hot water washes.

5.2.3 Optimization of Reaction Conditions

5.2.3.1 Sonication

The first step taken to optimize the reaction procedure was to determine the importance and effect of sonication in the process. Therefore, a reaction was performed without sonication of the content in the crucible. A 1.42 g sample of lithium (204.6 mmol) was melted at 200°C. Then 2.0 g of boron oxide (28.7 mmol) was added. Once the addition of boron oxide was done the reaction temperature was increased to 250°C and the crucible was covered for two hours. The

product was collected and purified. Finally the product was dried in *vacuo* overnight and then characterized.

Next, different sonication amplitudes were investigated. Table 5.1 has a complete list of reaction times, temperatures, and sonication amplitudes. Each of the reactions in the table was performed and purified using the scale-up synthesis procedure.

Table 5.1

Reaction Conditions for Sonication Amplitude Optimization.

Sample	Sonication Amplitude	Reaction Temp. (°C)	Duration (hour)
1	20%	260	2
2	40%	260	2
3	60%	260	2
4	80%	260	2

5.2.3.2 Temperature

The original synthetic protocol dictates that the lithium metal melts at 200°C and then the temperature was increased to 250°C for the remaining two hours after all of the boron oxide was added. We varied the reaction temperature in an attempt to form a product without any boron nanoparticles. A list of different temperatures that were examined is shown in Table 5.2.

Table 5.2

Reaction Conditions for Temperature Optimization.

Sample	Reaction Temp. (°C)	Sonication Amplitude	Duration (hour)
1	180	60%	2
2	210	60%	2
3	230	60%	2
4	260	60%	2
5	280	60%	2
6	300	60%	2

5.2.3.3 Reaction Time

The final optimization was done with reaction time. The initial reaction duration of two hours was varied starting from 30 minutes and extended up to four hours. The first reaction was left to run for half an hour then the reaction time was increased in 30-minute or one-hour increments for the consecutive trials (Table 5.3).

Table 5.3

Reaction Conditions for Time Optimization.

Sample	Duration (hour)	Sonication Amplitude	Reaction Temp. (°C)
1	0.5	60%	180
2	1	60%	210
3	1.5	60%	230
4	2	60%	260
5	3	60%	280
6	4	60%	300

5.2.4 Functionalization of boron nanorods

Several attempts were made to functionalize the boron nanorods that were prepared using the optimal reaction conditions. The functionalization was done using bis (3-aminopropyl)-terminated polyethylene glycol, folic acid, and hydrogen peroxide (H_2O_2).

5.2.4.2 Reaction with Bis (3-Aminopropyl)-Terminated Polyethylene Glycol

A 0.5 g sample of bis (3-aminopropyl)-terminated polyethylene glycol (PEG) in a round-bottom flask was set under a condenser and the system was purged with argon followed by increasing the temperature to 50°C. Once the polymer melted completely, 0.02 g of previously prepared boron nanorods were added into the flask and the flask was stirred for three days. When the reaction was complete the contents in the flask were cooled to room temperature and

purified. The sample was purified by the addition of DI water followed by centrifugation at 3,000 rpm for 30 minutes. Then the supernatant was collected and the residue was washed repeatedly. Finally, all the supernatant from each wash was combined and the DI water was removed via a rotary evaporator. The final product was dried in *vacuo* overnight and then characterized.

5.2.4.2 Reaction with Folic Acid

A reaction with folic acid was performed with 0.021 g of boron nanorods and 0.197 g of folic acid. A round-bottom flask containing the boron nanorods sample was dispersed in 50 mL of DI water for 45 minutes followed by the addition of folic acid. The solution was stirred at room temperature for three days. The product was collected, isolated, and characterized.

5.2.4.3 Reaction with Hydrogen Peroxide

A 0.102 g sample of boron nanorods were dispersed in 50 mL of hydrogen peroxide (H_2O_2) for 30 minutes using a water bath sonicator. Then the flask was transferred to an oil bath heated at 110°C and the contents were stirred for three hours. Once the reaction was complete the solution was centrifuged in DI water three times and the decant was collected. Then the water was removed using a rotary evaporator. The final product was dried in *vacuo* overnight and then characterized.

A second trial with hydrogen peroxide was performed with a small volume of H_2O_2. A 0.099 g sample of boron nanorods was dispersed for 20 minutes in a 100 mL solution containing 90 mL of DI water and 10 mL H_2O_2. Then the solution was refluxed at 100°C with stirring

overnight. The resulting mixture was washed with water and centrifuged multiple times at 3,000 rpm for ten minutes. The final product was dried in *vacuo* overnight and then characterized.

5.3 Results and Discussion

5.3.1 Synthesis of Boron Nanorods

The synthetic procedure utilized the reduction of boron oxide with lithium to form boron nanorods shown in Figure 5.1.[3] The reaction was performed under an inert atmosphere to prevent oxidation of the lithium metal.

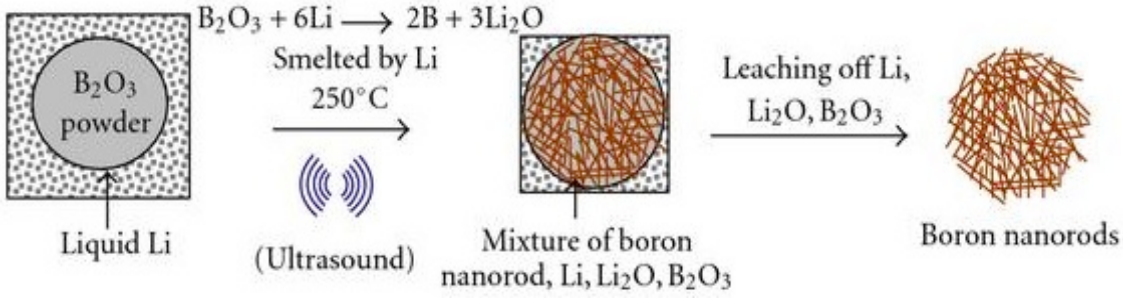

Figure 5.1: Reaction scheme for the synthesis of boron nanorods.

Based on the balanced chemical equation, six moles of lithium were required to reduce one mole of B_2O_3, but during the scale-up production of boron nanorods an excess of lithium was used to guarantee the total conversion of B_2O_3 to boron. Lithium is the ideal reducing agent with a reducing potential of -3.05 V and a low melting point. In addition, the intercalating property of lithium ensures the formation of rod-like nanostructures.

After the reaction is complete the resulting mixture contains boron nanorods, unreacted lithium, unreacted B_2O_3, lithium tetraboride and lithium diborides. These byproducts as well as

unreacted starting materials need to be removed in order to recover pure boron nanorods. Therefore, a series of washes were performed. The first wash was done using methanol, which reacts with lithium to form a salt called lithium methoxide and this salt solution was easily removed from the rest of the mixture. The second wash uses hot water to remove unreacted B_2O_3 since B_2O_3 is soluble in hot water. The third wash removed lithium tetraboride using 0.1 M KOH followed by the elimination of lithium diborides using 0.1 M HCl. Finally the product was washed with DI water to change the pH of the solution to natural.

The morphology of the product was determined using transmission electron microscopy (TEM). The result shows boron nanorods with a diameter between 10-500 nm and a length up to 10 μm (Figure 5.2). Scanning electron microscopy (SEM) also supports the observation of the formation of nanorods along with some amorphous structures (Figure 5.3).

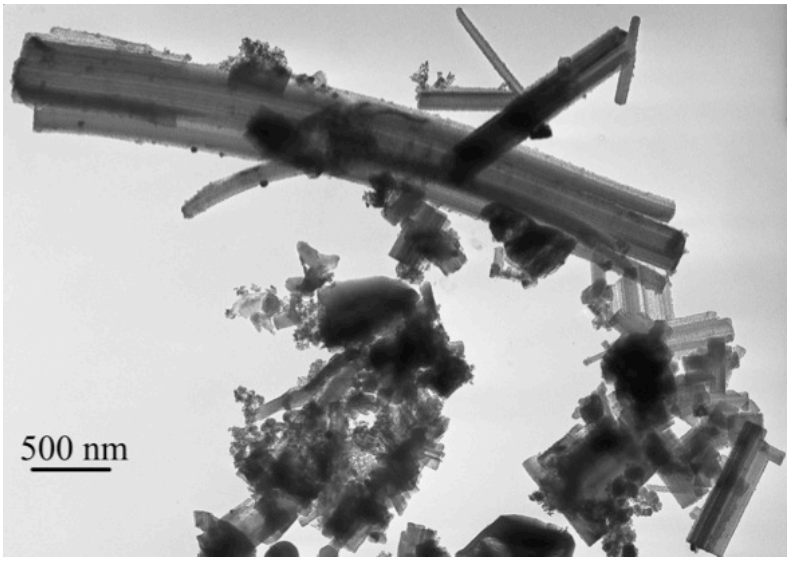

Figure 5.2: TEM image of boron nanorods before optimization.

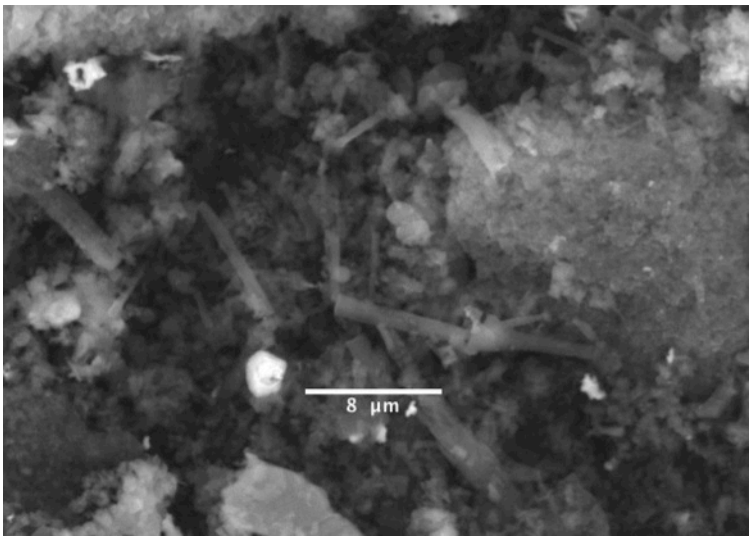

Figure 5.3: SEM image of boron nanorods before optimization.

X-ray powder diffraction (XRD) of the product has peaks at 21 degrees and 44 degrees. The broad peaks indicated the product is amorphous and the sharper peaks in the spectrum come from the sample holder (Figure 5.4). Based on TEM and XRD results, the scale up of the reaction procedure did not change the morphology or the size of the product.

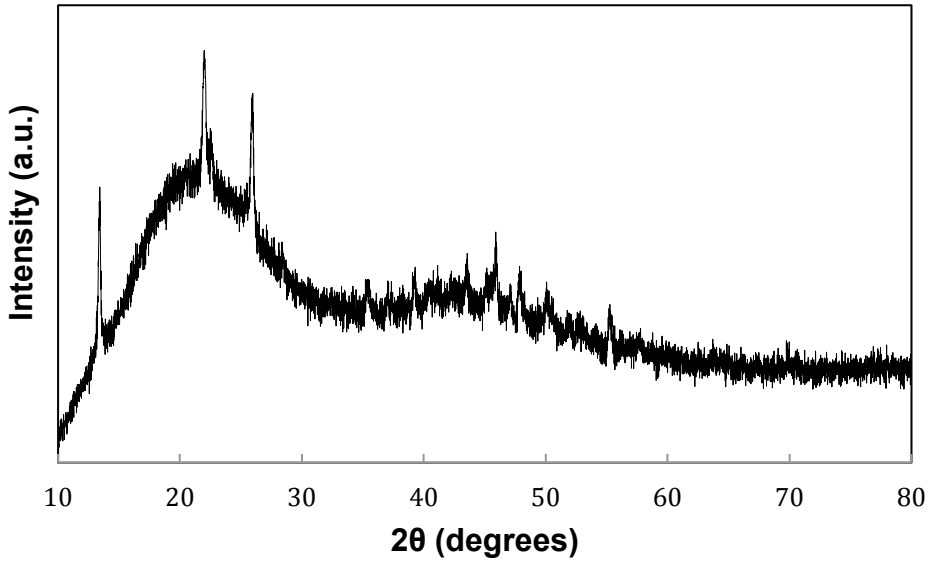

Figure 5.4: XRD spectrum of boron nanorods.

Other reducing agents were explored for this reaction. The few requirements looked at while searching for other metals were a low melting point, high reducing potential, and availability of the metals in the lab. Metals like barium, strontium, and calcium have an excellent reducing potential but high melting points; therefore, sodium was selected. The reaction between sodium and boron oxide is shown in equation 5.1:

$$B_2O_3 + 6Na \rightarrow 2B + 3Na_2O \qquad \text{(Equation 5.1)}$$

During the purification process, when methanol was added unreacted sodium was removed and then hot water was added, in which case the entire residue dissolved indicating there was only boron oxide in the residue. In conclusion, reduction of boron oxide using sodium to boron nanorods did not succeed.

5.3.2 Optimization of Reaction Conditions

5.3.2.1 Sonication

The original paper did not specify the sonication amplitude for the reaction; therefore, various amplitudes were studied, including one without any sonication. Sonication was used to mix the molten lithium and B_2O_3 via vibration. The TEM result of a reaction without sonication shows formation of amorphous structures but not any nanorods, signifying the key role of sonication on the formation of nanorods (Figure 5.5).

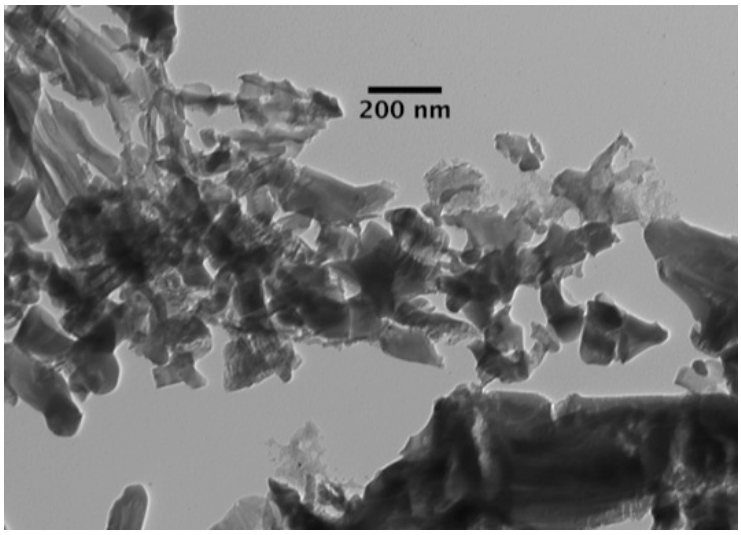

Figure 5.5: TEM image of boron nanorods prepared without sonication.

When different amplitudes were implemented on the synthetic procedure at higher sonication amplitude, an improvement on the nanostructures was observed (Figure 5.6). The high sonication amplitude produces a strong vibration, which enhances the interaction between molten lithium and B_2O_3. However, a sonication amplitude higher than 60% leads to splattering of both starting materials as well as products. When all the TEM results of 20%, 40%, 60%, and 80% sonication amplitude were compared, 60% sonication amplitude resulted in the synthesis of a large amount of boron nanorods without any loss of starting material or product.

Energy-dispersive X-ray spectroscopy (EDX) analysis of the boron nanorods shows the product was mostly composed of boron with 90 % atomic weight (Figure 5.7). The small amount of oxygen is attributed to surface oxidation of boron in air, which is reported in other literatures.[3,4] In addition, traces of sodium, silicon, and nickel that originated from glassware and crucibles were also present.

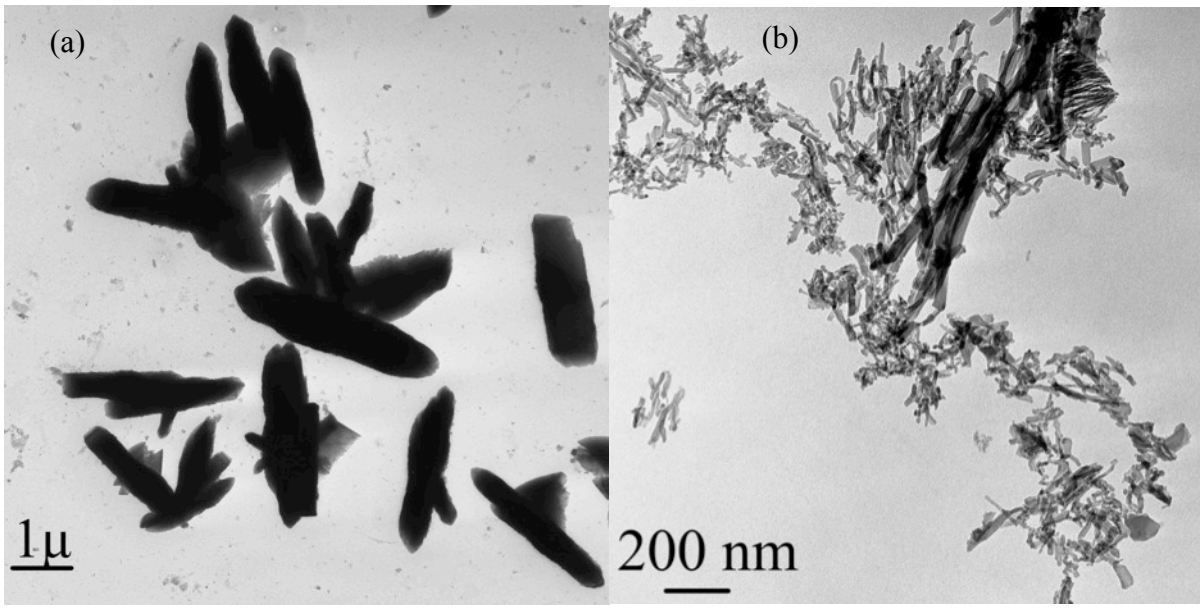

Figure 5.6: TEM images of boron nanorods (a) prepared with 40% sonication amplitude and (b) prepared using 60% sonication amplitude.

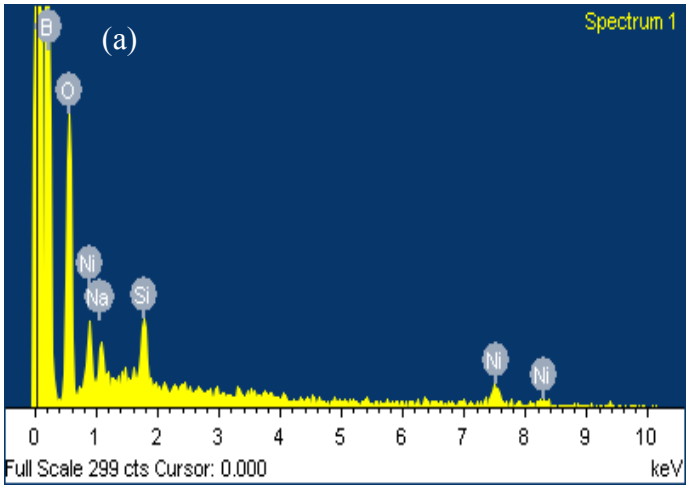

(b)

Element	Weight %	Atomic %
B	85.44	90.13
O	13.30	9.48
Na	0.26	0.13
Si	0.30	0.12
Ni	0.70	0.14
Total	100	100

Figure 5.7: (a) EDX Spectrum of boron nanoparticles prepared at 60% sonication amplitude. (b) EDX data of boron nanoparticles prepared at 60% sonication amplitude.

5.3.2.2 Temperature

The melting point of lithium is 180°C, which is the lowest temperature at which the reaction can be performed, so temperatures starting at 180°C up to 300°C were explored. TEM data has established that nanorods synthesized at elevated temperatures exhibit sharp edges, a diameter between 10-20 nm, and a length up to 500 nm (Figure 5.8). However, there was no significant difference in structure between nanorods that were synthesized at 280°C and 300°C. In addition, the 280°C reaction consumes less energy; as a result, it was selected to be the optimized reaction temperature.

XRD data showed the change in temperature did not improve or transform the phase of the product. The nanorods still maintained an amorphous structure. Attenuated total reflection (ATR-FTIR) spectrum of boron nanorods displays a peak at 1322 cm^{-1} which corresponds to B-O band, showing an oxidation of boron which is also reported in other literatures.[5] In addition, a peak at 3240 cm^{-1} is recognized as OH group from the absorbed moisture (Figure 5.9).

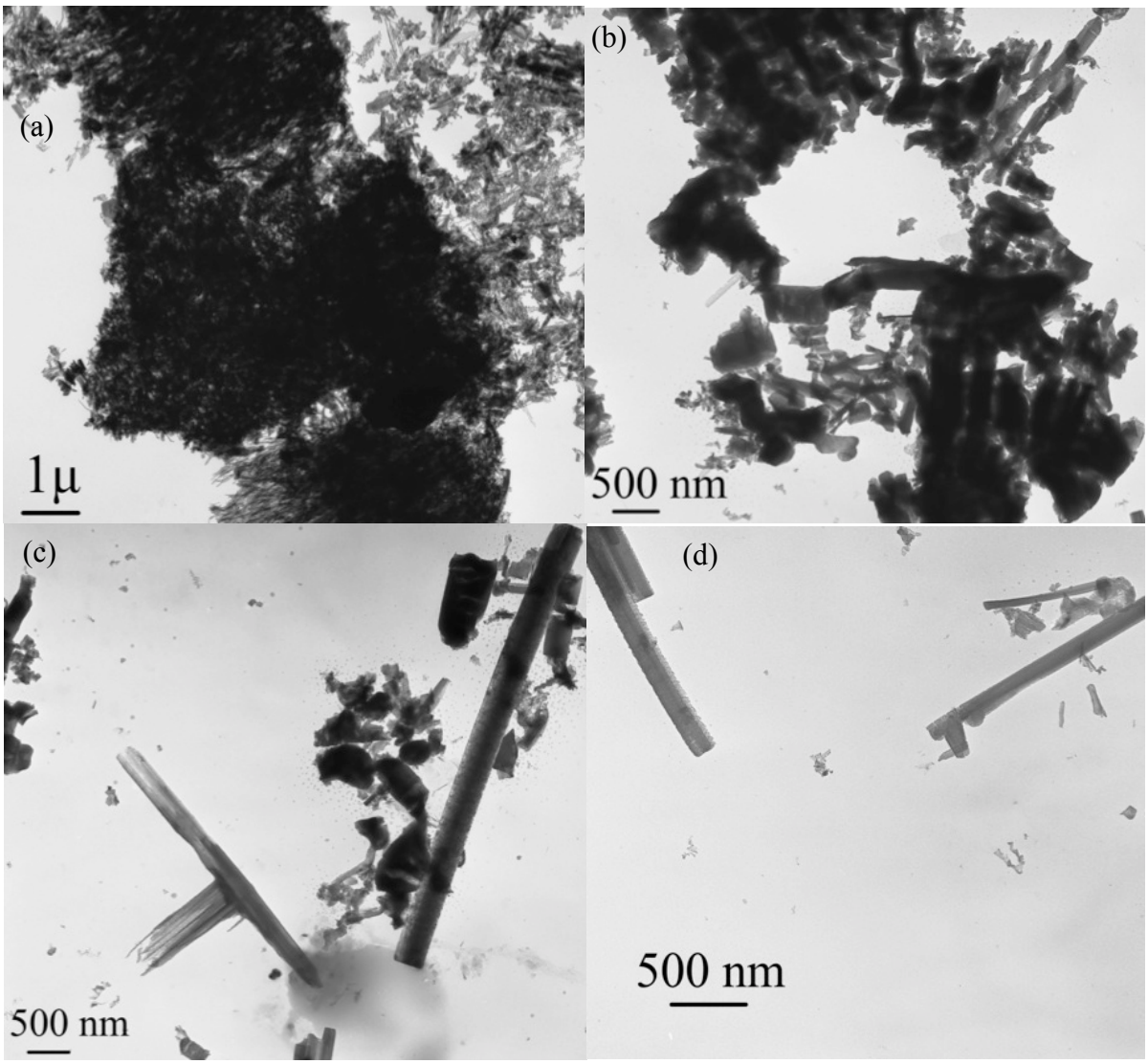

Figure 5.8: TEM images of boron nanorods synthesized (a) at 210°C, (b) at 235°C, (c) at 260°C, and (d) at 280°C.

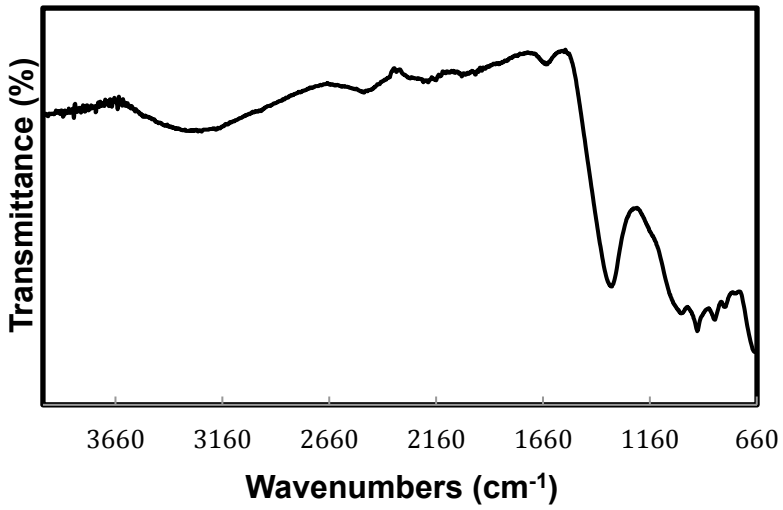

Figure 5.9: ATR-FTIR spectrum of boron nanorods synthesized at 260°C.

5.3.2.3 Reaction Time

The amount of time the reaction was sonicated after the addition of boron oxide also impacted the formation of boron nanorods. An increase in the length of time resulted in nanorods with defined shapes and higher yield. The TEM shows the resulting nanorods and tubular (Figure 5.10 c) structures have a diameter between 20-500 nm and a length of up to 12 μm (Figure 5.10). Furthermore, comparing the results between three and four hours reaction time, there was no evidence of improvement in yield or morphology of the product when the reaction was let to run for four hours.

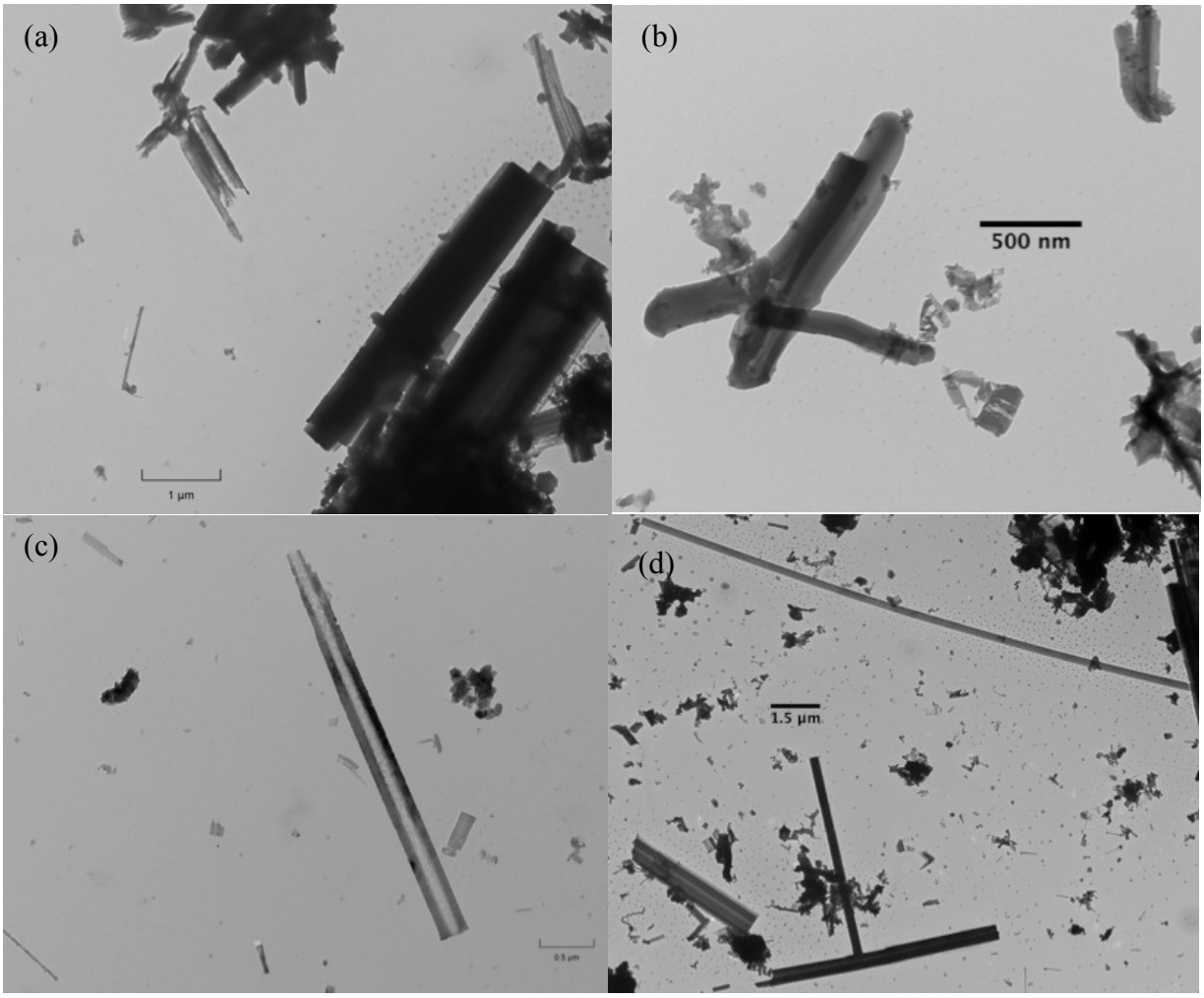

Figure 5.10: TEM images of boron nanorods synthesized (a) at 30 min., (b) 1 hr., (c) 1.5 hrs., and (d) 3 hrs.

The ATR-FTIR measurements of the resulting nanorods at various reaction times were all similar, containing corresponding peaks between temperature and reaction time, suggesting that the length of time did not affect the products' elemental composition or susceptibility to oxidation (Figure 5.11). In addition, the XRD analyze of the products were identical to each other, containing broad peaks at 21 degrees and 44 degrees, confirming the temperature did not change the non-crystalline phase.

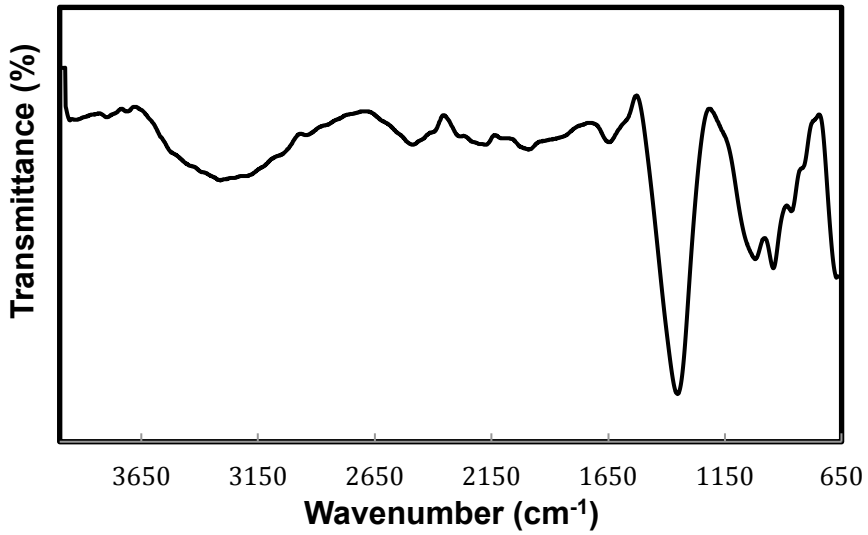

Figure 5.11: ATR-FTIR spectrum of boron nanorods synthesized for three hours.

5.3.3 Functionalization of Boron Nanorods

In order to use boron nanorods for biological application, surface modification is required; this was accomplished by both steric interaction and the formation of a covalent bond with other organic compounds. In addition, surface modification of the nanorods can lead to water-soluble products. The functionalization of boron nitride nanotubes with amine-terminated PEG (NH_2-PEG-NH_2) was reported,[6] and a similar idea was implemented to modify our boron nanorods. A TEM image of boron nanorods functionalization with bis (3-aminopropyl)-terminated PEG shows the presence of rods in the aqueous layer establishing the water-soluble characteristic of the boron nanorods (Figure 5.12).

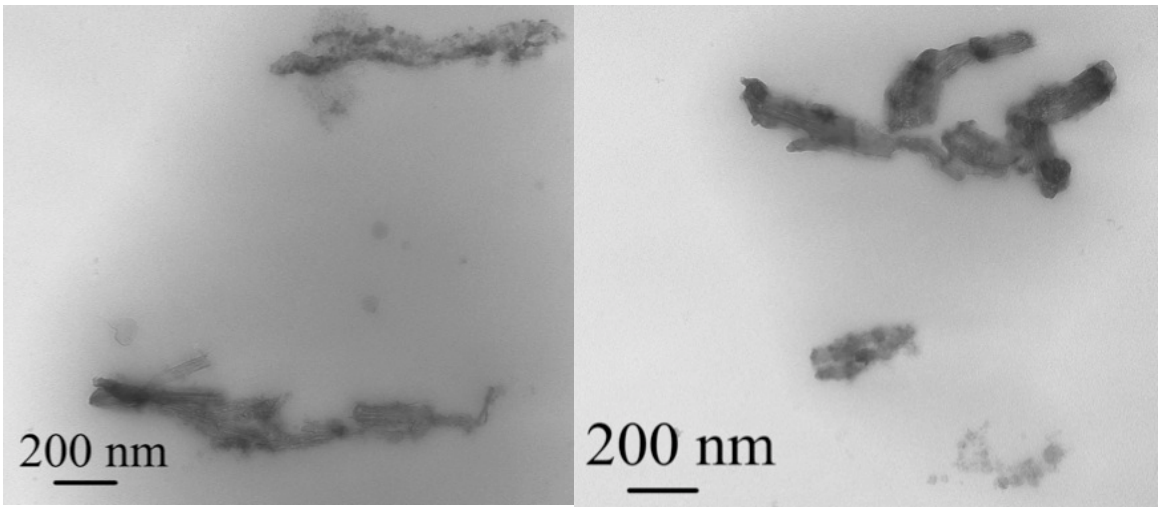

Figure 5.12: TEM images of bis (3-aminopropyl)-terminated PEG functionalized boron nanorods.

The electron-deficient boron bearing a partial negative charge (δ^-) and electron-rich (δ^+) amine of NH_2-PEG-NH_2 form a covalent bond securing the attachment of the two moieties. The ATR-FTIR analysis of the product confirms the surface modification of the nanorods with peaks at 1659 cm^{-1}, 2889 cm^{-1}, and 3486 cm^{-1} that are due to carboxyl groups, aliphatic C-H bonds, and amine groups, respectively. On the other hand, the peak at 1357 cm^{-1} corresponds to the B-O band of the oxidized boron nanorods (Figure 5.13).

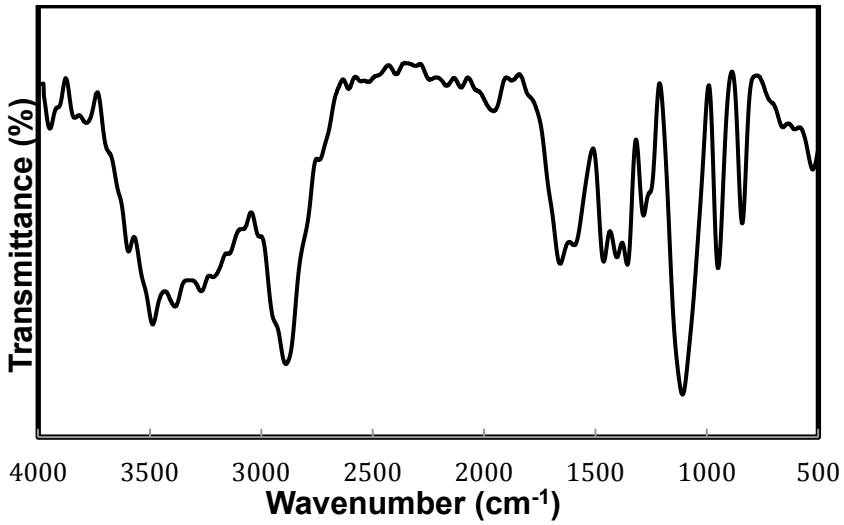

Figure 5.13: ATR-FTIR spectrum of bis (3-aminopropyl)-terminated PEG functionalized boron nanorods.

A TEM image of the product that used hydrogen peroxide to attach hydroxyl groups on the boron nanorods shows no evidence of born nanorods in the aqueous layer. The absence of nanorods implies the surface modification did not occur (Figure 5.14). Both the first and second trials show similar results.

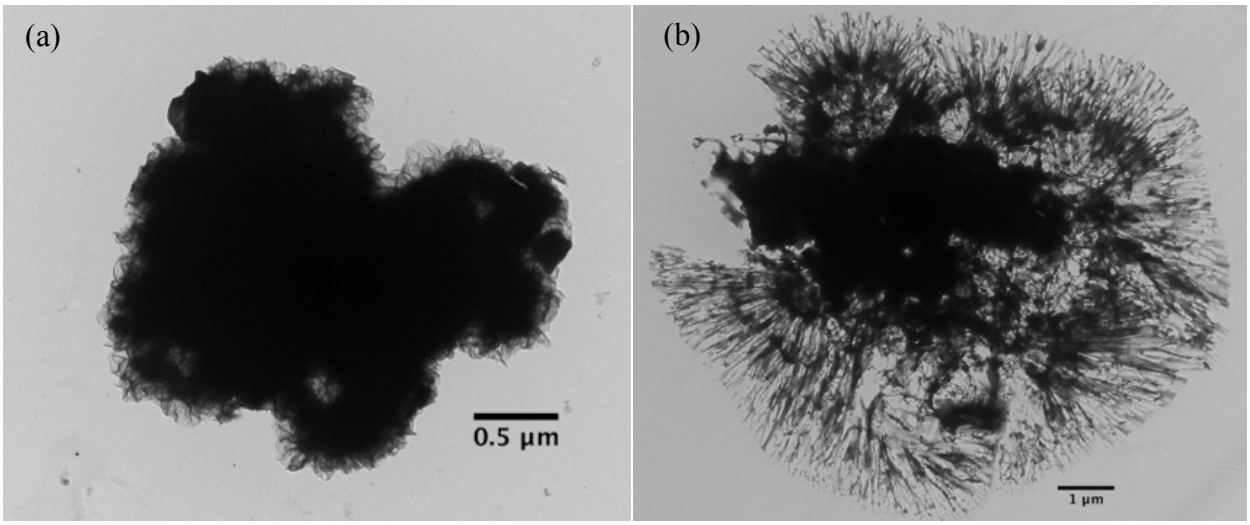

Figure 5.14: TEM images of hydrogen peroxide functionalization boron nanorods. (a) First trial and (b) second trial.

The last surface modification was performed using folic acid, and the TEM of the reaction product does not contain any nanorods (Figure 5.15). However, the UV-Vis shows the presence of folic acid in the product but does not show the presence of boron nanorods, suggesting that the reaction did not result in a formation of a bond between boron nanorods and folic acid.

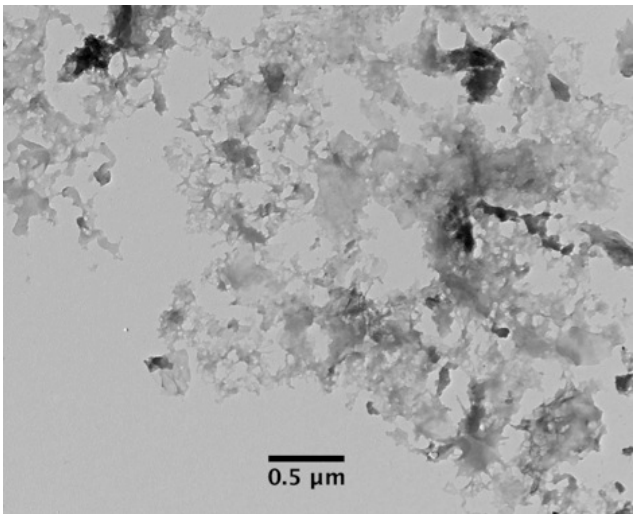

Figure 5.15: TEM image of folic acid functionalization trial.

5.4 Summary and Conclusion

The synthetic procedure of boron nanorods was explored to optimize product formation. Various aspects of the reaction - such as a reducing agent, sonication, temperature, and time - were studied, and a new reaction condition for the synthesis of boron nanorods was developed. The optimization result establishes that a 60% sonication amplitude at 280°C for three hours produced boron nanorods with well-defined shapes and high yields. In addition, the product was predominantly composed of boron with a small amount of oxygen, proving the purity of the product. However, nanorods that were synthesized using the optimal reaction condition were amorphous solid. The functionalization of the boron nanorods with bis (3-aminopropyl)-terminated PEG was successful in making the nanorods water soluble and biocompatible. On the other hand, the attempt to modify the boron nanorods with folic acid and hydrogen peroxide did not produce the intended result.

References

1. Yang, Q.; Sha, J.; Wang, L.; Yuan, Z.; Yang D., Aligned single crystal Al-catalyzed boron nanorods on Si substrates. *Eur. Phys. J.* B, 2007, 56, 35–39.

2. Zhu, D.M.; Kisi, E., Synthesis and Characterization of Boron/Boron Oxide Nanorods. *J Aust. Ceram. Soc,*, **2009**, 45[2], 49-53.

3. Chakrabarti, A.; Xu, T.; Paulson, L. K.; Krise, K. J.; Maguire, J. A.; Hosmane, N. S., Synthesis of Boron Nanorods by Smelting Non-Toxic Boron Oxide in Liquid Lithium. *J. Nanomater*., **2010**, 589372.

4. Devener, B.V.; Perez, P.L.; Anderson, S.L.; Air-stable, unoxidized, hydrocarbon-dispersible boron nanoparticles. *J. Mater. Res.,* **2009**, 24 (11), 3462-3464.

5. Siqueira, R.; Yoshida, I.; Pardini, L.; Schiavon, M.; Poly(borosiloxanes) as precursors for carbon fiber ceramic matrix composites. *Mat Res*., **200**7, 10(2), 147-151.

6. Xie, S.; Wang, W.; Fernando, K.; Wang, X.; Lin, Y.; Sun, Y.; Solubilization Of Boron Nitride Nanotubes. *Chem. Commun.* **2005**, 3670-3672.

Chapter 6

CONCLUSION AND FUTURE WORK

6.1 Summary

The research performed in this dissertation highlights the synthesis of boron-based zero-dimensional (0-D) and one-dimensional (1-D) nanostructures as well as the surface modification of these nanostructures. Chapter 1 dealt with the history and development of nanotechnology and nanomaterials. It also described the applications of nanostructures, which is the main reason the field has gained the interest of many researchers. Chapter 2 provided the different characterization methods used throughout the research, the concept behind each technique, and the useful information we collected from these instruments. Chapter 3 discussed the synthesis of 0-D boron nanoparticles followed by the formation of boron/iron oxide core/shell nanoparticles. The core/shell nanoparticles were developed to utilize the surface of the iron oxide shell for functionalization. The functionalization of iron oxide with multiple organic moieties to create a water-soluble boron carrier as well as the cytotoxicity of these water-soluble boron/iron oxide nanoparticles were covered. Also, the chapter clarified why iron oxide was one of the ideal candidates for designing core/shell nanoparticles with the magnetic measurement data of the bare boron/iron oxide core/shell nanoparticles and water-soluble core/shell nanoparticles. Chapter 4 described the synthesis and functionalization of boron/silica core/shell nanoparticles as well as

the toxicity of the modified nanoparticles. Chapter 4 explored similar parameters as Chapter 3; however, the primary difference is that Chapter 4 deals with boron/iron oxide core/shell nanoparticles whereas Chapter 4 deals with boron/silica core/shell nanoparticles. Chapter 5 focused on the synthesis of 1-D boron nanorods using a bottom-up approach with a reduction of boron oxide by lithium. Several reaction parameters—such as reaction time, temperature, and sonication amplitudes—were investigated in detail. Furthermore, the surface functionalization of the boron nanorods produced using the optimal reaction conditions was presented.

6.2 Future Work

6.2.1 Boron-Based Core/Shell Nanoparticles

The development of core/shell nanoparticles allows us to modify and use boron for biomedical application via making boron nanoparticles water soluble and biocompatible. More water-soluble compounds should be prepared followed by cytotoxicity, *in vitro*, and *in vivo* bio-distributional studies. This will determine if the compound can achieve the necessary boron concentration (35 μg/g of tissue or 10^9 ^{10}B atoms) for the use of boron neutron capture therapy (BNCT). A large concentration of these nanoparticles can be delivered to cancer cells via targeted delivery. This method uses compounds that have an overexpression of receptor sites in tumor cells. In this case, the core/shell nanoparticles can be tagged with these molecules so that the receptor sites on the tumor cells can recognize and incorporate the molecules into an intercellular cavity or cytoplasm (Figure 6.1).[1-4]

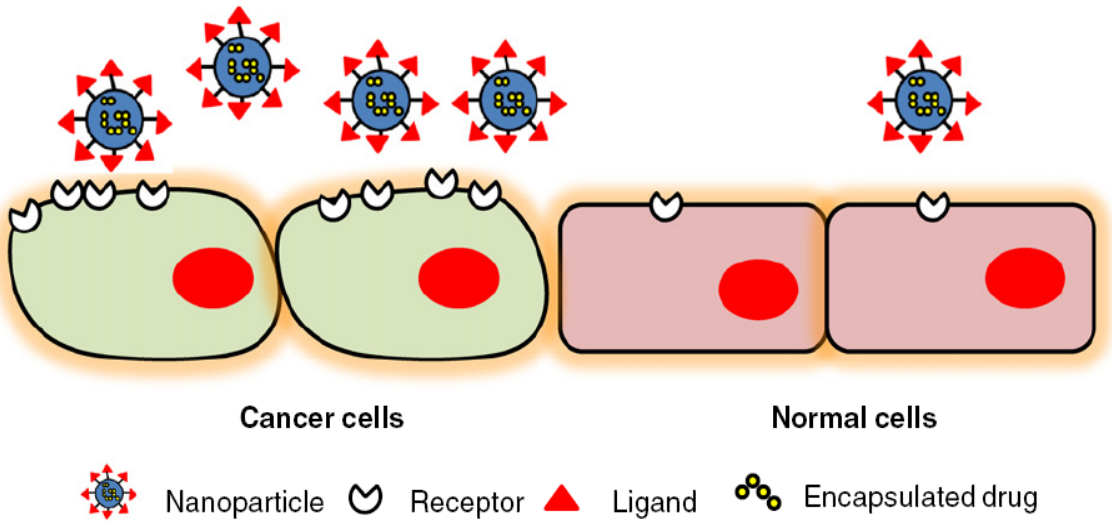

Figure 6.1: Drug delivery via direct surface modification.[1]

On the other hand, the nanoparticles can be encapsulated in liposomes by which the drug will be transported into the cell through endocytosis. This approach does not require any modification of the nanoparticles and is as effective as the method mentioned above. In addition, both water-soluble and non-water-soluble drugs can be carried to a cancer cell using the hydrophilic space and a hydrophobic bilayer of liposome, respectively. The liposome hydrophilic head can be modified to ensure the delivery of the boron containing compounds to tumor cells (Figure 6.2).[1,5,6]

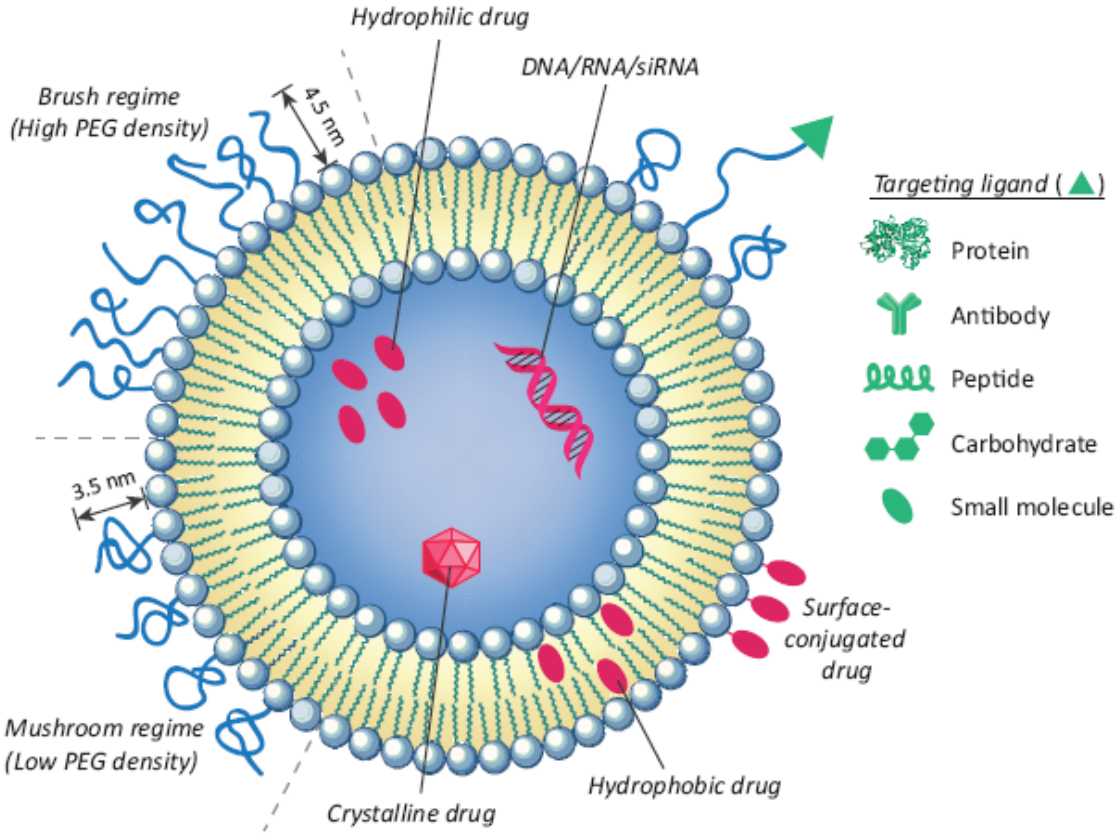

Figure 6.2: Drug delivery via liposomal encapsulation.[1]

Consequently, BNCT should be performed using the modified core/shell nanoparticles in small animals.

6.2.2 Boron Nanorods

The optimization of reaction conditions for the synthesis of boron nanorods improved the morphology and yield of the product. However, the product still contains nanorods with a wide range of size. Therefore, other reducing agents and reaction factors should be studied in order to create nanorods with uniform dimensions and narrow size distribution.

Biomedical and other applications of boron nanorods will depend on the ability to alter the surface of the rods for the intended purpose. Particularly, the use of boron nanorods for biological studies will require the nanorods to be soluble in various solvents and biocompatible or nontoxic to health cells. With this in mind, functionalization of boron nanorods with organic functional groups should be explored.

References

1. Çağdaş, M.; Sezer, A.; Bucak, S. Liposomes As Potential Drug Carrier Systems For Drug Delivery. *Application of Nanotechnology in Drug Delivery,* InTech**,** 2014.

2. De Jong, W. H., & Borm, P. J. (2008). Drug delivery and nanoparticles: Applications and hazards. *Int. J. Nanomedicine*, **2008**, 3(2), 133–149.

3. Ulbrich, K.; Hekmatara, T.; Herbert, E.; Kreuter, J. Transferrin- And Transferrin-Receptor-Antibody-Modified Nanoparticles Enable Drug Delivery Across The Blood–Brain Barrier (BBB). *Eur. J. Pharm. Biopharm.* **2009**, 71, 251-256.

4. Haley, B.; Frenkel, E. Nanoparticles For Drug Delivery In Cancer Treatment. Urol Oncol-Semin. Ori. **2008**, 26, 57-64.

5. Hong, C.; Nam, Y. Functional Nanostructures For Effective Delivery Of Small Interfering RNA Therapeutics. *Theranostics,* **2014**, 4, 1211-1232.

6. Hofheinz, R.; Gnad-Vogt, S.; Beyer, U.; Hochhaus, A. Liposomal Encapsulated Anti-Cancer Drugs. *Anti-Cancer Drugs,* **2005**, 16, 691-707.

APPENDIX

THE ROLE OF SURFACTANTS IN SYNTHESIS OF ZNS NANOSTRUCTURES

Even though the focus of the research done in this dissertation was on boron-based nanostructures, there was also some work done on ZnS nanostructures. This work was performed to gain a better understanding of how different kinds of surfactants dictate the formation of specific ZnS nanostructures.

A.1 Introduction

Zinc sulfide (ZnS) nanostructures are semi-conductor inorganic materials that consist of zinc and sulfur with tetrahedral coordination. ZnS is mainly found on the earth's crust as sphalerite in many parts of the world, mainly in Germany and Switzerland. However, sphalerite ore contains contamination such as iron, which changes the color from white to black. ZnS nanostructures can be used for many applications, including luminescence materials,[1-6] gas sensors,[7-9] chemical sensors,[10,11] nanogenerators,[12,13] biosensors,[10,14,15] field effect transistors,[10,16,17] and catalysis.[18,19] We will discuss some of these applications in detail.

Luminescence is a process of light emission and can arise from various sources. Furthermore, the luminescence process is categorized based on the emission source. For

instance, photoluminescence is an emission that is observed when a material is excited using a photon source and cathodoluminescence is caused by electron excitation. In 1866 Theodore Sidot became the first to explore the photoluminescence property of ZnS. The photoluminescence absorption peak of ZnS can vary based on the synthetic approach, shape, and size of the nanostructure.[20] To illustrate this point, ZnS nanobelts and nanosheets synthesized via vapor-solid mechanisms have an emission peak at 545 nm and 440 nm while ZnS nanorods and nanowires synthesized via vapor-liquid-solid mechanism have an emission peak at 530 nm and 440 nm.[21] Luminescence materials are mainly used for safety, particularly to mark emergency exits and stairways in buildings since the light can be seen in a smoke-filled room.[22]

ZnS nanostructures have been widely used as photocatalysts for the removal of harmful water contaminants such as p-nitrophenol, dyes, and halogenated benzene derivatives.[20] In addition, the reduction of CO_2 to formic acid was achieved using ZnS nanocrystals.[19] The efficiency of CO_2 reduction increases with the use of sodium hypoposphite (NaH_2PO_2) and sodium sulfide (Na_2S).[23] Berdol and Kaczmarek reported that ZnS with ligand-modified surface can replace the use of metal catalysts for the reduction of ethanol to water and CO_2. This work shows that ZnS is inert from oxidation and surface poisoning that decrease the turnover frequency or efficiency of the catalyst.[24]

Nanomaterial-based sensors have been explored for quite some time, but ZnS was not the front-runner because of low-carrier density. However, in recent years ZnS nanostructures such as nanobelts were used to determine the presence of hydrogen gas[9] and the amount of oxygen in the surrounding area.[7] Moreover, carbon tetrachloride, a toxic compound that is harmful to humans and the environment, was detected using cataluminescence ZnS.[25] The ZnS nanosensor exhibited

a significantly large cataluminescence emission when carbon tetrachloride was introduced. ZnS can also be used as a biosensor following a surface modification with biocompatible compounds.

Most of these applications utilize the large bandgap of ZnS, which can vary from 3.72 eV to 3.77 eV based on crystalline structures. ZnS has two crystalline structures, namely zinc blend and wurtzite. Zinc blend (ZB), also known as sphalerite, has a cubic form with an ABCABC staking pattern that is the most stable and common form of ZnS at low temperatures. Furthermore, zinc blend exists in F4-3 m space group where a = b = c = 5.42 Å and Z = 4 and has a smaller bandgap of 3.72 eV.[20] On the other hand, wurtzite has a hexagonal form with an ABAB staking pattern; exists in a $P6_3mc$ space group where a = b = 3.82 Å, c =6.26 Å, and Z = 2; and retains a 3.77 eV bandgap (Figure A.1).[26] Both ZB and wurtzite have Zn and S maintaining a tetrahedral coordination. ZB form can be transformed to wurtzite at 1020°C.

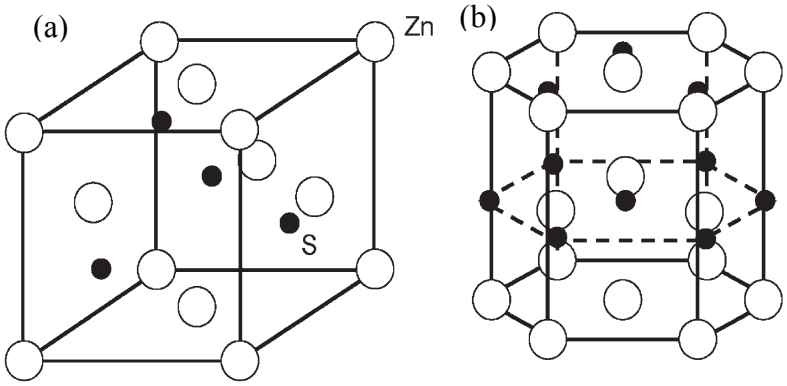

Figure A.1: Crystalline forms of zinc sulfide. (a) Zinc blend (ZB) and (b) wurtzite.[26]

A.2 Zinc Sulfide Nanostructures

Zinc sulfide nanostructures can be categorized as 0-D nanostructures, which contain quantum dots, core/shell nanocrystals, and hollow nanocrystals; 1-D nanostructures, which contain nanowires (NWs), nanorods (NRs), nanotubes (NTs), nanobelts (NBs), and nanoribbons (NRs); and 2-D nanostructure containing ZnS thin films. All of these structures can be synthesized using both top-down and bottom-up approaches. We will discuss the different synthetic approaches developed to produce 0-D nanostructure and 1-D nanostructure.

A.2.1 Synthesis of 0-D ZnS Nanostructure

Cubic ZnS quantum dots were synthesized by Hyeon et al. using $ZnCl_2$ as a zinc source and sulfur with oleylamine and trioctylphosphine oxide (TOPO) at 320°C . The thermal reaction produced crystalline quantum dots with an average diameter of 11 nm. Although the reaction required a high temperature, it was successful in producing ZnS quantum dots with uniform size distribution.[27]

ZnS core/shell structures were used to expand the luminescence efficiency of ZnS in combination with other materials such as cadmium selenide (CdSe) and iron oxide (Fe_3O_4). ZnS core/shell structures are usually synthesized in two steps. First, the core CdSe or Fe_3O_4 is prepared, followed by the formation of the ZnS shell. For example, Weller et al. prepared well-dispersed CdSe nanoparticles using in hexadecylamine (HDA), trioctylphosphine (TOP), and trioctylphosphine oxide (TOPO).[28] The resulting CdSe nanoparticles with 4 nm diameter were coated with ZnS and the luminescence efficiency increased from 10-25% to 66%.

Xu et al. synthesized ZnS hollow spheres in hydrothermal reaction using thiocarbamide, $(CH3COO)_2Zn.2H_2O$, and water. The hollow spheres produced are hexagonal and have a diameter between 200-300 nm with an average thickness of 20 nm.[29] Alternatively, smaller hollow spheres with diameters between 50 to 70 nm and 15 nm thickness were fabricated by Qi et al.[30] Table A.1 shows the different 0-D ZnS nanostructures that were produced and their synthesis approaches.[20]

Table A.1

Synthesis of 0-D ZnS Nanostructures

Nanostructure	Composition	Synthesis method	*T* (°C)
Nanocrystals	ZnS	Thermal reaction with $ZnCl_2$ and S in oleylamine	320
		Solution approach in a polyol medium	150
		Chemical reaction in non-coordinating solvents	340, 300
		Thermolysing $Zn(exan)_2$ with OA and TOP as precursor solvents	150–250
		Liquid–solid–solution (LSS) process	90
		Chemical reduction route	RT
		Aging reaction mixtures	300
Core/shell nanocrystals	$CuInS_2$/ZnS (shell)	Two-step procedure	230
	Mn-CdS/ZnS (shell)	Three-step synthesis method	280
	CdS/ZnS (shell)	Two-step procedure	250–280;180
	CdSe/ZnS (shell)	Lyothermal technique	250
	CdSe/ZnS (shell)	Organometallic synthesis in HDA–TOPO–TOP mixture	300;220
	CdSe/ZnS (shell)	Two-step synthesis	360, 220
	CdSe/CdS/$Zn_{0.5}Cd_{0.5}S$/ZnS (shell)	SILAR technique	200–260
Hollow nanocrystals	Fe_3O_4/ZnS (shell)	Corrosion-aided Ostwald ripening process	150
	ZnS	Bacteria-template sonochemical route	RT
	ZnS	Hydrothermal route	140
	ZnS	Hydrothermal route	120
Doped nanocrystals	Mn-ZnS	Organometallic and inorganic synthesis method	–
	Mn-ZnS	Solution approach	RT
	Co-ZnS	Solution-phase thermal decomposition method	150
	Cu-, Pb-ZnS	Organometallic synthesis method	300
Alloyed nanocrystals	$Zn_xCd_{1-x}S$	Solution chemical route	270
	$Zn_xCd_{1-x}S$	Thermolyzing a mixture of $Cd(exan)_2$ and $Zn(exan)_2$ precursors	210
	$Zn_xCd_{1-x}S$	Chemical reaction of CdO- and ZnO-oleic acid complexes with sulfur	300

A.2.2 Synthesis of 1-D ZnS Nanostructures

One-dimensional ZnS nanostructures are predominantly produced using a vapor-phase approach, in which the zinc and sulfur precursor exist as a vapor and then are deposited onto a substrate where the final structure grows. During the deposition process various reaction parameters, for example, temperature, flow rate of carrier gas, and substrate, can be altered to produce ZnS nanostructures with particular shapes and sizes.[26] In general, vapor-phase synthesis requires high temperature and a carrier gas, but there are other methods such as the hydrogel[31] and liquid crystal template[32] route that can fabricate 1-D ZnS nanostructures in an ambient temperature.

ZnS nanowires and nanorods were prepared using a top-down approach using ZnS powder via thermal evaporation at 900°C.[33] The nanowires have diameters ranging from 30-60 nm and can grow to micrometers in length. Low-temperature synthesis of ZnS nanowires was performed using hexagonal liquid crystal as a template for the growth of the nanowires. Furthermore, nanotubes can be created via template-assisted synthesis.[32] Table A.2 contains various synthetic methods used to manufacture 1-D ZnS nanostructures.[20]

In our laboratory, we explored the role of surfactants in the synthesis of ZnS nanostructures. Before moving to the synthesis, we will briefly discuss the use of surfactants. Surfactants are compounds that contain both hydrophilic heads and hydrophobic tails. Surfactants are classified into four groups known as anionic, cationic, nonionic, and zwitterionic based on the charge the hydrophilic heads carry. As the name indicates, anionic surfactants contain negatively charged heads, cationic contain positively charged heads, nonionic does not contain any charges, and zwitterionic contains both negatively and positively charged heads. In terms of nanomaterials,

surfactants were used mostly for two reasons, which are prevention of heads are exposed to the surroundings while the hydrophilic tails are intact inside (Figure A.2).[41] Nanostructures such as nanotubes or hollow spheres can be fabricated using the outer surface of the micelle and the inner cavity can be used to form nanorods, nanowires, and nanoparticles followed by the removal of the surfactant to recover pure nanostructure agglomeration through steric stabilization and shape-controlled synthesis via micelle formation.[34-40] Micelles are formed when a surfactant is oriented in a way that the hydrophilic agglomeration through steric stabilization and shape-controlled synthesis via micelle formation.[34-40] Micelles are formed when a surfactant is oriented in a way that the hydrophilic

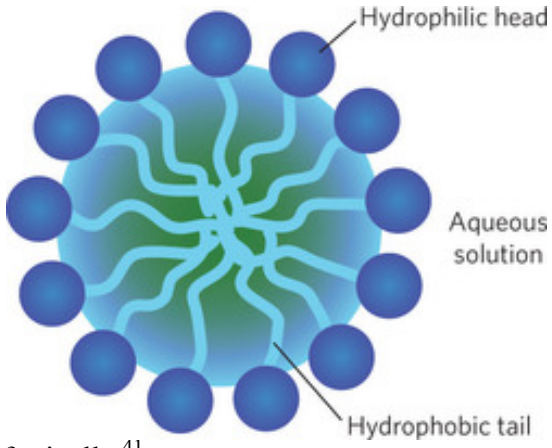

Figure A.2: Formation of micelle.[41]

In this chapter we will explore the synthesis of ZnS nanostructures using different reagents and the effect of surfactants' presence during the synthesis process. In addition, the amount of surfactant added to the synthesis process is investigated.

Table A.2

Synthesis of 1-D ZnS Nanostructures

Nanostructure	Synthesis method	T (°C)
Nanowires	Thermal evaporation method	900
	MOCVD process	–
	Liquid crystal template by γ-irradiation	RT
	Solvothermal route	180
	One-step wet-chemical approach	140
	VLS process	1200
	Thermal evaporation	400–500
	Molecular beam epitaxy (MBE) technique	430
	Solvothermal route	180
	Mild-solution chemistry approach	180
	Thermal evaporation method	1250
	Electrochemical-template method	RT
	Thermal evaporation process	1300
	Vapor phase deposition method	900
	Thermal evaporation of zinc powder and sulfur powder	580, 90
	Electrochemical-template method	120
	One-step CVD method	1200
	Hydrothermal synthesis route	180
	Electrodeposition-template method	120–130
	Hydrogen-assisted thermal evaporation method	1100
	Thermal physical evaporation	1000
	Carbothermal CVD process	500
	Organic assistant VLS method	1000
	VLS method	1100
	Thermal evaporation method	700
	Two-step thermal evaporation process	1050
	Pulsed laser vaporization	950
	Hydrogen-assisted thermal evaporation	1100
	Intermittent laser ablation-catalytic growth process	950
	Chemical vapor transport and condensation	900–950
	Direct reaction of Zn and S powders	750
	Solid-state reaction	RT
	Thermal evaporation method	1000
	VLS process	–
	Thermal evaporation	1050
Nanorods	Aqua-solution hydrothermal process	95
	Micro-irradiation-assisted growth	RT
	Solvothermal approach	135–250
	Sulfidation of ZnO nanorod arrays	600
	Radio frequency magnetron sputtering technique	−40 to 0
	Solvothermal decomposition	150–200
	Solution method in the presence of block copolymer	105
	Plasma-assisted MOCVD process	650
	Thermolysing $Zn(exan)_2$ with OA and TOP as precursor solvents	150–250
	Thermal evaporation	1100
	Thermal evaporation	970
	Hydrothermal synthesis	180

Continued on following page

Table A.2 (continued)

Nanostructure	Synthesis method	T (°C)
Nanotubes	Conversion of ZnO nanobelts	1350, 90
	High-temperature thermal-chemical reaction route	1500–1700
	MOCVD-template method	400
	Ultrasonic chemical solution method	RT
	Wet-chemistry method	140
	Hydrogel template route	RT
	Thioglycolic acid-assisted solution route	130–180
	Atomic layer deposition	75
	Thermochemical process	1250
	Chemical conversion of ZnO columns	400
	Solution route by using the hard templates of CNTs	120
Nanobelts	CVD process	1100
	Vapor-phase transport process	900
	Hydrogen-assisted thermal evaporation	1120
	Under moist gas conditions	
	Thermal evaporation	1100
	Thermal evaporation	1100
	Conversion reaction of CdS NBs	800
	Rapid CVD process with Au as catalyst and graphite as reductant	1050
	Thermal evaporation	1150
	VLS process	1050
	Thermal evaporation	1150
	Solid–vapor phase thermal-sublimation technique	1050
	Thermal evaporation	900
	Diethylenetriamine-assisted solvothermal approach	180
	Controlled thermal process	1150
	Low-temperature thermochemistry route	640
	VLS process	1000
	Thermal evaporation	970
	VPT process	900–950
	Thermal evaporation	1200
	H_2-assisted thermal evaporation approach	900–1100
	Thermal evaporation	1050
	Thermal evaporation	1600
	Thermal evaporation	1100
	Solvothermal reaction and subsequent heat treatment	160, 250
	Thermal evaporation	1020
Nanoribbons	Au mediated thermal evaporation route	1000–1100
	CVD method	450
	Thermal evaporation using thiol-capped Au NPs as catalysts	1000
	Thermal evaporation process	1050
	Two-stage temperature-controllable thermal evaporation and condensation process	1180
	Thermal evaporation	1050
	Microwave-assisted solvothermal synthesis	400
	Hydrogen-assisted thermal evaporation	1100

A.3 Materials and Methods

A.3.1 Synthesis of Zinc Sulfide Nanostructures

A.3.1.1 Reaction with Zinc Chloride and Sodium Sulfide (Sample 1)

Zinc sulfide was prepared using zinc chloride ($ZnCl_2$) and sodium sulfide (Na_2S) as zinc and sulfur sources, respectively. Initially, $ZnCl_2$ solution (1M, 10 mL) and Na_2S solution (1M, 10 mL) were transferred into a 100 mL round-bottom flask and heated to 50°C with stirring for 1 hour. The product was then collected via centrifugation and purified by washing with deionized (DI) water and ethanol. The final product was dried under *vacuo* overnight. Further, a similar reaction was performed with assistance of sonication at room temperature. To illustrate, a 10 mL Na_2S solution (1M) was added dropewise to $ZnCl_2$ solution (1M, 10 mL) alongside sonication (80% amplitude) and the sonication was continued for an additional 30 minutes after the addition of the Na_2S solution was complete. The product was purified in a similar fashion as that stated above.

A.3.1.2 Reaction with Zinc Nitrate Hexahydrate and Sodium Sulfide (Sample 2)

A 10 mL solution of zinc nitrate hexahydrate ($Zn(NO_3)_2.6H_2O$, 1M) was prepared followed by dropewise addition of Na_2S solution (1M, 10 mL). The solution was sonicated for 30 minutes while the Na_2S solution was added and for another 30 minutes afterwards. The product was then collected via centrifugation and purified by multiple washes with DI water and ethanol. The final product was dried under *vacuo* overnight. Further, for one specific reaction, the flask was placed in ice bath to decrease the reaction temperature to 2°C. The reaction

temperature was later increased to room temperature and two surfactants, namely sodium dodecyl sulfate (SDS) and hexadecyl trimethyl ammonium bromide (CTAB), were added to the reaction (Table A.3). In addition, when surfactants were used, the zinc nitrate hexahydrate solution and the surfactant were sonicated for 10 minutes before the addition of Na_2S solution.

A similar reaction using $Zn(NO_3)_2.6H_2O$ (1M, 30 mL) and sodium sulfide nonahydrate ($Na_2S.9H_2O$, 1M, 30 mL) at room temperature was executed and other surfactants were tested (Sample 3)(Table A.4). The surfactants tested were triton X-100, sodium cholate hydrate, and sodium dodecylbenzenesulfonate (SDBS). In addition, these reactions were done in reverse order meaning the surfactants were dispersed with $Na_2S.9H_2O$ solution followed by the addition of $Zn(NO_3)_2.6H_2O$ solution. In some cases the final product from the above reactions was annealed at 800°C for 2 hours under an argon atmosphere.

Table A.3

Reaction Conditions for Sample 2

Reagents	Surfactant	Temperature
$Zn(NO_3)_2.6H_2O$ (1M, 10 mL)	SDS	Room temp.
Na_2S (1M, 10 mL)		
$Zn(NO_3)_2.6H_2O$ (1M, 10 mL)	CTAB	Room temp.
Na_2S (1M, 10 mL)		

Table A.4

Reaction Conditions for Sample 3

Surfactant	Wt. % of surfactant	Temperature (°C)	Time (hours)
Terephthalic acid	10	Room temp.	Overnight
SDS	10	Room temp.	Overnight
Triton X-100	10	Room temp.	Overnight
CTAB	10	Room temp.	Overnight
Sodium cholate hydrate	10	Room temp.	Overnight
SDBS	10	Room temp.	Overnight
Sodium cholate hydrate	10	60	Overnight

A.3.1.3 Reaction with Zinc Nitrate Hexahydrate and Thiourea (Sample 4)

A 0.5 M $Zn(NO_3)_2.6H_2O$ (25 mL) and 0.5 M thiourea (25 mL) solution was prepared and transferred into a round-bottom flask. The content in the flask was dispersed in a water bath sonicator for one hour. Then the flask was set under reflux at 120°C overnight. The product was then collected via centrifugation and purified with multiple washes of DI water and ethanol. The final product was dried under *vacuo* overnight. The same reaction was performed in the presence of SDS. Additionally, the reaction vessel was replaced by a Teflon container as an autoclave to

maintain the temperature and pressure generated during the reaction. This reaction was done at a slightly lower temperature of 110°C.

On the other hand, the two reagents were used in dimethyl sulfoxide (DMSO). A 7.43 g sample of $Zn(NO_3)_2.6H_2O$ and 1.9 g sample of thiourea were placed into a round-bottom flask. Then the flask was set under reflux while stirring at 150°C for 2 hours. The product was then collected via centrifugation and purified by multiple washes of DI water and acetone. The final product was dried under *vacuo* overnight. Table A.5 contains all the reaction conditions as well as the various surfactants used.

In addition to using single surfactants we explored the effect of combining different surfactants with identical weight % as well as diverse weight % (Table A.6).

Table A.5

Reaction Conditions for Sample 4

Surfactant	Wt. % of surfactant	Temperature (°C)	Time (hours)	Solvent
None	-	130 (reflux)	Overnight	DMSO
None	-	140 (reflux)	2	DMSO
None	-	160 (reflux)	2	DMSO
None	-	170 (reflux)	4	DMSO
SDS	5 &10	150 (reflux)	2	DMSO
CTAB	5 & 10	150 (reflux)	2	DMSO
Terephthalic acid	5, 10, & 20	150 (reflux)	2	DMSO
Terephthalic acid	10 & 20	150 (reflux)	Overnight	DMSO
Triton X-100	5, 10, 15, & 20	150 (reflux)	2	DMSO

Table A.6

Mixture of Surfactants

Surfactants		Wt. % of each surfactant	Temperature (°C)	Time (hours)	Solvent
Terephthalic acid	SDS	2.5 & 5	150 (reflux)	2	DMSO
Terephthalic acid	Triton X-100	5 & 10	150 (reflux)	2	DMSO
Terephthalic acid	CTAB	5 &10	150 (reflux)	2	DMSO
Triton X-100	CTAB	10	150 (reflux)	2	DMSO
Triton X-100	CTAB	10 (Triton X-100), 5 (CTAB)	150 (reflux)	2	DMSO

A.3.1.4 Reaction with Zinc Chloride and Thiourea (Sample 5)

A 3.40 g sample of $ZnCl_2$ and 1.9 g sample of thiourea were placed into a round-bottom flask with 25 mL of diethylene glycol methyl ether. Then the flask was set under reflux while stirring at 190°C for 2 hours. The product was then collected via centrifugation and purified with multiple washes of DI water and acetone. The final product was dried under *vacuo* overnight. Table A.7 displays the list of surfactants that were studied with these reaction conditions.

Table A.7

Reaction Conditions for Sample 5

Surfactant	Wt. % of surfactant
Terephthalic acid	5 & 10
Sodium cholate hydrate	5 & 10
pluronic F-127	5 & 10

In addition, the reaction was performed in a different solvent, namely anhydrous diglyme. Since the solvent used is anhydrous, the reaction requires a moisture-free environment. Therefore, the reagents were dried under vacuum then measured in a glovebox and the reaction container was purged with argon during the reaction. A typical reaction contains a 3.46 g sample of $ZnCl_2$ and 1.89 g sample of thiourea placed into a round-bottom flask with 25 mL of diglyme. Then the flask was set under reflux while stirring at 150°C for 2 hours. The addition of terephthalic acid to this reaction was investigated (Table A.8).

Table A.8

Reaction Conditions for Sample 5 in Diglyme

Surfactant	Wt. % of surfactant	Temperature (°C)
Terephthalic acid	5 & 10	150 (reflux)
Terephthalic acid	15 & 20	160 (reflux)

A.4 Results and Discussion

A.4.1 Synthesis of Zinc Sulfide Nanostructures

A.4.1.1 Reaction with Zinc Chloride and Sodium Sulfide (Sample 1)

There are many publications that focus on the synthesis of zinc sulfide (ZnS),[42-45] and in our research we started with the simple zinc and sulfur sources available, which were zinc chloride and sodium sulfide. The two reagents react in 1:1 ratio to form ZnS and a water-soluble sodium chloride (NaCl) salt that is removed during the purification process (Equation A.1). The transmission electron microscopy (TEM) image shows there is no development of nanostructure, which suggests higher temperature and sonication did not improve the formation of ZnS nanostructures (Figure A.3).

$$ZnCl_2+Na_2S\rightarrow ZnS+2NaCl \qquad \text{(Equation A.1)}$$

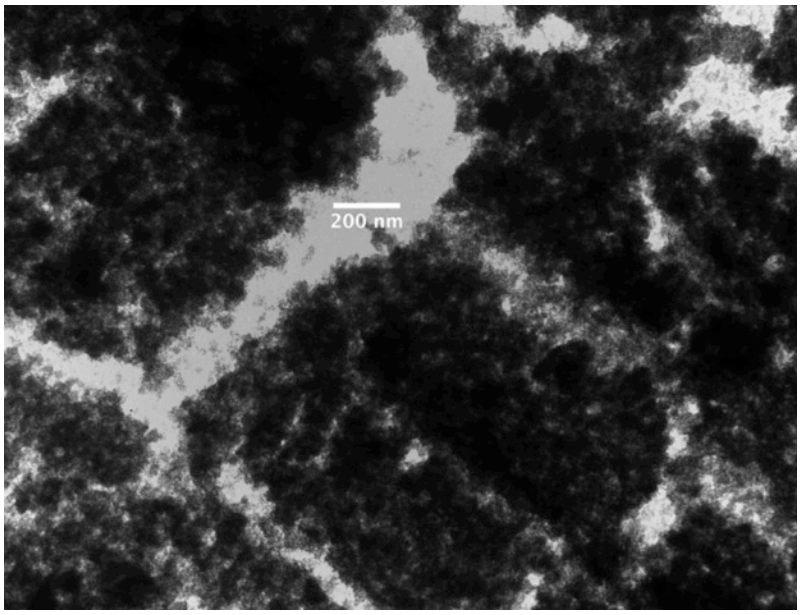

Figure A.3: TEM image of Sample 1.

A.4.1.2 Reaction with Zinc Nitrate Hexahydrate and Sodium Sulfide (Sample 2)

Since the reaction between zinc chloride and sodium sulfide did not result in formation of ZnS nanostructures, a different zinc source was explored. In this case, $Zn(NO_3)_2.6H_2O$ was reacted with Na_2S at ambient temperature (Equation A.2). During the reaction, the addition of Na_2S solution resulted in an instant precipitate formation. Therefore, a separate reaction was conducted at lower temperature (2°C) aiming to reduce the rate of precipitate formation. However, the TEM image of both reactions shows no evidence of ZnS nanostructures. Furthermore, the addition of anionic (SDS) and cationic (CTAB) surfactants did not improve the result (Figure A.4).

$$Zn(NO_3)_2.6H_2O + Na_2S \rightarrow ZnS + 2NaNO_3 + 6H_2O \qquad \text{(Equation A.2)}$$

In order to recover a favorable result, the above reaction was performed using a larger amount of starting materials and longer reaction time (Sample 3). An extended reaction period will give enough time for nucleation and growth leading to the development nanostructures. Various nonionic surfactants such as terephthalic acid, triton X-100, and sodium cholate hydrate; anionic surfactants such as SDS and SDBS; and a cationic surfactant CTAB (Figure A.5) were used and TEM images display the formation of well-defined nanoparticles (Figure A.6).

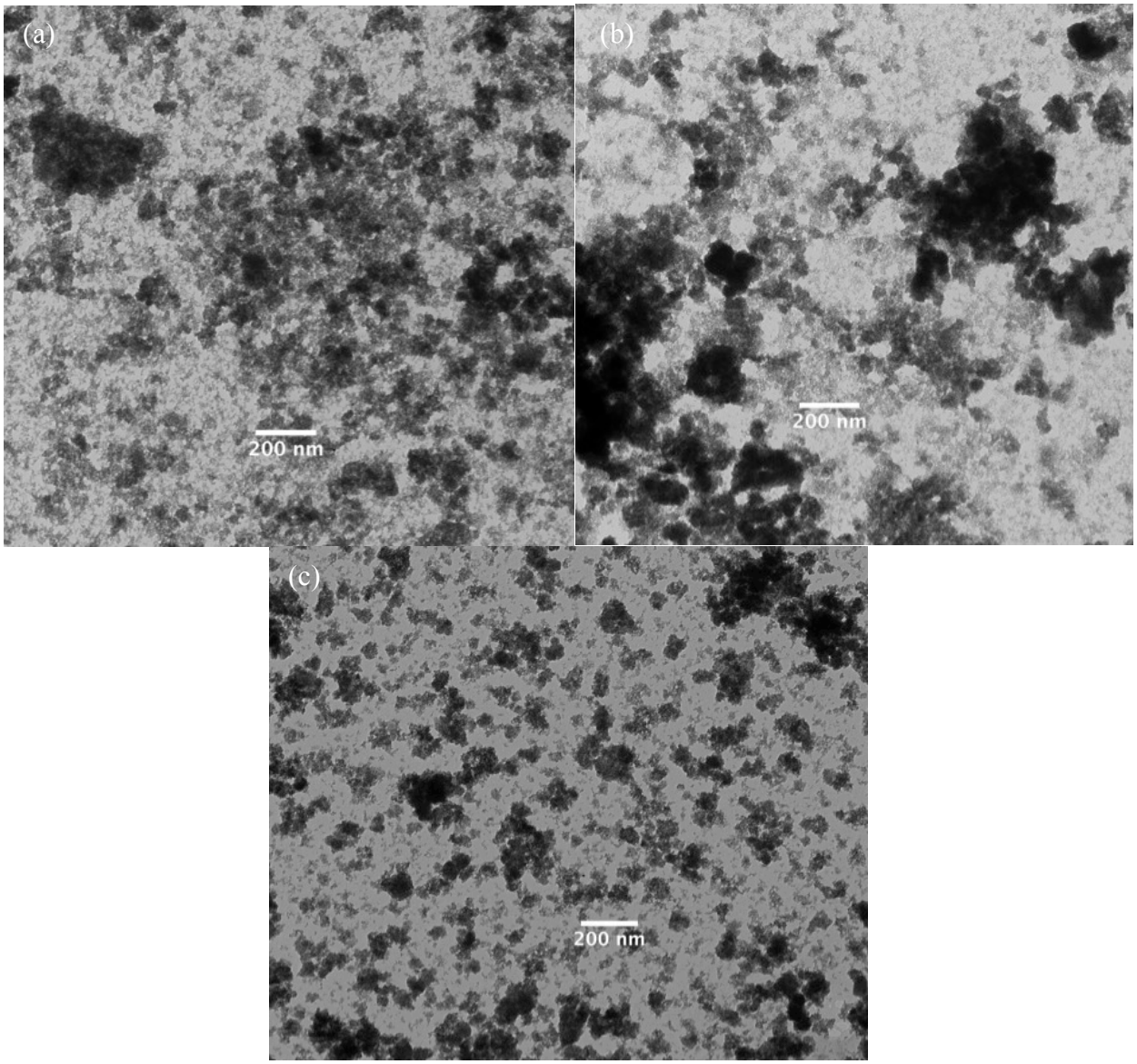

Figure A.4: TEM image of Sample 2 (a) at 2°C, (b) with SDS, and (c) with CTAB.

Terephthalic acid

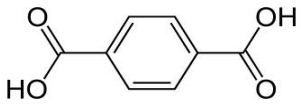

Hexadecyl trimethyl ammonium bromide (CTAB)

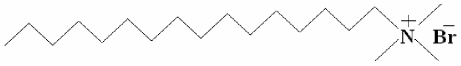

Triton X-100

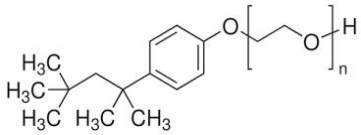

Sodium cholate hydrate

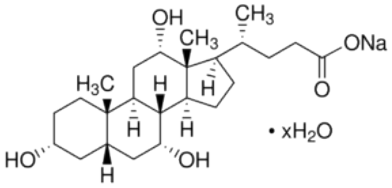

Sodium dodecyl sulfate (SDS)

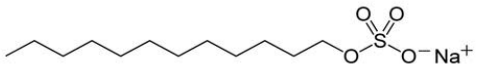

Sodium dodecyl benzene sulfonate (SDBS)

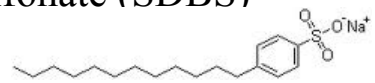

Figure A.5: Surfactants used in this work.

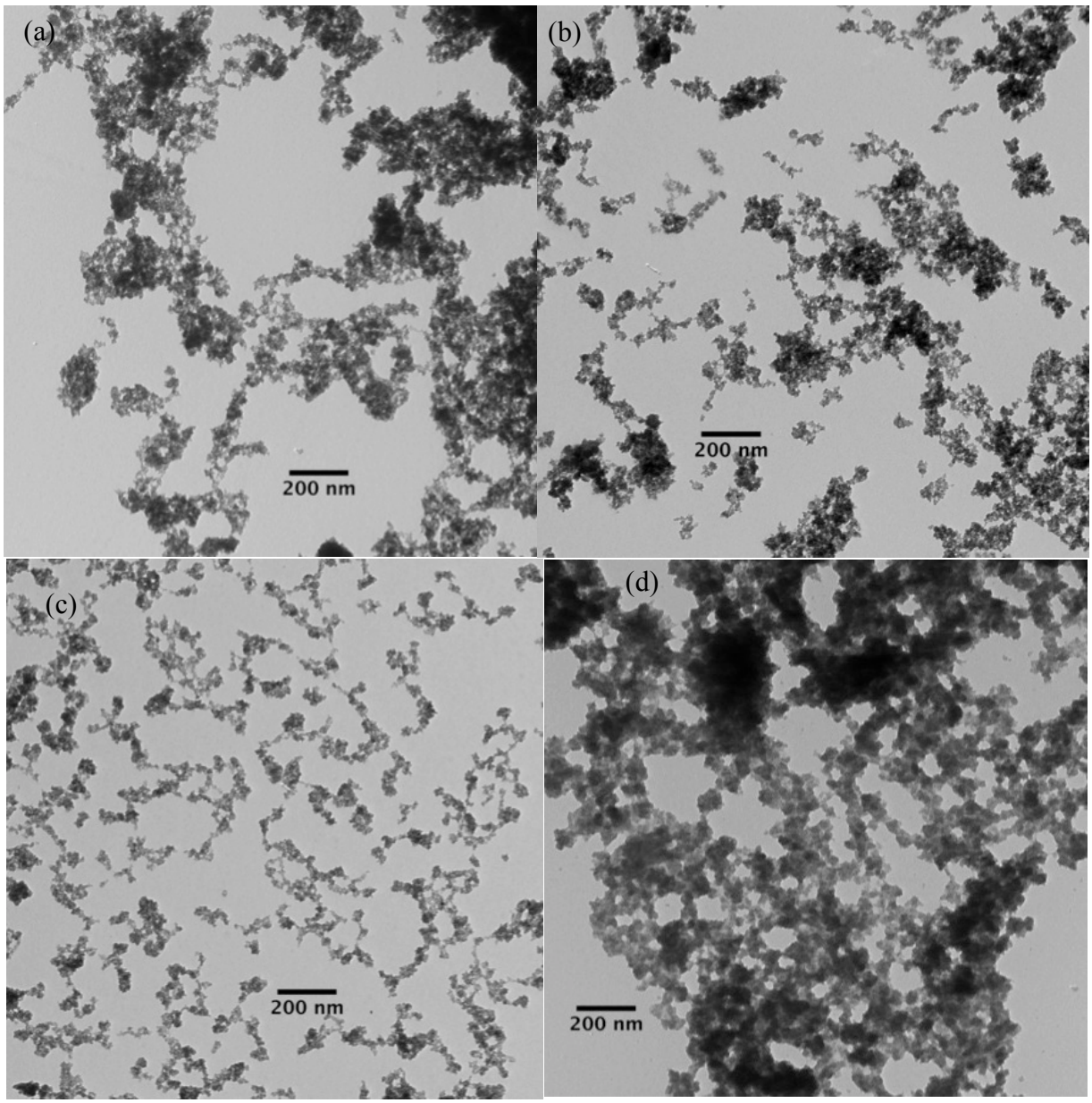

Figure A.6: TEM image of Sample 3 with (a) terephthalic acid, (b) SDS, (c) CTAB, and (d) sodium cholate hydrate.

Energy-dispersive X-ray spectroscopy (EDX) analysis establishes that the product is composed of 51.34% atomic weight sulfur and 48.66% zinc (Figure A.7). Furthermore, the X-ray diffraction (XRD) pattern contains peaks at 2θ equals to 29°, 48°, and 56° corresponding to 111, 220, 311 planes, respectively (Figure A.8). These values are representative of zinc blend, or

cubic zinc sulfide nanostructures, and are in agreement with published literatures.[46] However, the Fourier-transform infrared spectroscopy (ATR-FTIR) spectrum suggests the presence of surfactant in the final product. For example, the CTAB-assisted reaction has peaks at 1471 cm^{-1}, 2846 cm^{-1}, 2917 cm^{-1}, and 3216 cm^{-1} which are attributed to the methyl group of $N(CH_3)_3$, aliphatic C-H groups, and OH group from the absorbed moisture (Figure A.9).

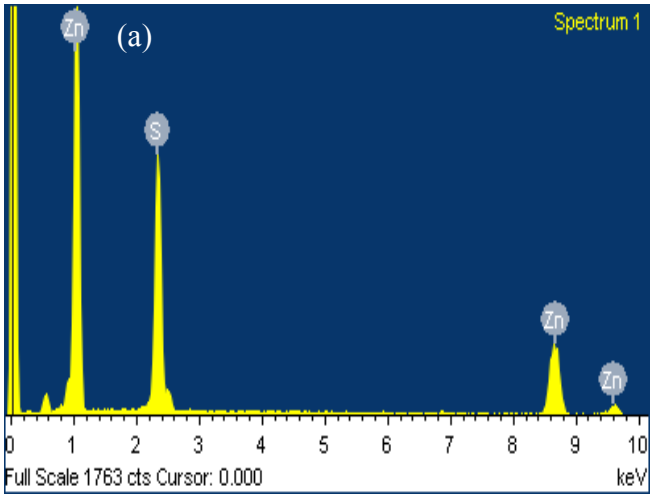

(b)

Element	Weight %	Atomic %
S	34.10	51.34
Zn	65.90	48.66
Total	100	100

Figure A.7: (a) EDX spectrum of Sample 1 and (b) EDX data of Sample 1.

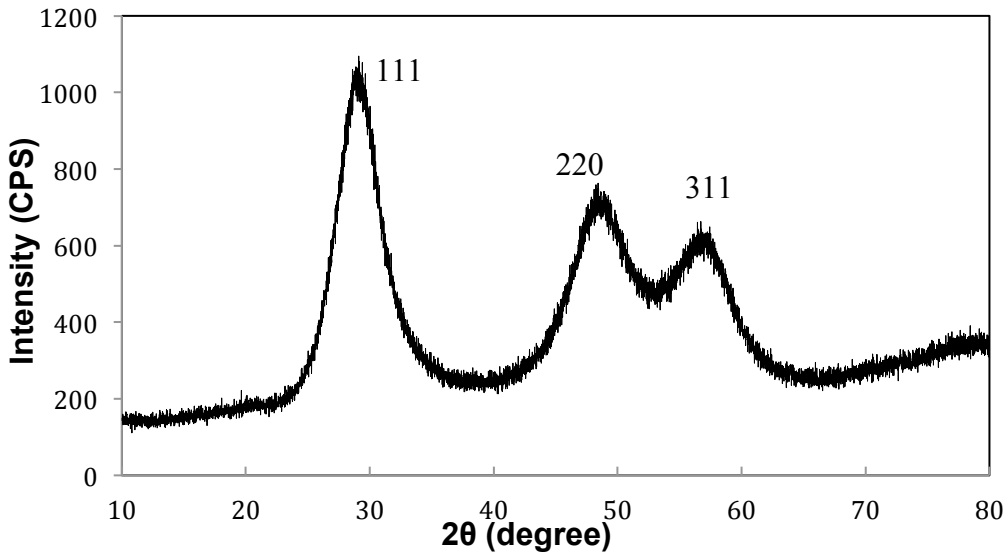

Figure A.8: XRD pattern of Sample 3 containing SDS.

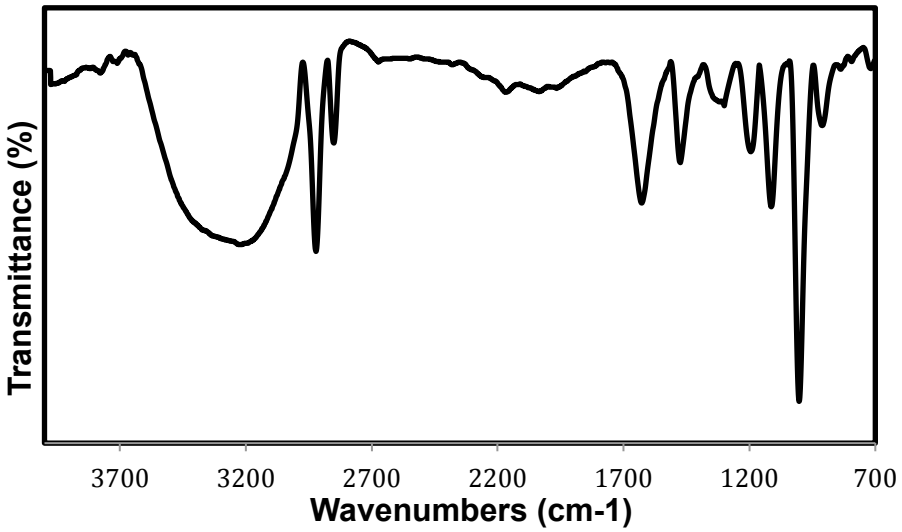

Figure A.9: ATR-FTIR spectrum of Sample 3 containing CTAB.

Some of the surfactant-containing reactions were heated at a high temperature to remove the surfactant that was still in the product after the purification step. This process was done under inert atmosphere (argon) to prevent oxidation of ZnS to ZnO nanostructures. In some cases annealing can be used to form crystalline structures.[47-51] In our case, we observed an elimination of the surfactant. The ATR-FTIR spectrum has no peaks due to the presence of the surfactant, indicating the removal of surfactant from the product (Figure A.10).

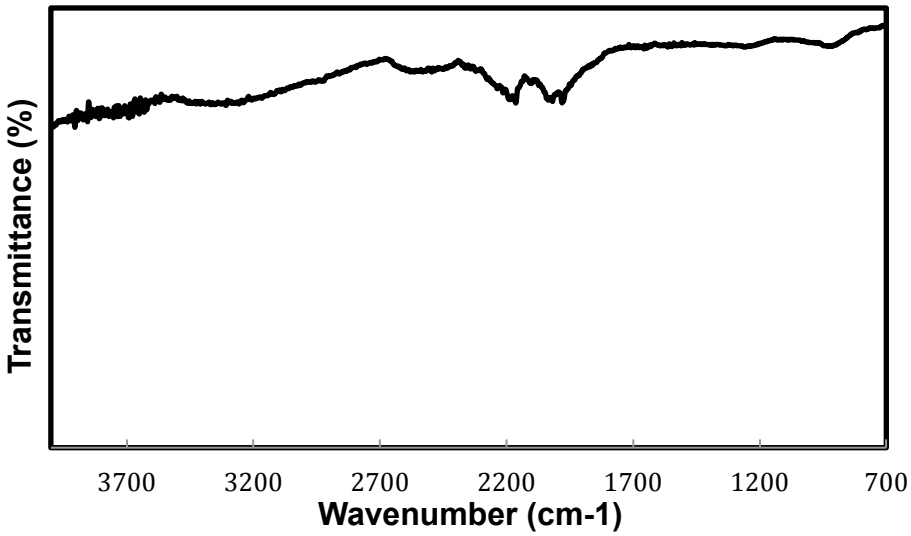

Figure A.10: ATR-FTIR spectrum of Sample 3 with CTAB after annealing.

An additional reaction was performed in reverse order with $Zn(NO_3)_2.6H_2O$ solution added to the mixture of Na_2S and surfactant revealing the order of addition has no influence in the fabrication of ZnS nanostructures. The TEM image shows identical products with both standard and reverse additions (Figure A.11). Also, an increase in temperature to 60°C has no impact (Figure A.12).

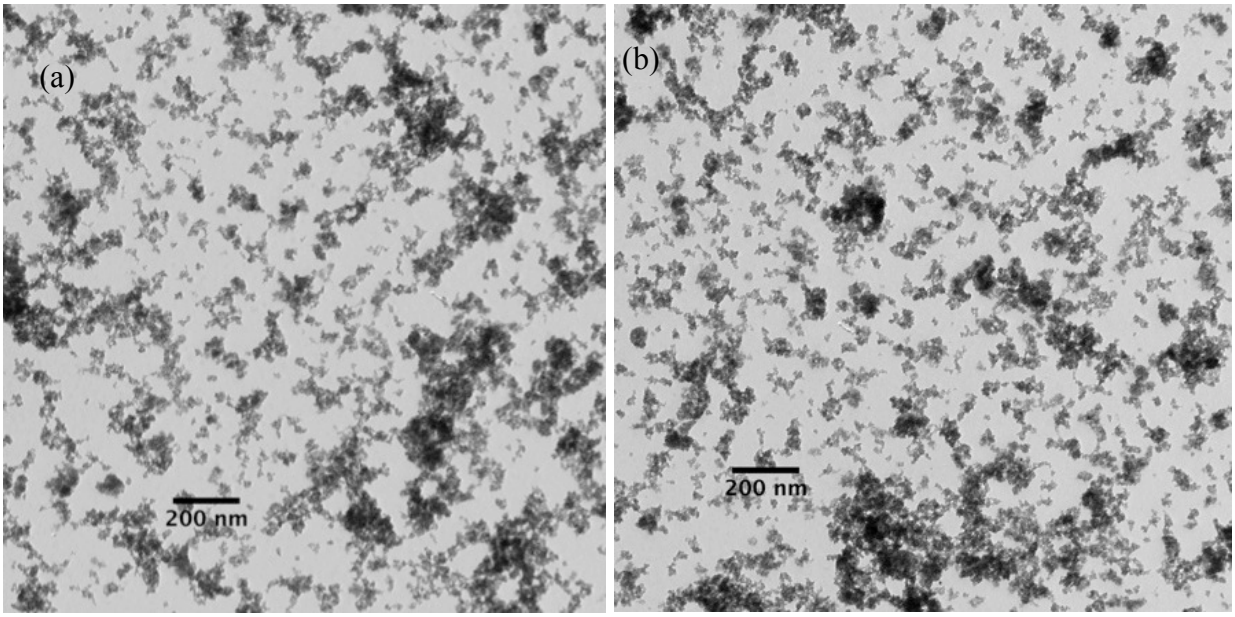

Figure A.11: TEM image of Sample 3 with triton X-100. (a) Standard addition and (b) reverse addition.

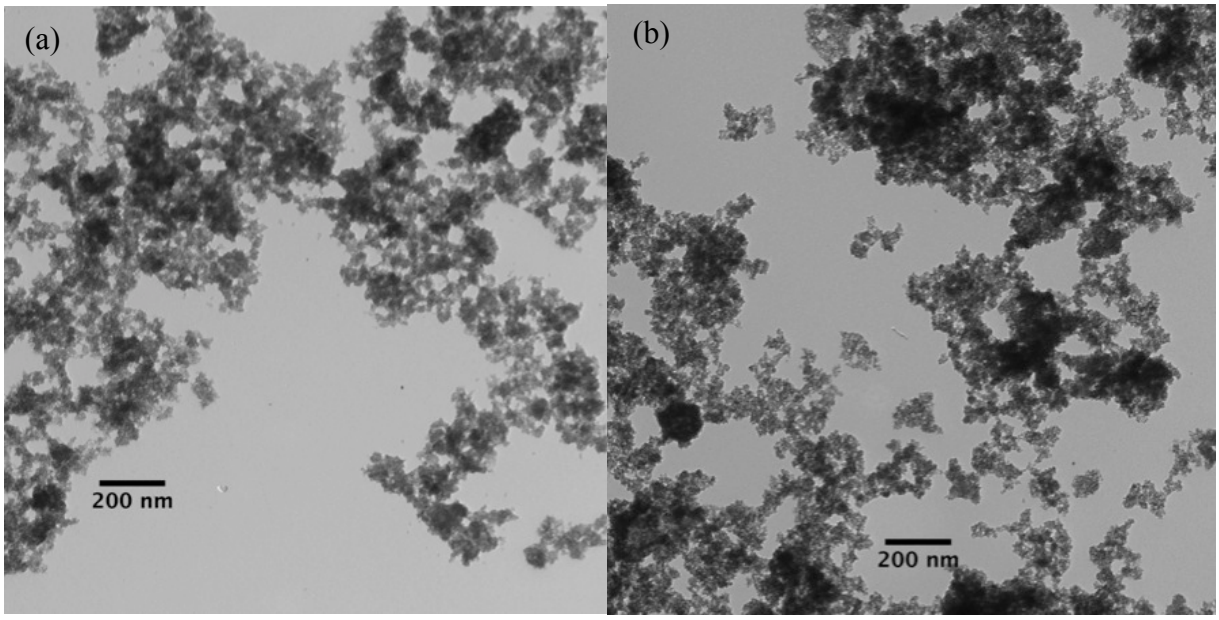

Figure A.12: TEM image of Sample 3 with sodium cholate hydrate at 60°C. (a) Standard addition and (b) reverse addition.

A.4.1.3 Reaction with Zinc Nitrate Hexahydrate and Thiourea (Sample 4)

Zinc nitrate hexahydrate and thiourea were mixed in water and refluxed above the boiling point of water. This reaction can occur in two ways. First, at low temperature thiourea can form a complex salt [$Zn(H_2NCSNH_2)_n)^{2+}$] with Zn, then the complex disintegrates to the final product ZnS (Equation A.3).[52] Second, thiourea can decompose to form diazomethane (CH_2N_2) and hydrogen sulfide (H_2S), which then reacts with water molecules and ZnS at a temperature above 105°C to produce in ZnS, ammonium gas, and carbon dioxide (Equation A.3).[53]

$$i,\quad Zn^{2+}+(H_2NCSNH_2)_n)\rightarrow[Zn(H_2NCSNH_2)_n)^{2+}] \qquad \text{(Equation A.3)}$$

$$ii,\quad H_2NCSNH_2\rightarrow CH_2N_2+H_2S$$

$$ii,\quad Zn(NO_3)_2.6H_2O+CH_2N_2+H_2S\rightarrow ZnS+2HNO_3\ 2NH_3+CO_2 \qquad \text{(Equation A.4)}$$

The reaction was done in a round-bottom flask as well as an autoclave. The use of autoclave allows hydrothermal approach, which maintains the temperature and pressure built up during the reaction. TEM images of the product display large particles with diameters of 1 μm and when a Teflon autoclave was used the particles were smaller but fused with each other (Figure A.13).

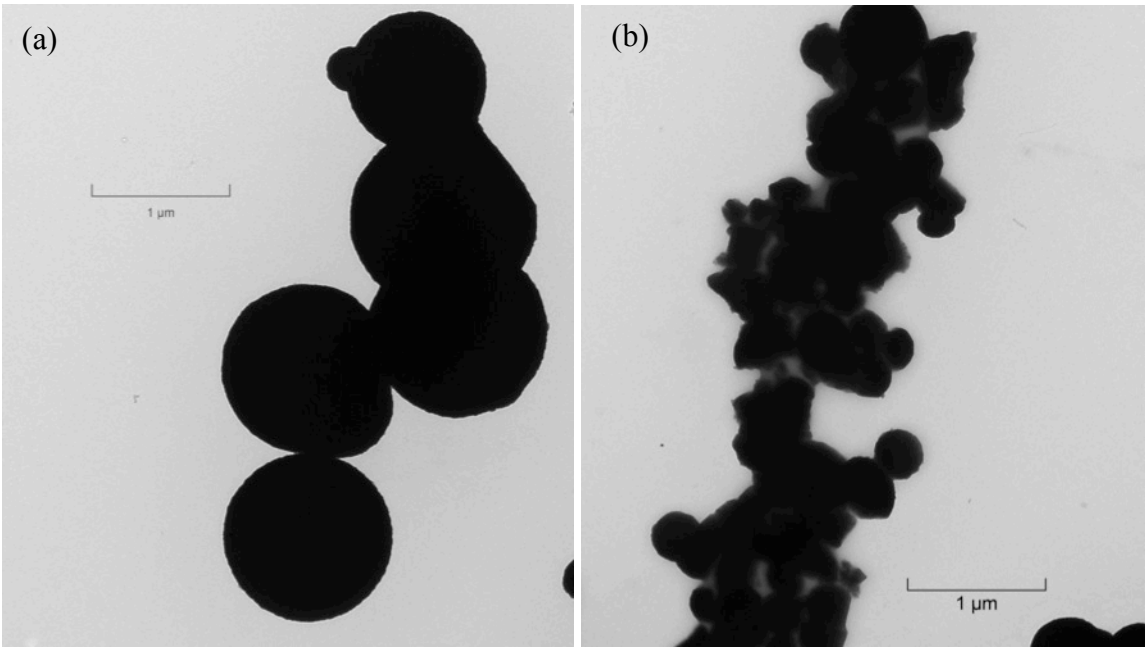

Figure A.13: TEM image of Sample 4 obtained using (a) round-bottom flask and (b) Teflon autoclave.

Next, a different polar solvent was used to accomplish a formation of nanoparticles with diameters less than 100 nm. The reaction temperature was varied starting from the boiling point of DMSO, which is 190°C, down to 130°C in order to decrease energy consumption. Low-temperature reaction with an extended reaction period did not produce any result, and during this proces, we learned that the temperature has to be above 140°C to observe any product formation. Therefore, the reaction temperature was selected to be 150°C, which will allow the complete

transformation of the reagents to products. Once the reaction parameters were established, various surfactants were used with the procedure in anticipation of seeing nanostructures with diverse morphology. TEM image of the product showed the formation of particles, rods, sheets and a mixture of particles and hollow spheres when CTAB, terephthalic acid, triton X-100, and SDS were utilized. However, an increase in concentration of surfactant had no impact on the ZnS product since both 5% and 10% surfactant loading resulted in identical structures (Figure A.14). Further, the increase in reaction time with terephthalic acid did not change the morphology of the nanorods.

The mixture of surfactant resulted in a product containing multiple morphologies. For example, a reaction containing triton X-100 and CTAB had nanosheets and nanoparticles as products (Figure A.15). ATR-FTIR spectrum shows the presence of surfactants in the product.

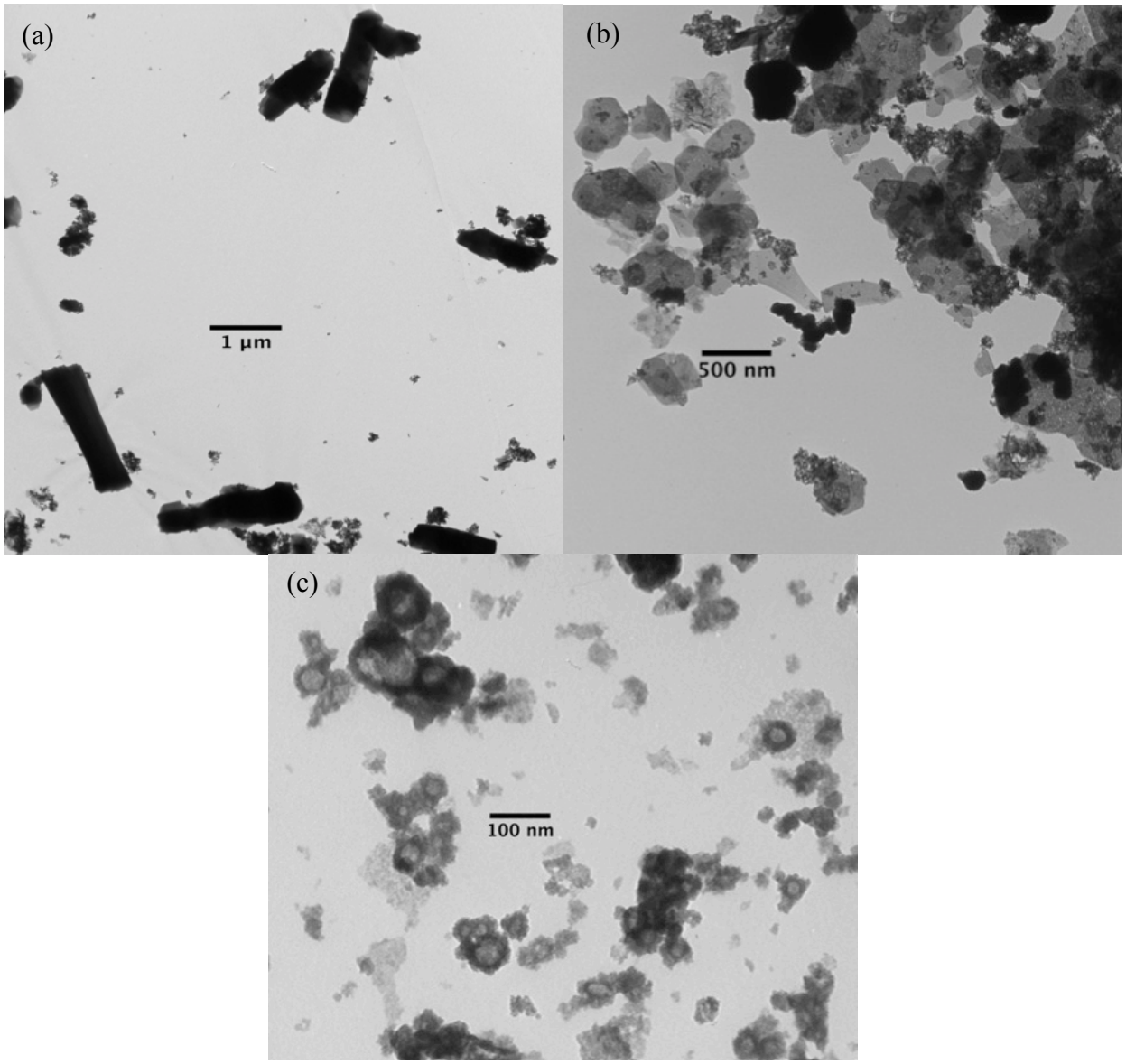

Figure A.14: TEM image of Sample 4 with (a) terephthalic acid, (b) triton X-100, and (c) SDS.

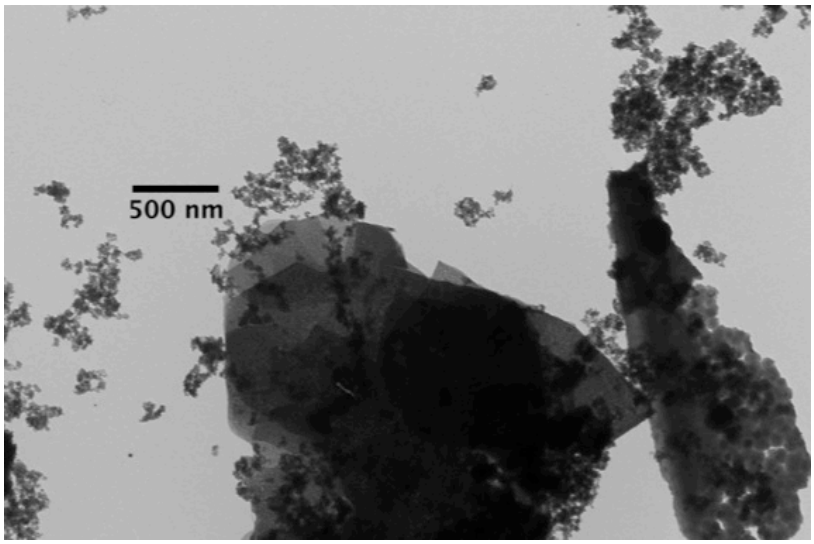

Figure A.15: TEM image of Sample 4 with a mixture of triton X-100 and CTAB.

A.4.1.4 Reaction with Zinc Chloride and Thiourea (Sample 5)

These two reagents used in diethylene glycol methyl ether formed ZnS nanosheets even after the addition of nonionic surfactants such as terephthalic acid, pluronic F 127, and sodium cholate hydrate. On the other hand, the use of anhydrous diglyme as a reaction medium and terephthalic acid resulted in a mixture of nanorods and nanoparticles (Figure A.16). Moreover, a larger surfactant loading produced more nanorods with an average diameter of 35 nm and a few micrometers in length. ATR-FTIR spectrum suggests that all of the surfactants were not removed from the product during the purification steps.

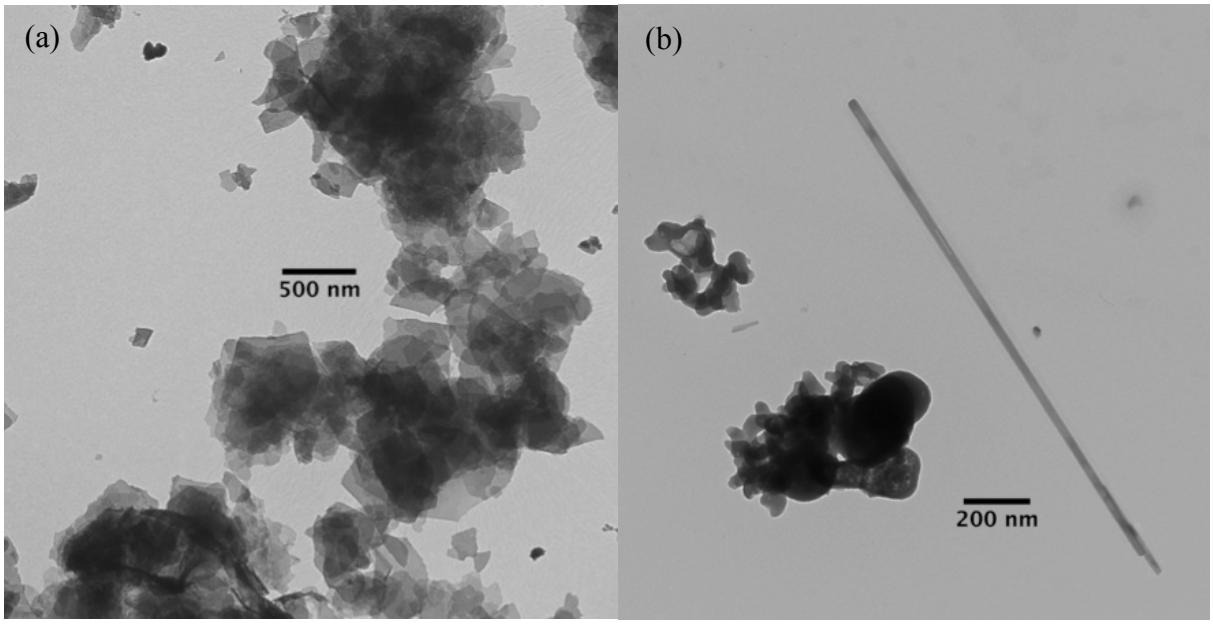

Figure A.16: TEM image of Sample 5 with terephthalic acid (a) in diethylene glycol methyl ether and (b) in anhydrous diglyme.

A.5 Summary and Conclusion

Four zinc and sulfur sources, namely zinc nitrate hexahydrate, zinc chloride, thiourea, and sodium sulfide nonahydrate, were used in different combinations to form ZnS nanostructures. The first combination was based on zinc chloride and sodium sulfide, but this group of reagents did not produce any ZnS nanostructures. The second combination was performed with zinc nitrate hexahydrate and sodium sulfide. This reaction produced nanoparticles when surfactants such as terephthalic acid, SDS, CTAB, and sodium cholate hydrate were added. The third pair utilizes zinc nitrate hexahydrate and thiourea to form ZnS nanoparticles. The presence of CTAB in the reaction had no influence, yet terephthalic acid, triton X-100, and SDS resulted in ZnS nanorods, nanosheets, and a mixture of nanoparticles and hollow spheres, respectively. Further, the addition of more than one surfactant can lead to the

development of various structures in a single product. The last combination was done using zinc chloride and thiourea; with this reaction, diethylene glycol methyl ether or anhydrous diglyme were used as a solvent. Incorporation of terephthalic acid with anhydrous diglyme formed ZnS nanorods, whereas in anhydrous diglyme we observe only ZnS nanosheets regardless of the existence of surfactant. EDX analysis proves the product is composed of zinc and sulfur while ATR-FTIR reveals the presence of surfactant. Also, XRD pattern confirms the ZnS nanostructures were zinc blend or cubic.

References

1. Miao, W.J.; Electrogenerated chemiluminescence and its biorelated applications. *Chem. Rev.,* **2008**,108, 2506–2553.

2. Deng, Z.; Qi, J.; Zhang, Y.; Liao, Q.; Huang, Y. Growth Mechanism And Optical Properties Of Zns Nanotetrapods. *Nanotechnology,* **2007**,*18*, 475603.

3. Zhai, T.; Gu, Z.; Fu, H.; Ma, Y.; Yao, J. Synthesis Of Single-Crystal Zns Nanoawls Via Two-Step Pressure-Controlled Vapor-Phase Deposition And Their Optical Properties. *Cryst. Growth Des.,* **2007**, 7, 1388-1392.

4. Fang, X.; Gautam, U.; Bando, Y.; Dierre, B.; Sekiguchi, T.; Golberg, D. Multiangular Branched Zns Nanostructures With Needle-Shaped Tips: Potential Luminescent And Field-Emitter Nanomaterial. *J. Phys. Chem. C,* **2008**, 112, 4735-4742.

5. Chen, Z.; Zou, J.; Wang, D.; Yin, L.; Liu, G.; Liu, Q.; Sun, C.; Yao, X.; Li, F.; Yuan, X. et al. Field Emission And Cathodoluminescence Of Zns Hexagonal Pyramids Of Zinc Blende Structured Single Crystals. *Adv. Funct.l Mater.,* **2009**, 19, 484-490.

6. Jie, J.; Zhang, W.; Jiang, Y.; Meng, X.; Zapien, J.; Shao, M.; Lee, S. Heterocrystal And Bicrystal Structures Of Zns Nanowires Synthesized By Plasma Enhanced Chemical Vapour Deposition. *Nanotechnology,* **2006**, 17, 2913-2917.

7. Liu, Y.; Feng, P.; Xue, X.; Shi, S.; Fu, X.; Wang, C.; Wang, Y.; Wang, T. Room-Temperature Oxygen Sensitivity Of Zns Nanobelts. *Appl. Phys. Lett.* **2007**, 90, 042109.

8. Yang, L.; Han, J.; Luo, T.; Li, M.; Huang, J.; Meng, F.; Liu, J. Morphogenesis And Crystallization Of Zns Microspheres By A Soft Template-Assisted Hydrothermal Route: Synthesis, Growth Mechanism, And Oxygen Sensitivity. *Chem. Asian J.,* **2009**, 4, 174-180.

9. Chen, Z.; Zou, J.; Liu, G.; Lu, H.; Li, F.; Lu, G.; Cheng, H. Silicon-Induced Oriented Zns Nanobelts For Hydrogen Sensitivity. *Nanotechnology,* **2008**, 19, 055710.

10. He, J.; Zhang, Y.; Liu, J.; Moore, D.; Bao, G.; Wang, Z. Zns/Silica Nanocable Field Effect Transistors As Biological And Chemical Nanosensors. *J. Phys. Chem. C,,* **2007**, 111, 12152-12156.

11. Koneswaran, M.; Narayanaswamy, R. L-Cysteine-Capped Zns Quantum Dots Based Fluorescence Sensor For Cu2+ Ion. *Sensors and Actuat B,* **2009**, 139, 104-109.

12. Wang, Z. L.; Song, J.H.; Piezoelectric Nanogenerators Based On Zinc Oxide Nanowire Arrays. *Science,* **2006**, 312, 242-246.

13. Wang ZL. Energy harvesting using piezoelectric nanowires – a correspondence on ‘‘energy harvesting using nanowires?’’ by Alexe et al.. *Adv. Mater.,* **2009**;21:1311–1315.

14. Duong, H.; Rhee, J. Use Of Cdse/Zns Core-Shell Quantum Dots As Energy Transfer Donors In Sensing Glucose. *Talanta,* **2007**, 73, 899-905.

15. Uematsu, T.; Taniguchi, S.; Torimoto, T.; Kuwabata, S. Emission Quench Of Water-Soluble Zns–Agins2 Solid Solution Nanocrystals And Its Application To Chemosensors. *Chem. Commun.,* **2009**, 7485-7487.

16. Yuan, G. D.; Zhang, W. J.; Zhang, W. F.; Fan, X.; Bello, I.; Lee, C. S.; *Appl. Phys. Lett.,* **2008**, 93:213102.

17. Shen, G.; Chen, P.; Bando, Y.; Golberg, D.; Zhou, C. Pearl-Like Zns-Decorated Inp Nanowire Heterostructures And Their Electric Behaviors. *Chem. Mater.,* **2008**, 20, 6779-6783.

18. Hu, J.; Ren, L.; Guo, Y.; Liang, H.; Cao, A.; Wan, L.; Bai, C. Mass Production And High Photocatalytic Activity Of Zns Nanoporous Nanoparticles. *Angew. Chem.,* **2005**, 117, 1295-1299.

19. Henglein, A.; Gutiérrez, M.; Fischer, C. Photochemistry Of Colloidal Metal Sulfides 6. Kinetics Of Interfacial Reactions At Zns-Particles. *Ber. Bunsen. Phys. Chem.,* **1984**, 88, 170-175.

20. Fang, X.; Zhai, T.; Gautam, U.; Li, L.; Wu, L.; Bando, Y.; Golberg, D. Zns Nanostructures: From Synthesis To Applications. *Prog. Mater. Sci.* **2011**, 56, 175-287.

21. Fang, X.; Ye, C.; Zhang, L.; Wang, Y.; Wu, Y. Temperature-Controlled Catalytic Growth Of Zns Nanostructures By The Evaporation Of Zns Nanopowders. *Adv. Funct. Mater.,* **2005**, 15, 63-68.

22. Tonikian, R.; Proulx, G.; Benichou, N.; Reid, I. Literature Review on Photoluminescent Material Used as a Safety Wayguidance System**.** *IRC-RR-214,* **2006**, V6-2, doc2.

23. Kanemoto, M.; Hosokawa, H.; Wada, Y.; Murakoshi, K.; Yanagida, S.; Sakata, T.; Mori, H.; Ishikawa, M.; Kobayashi, H. Semiconductor Photocatalysis. Part 20. Role Of Surface In The Photoreduction Of Carbon Dioxide Catalysed By Colloidal Zns Nanocrystallites In Organic Solvent. *J. Chem. Soc. Faraday Trans.* **1996**, 92, 2401-2411.

24. Bredol, M.; Kaczmarek, M. Potential Of Nano-Zns As Electrocatalyst . *J. Phys. Chem. A,* **2010**, 114, 3950-3955.

25. Luo, L.; Chen, H.; Zhang, L.; Xu, K.; Lv, Y. A Cataluminescence Gas Sensor For Carbon Tetrachloride Based On Nanosized Zns. *Analytica Chimica Acta.,* **2009**, 635, 183-187.

26. Moore, D.; Wang, Z. Growth Of Anisotropic One-Dimensional Zns Nanostructures. *J. Mater. Chem.*, **2006**, 16, 3898 –3905.

27. Joo, J.; Na, H.; Yu, T.; Yu, J.; Kim, Y.; Wu, F.; Zhang, J.; Hyeon, T. Generalized And Facile Synthesis Of Semiconducting Metal Sulfide Nanocrystals. *J. Am. Chem. Soc.* **2003**, 125, 11100-11105.

28. Talapin, D.; Rogach, A.; Kornowski, A.; Haase, M.; Weller, H. Highly Luminescent Monodisperse Cdse And Cdse/Zns Nanocrystals Synthesized In A Hexadecylamine−Trioctylphosphine Oxide−Trioctylphospine Mixture. *Nano Letters* **2001**, 1, 207-211.

29. Liu, H.; Ni, Y.; Han, M.; Liu, Q.; Xu, Z.; Hong, J.; Ma, X. A Facile Template-Free Route For Synthesis Of Hollow Hexagonal Zns Nano- And Submicro-Spheres. *Nanotechnology,* **2005**, 16, 2908-2912.

30. Ma, Y.; Qi, L.; Ma, J.; Cheng, H. Facile Synthesis Of Hollow Zns Nanospheres In Block Copolymer Solutions. *Langmuir,* **2003**, 19, 4040-4042.

31. Kalyanikutty, K.; Nikhila, M.; Maitra, U.; Rao, C. Hydrogel-Assisted Synthesis Of Nanotubes And Nanorods Of Cds, Zns And Cus, Showing Some Evidence For Oriented Attachment. *Chem. Phys. Lett.,* **2006**, 432, 190-194.

32. Wang, X.; Gao, P.; Li, J.; Summers, C.; Wang, Z. Rectangular Porous Zno–Zns Nanocables And Zns Nanotubes. *Adv. Mater.* **2002**, 14, 1732-1735.

33. Wang, Y.; Zhang, L.; Liang, C.; Wang, G.; Peng, X. Catalytic Growth And Photoluminescence Properties Of Semiconductor Single-Crystal Zns Nanowires. *Chem. Phys. Lett.,* **2002**, 357, 314-318.

34. Imtiaz, A.; Farrukh, M.; Khaleeq-ur-rahman, M.; Adnan, R. Micelle-Assisted Synthesis Of Al2o3·Cao Nanocatalyst: Optical Properties And Their Applications In Photodegradation Of 2,4,6-Trinitrophenol. *The Scientific World Journal,* **2013**, 1-11.

35. Ding, X.; Han, D.; Wang, Z.; Xu, X.; Niu, L.; Zhang, Q. Micelle-Assisted Synthesis Of Polyaniline/Magnetite Nanorods By In Situ Self-Assembly Process. *J. Colloid Interface Sci.,* **2008**, 320, 341-345.

36. Fan, H.; Leve, E.; Scullin, C.; Gabaldon, J.; Tallant, D.; Bunge, S.; Boyle, T.; Wilson, M.; Brinker, C. Surfactant-Assisted Synthesis Of Water-Soluble And Biocompatible Semiconductor Quantum Dot Micelles. *Nano Letters,* **2005**, 645-648.

37. Xi, L.; Lam, Y.; Xu, Y.; Li, L. Synthesis And Characterization Of One-Dimensional Cdse By A Novel Reverse Micelle Assisted Hydrothermal Method. *J. Colloid Interface Sci.,* **2008**, 320, 491-500.

38. Wu, P.; Zhu, J.; Xu, Z. Template-Assisted Synthesis Of Mesoporous Magnetic Nanocomposite Particles. *Adv. Funct. Mater.,* **2004**, 14, 345-351.

39. Wang, S.; Xu, H.; Qian, L.; Jia, X.; Wang, J.; Liu, Y.; Tang, W. CTAB-Assisted Synthesis And Photocatalytic Property Of Cuo Hollow Microspheres. *J. Solid State Chem.,* **2009**, 182, 1088-1093.

40. Moon, S.; Kusunose, T.; Sekino, T. CTAB-Assisted Synthesis Of Size- And Shape-Controlled Gold Nanoparticles In SDS Aqueous Solution. *Materials Letters,* **2009**, 63, 2038-2040.
41. Pasquali, M. Gelation: Grow With The Flow. *Nat Mater.,* **2010**, 9, 381-382.

42. Zhao, Q.; Hou, L.; Huang, R. Synthesis Of Zns Nanorods By A Surfactant-Assisted Soft Chemistry Method. *Inorg. Chem. Commun.,* **2003**, 6, 971-973.

43. Zhao, Z.; Geng, F.; Cong, H.; Bai, J.; Cheng, H. A Simple Solution Route To Controlled Synthesis Of Zns Submicrospheres, Nanosheets And Nanorods. *Nanotechnology,* **2006**, 17, 4731-4735.

44. Goodell, C.; Gilbert, B.; Weigand, S.; Banfield, J. Kinetics Of Water Adsorption-Driven Structural Transformation Of Zns Nanoparticles. *J. Phys. Chem. C,* **2008**, 112, 4791-4796.

45. Chung, J.; Myoung, J.; Oh, J.; Lim, S. Synthesis Of A Zns Shell On The Zno Nanowire And Its Effect On The Nanowire-Based Dye-Sensitized Solar Cells. *J. Phys. Chem. C,* **2010**, 114, 21360-21365.

46. Qadri, S.; Skelton, E.; Hsu, D.; Dinsmore, A.; Yang, J.; Gray, H.; Ratna, B. Size-Induced Transition-Temperature Reduction In Nanoparticles Of Zns. *Phys. Rev. B,* **1999**, 60, 9191-9193.

47. Son, D.; Jung, D.; Kim, J.; Moon, T.; Kim, C.; Park, B. Synthesis And Photoluminescence Of Mn-Doped Zinc Sulfide Nanoparticles. *Appl. Phys. Lett.* **2007**, 90, 101910.

48. Tsuzuki, T.; Ding, J.; McCormick, P. Mechanochemical Synthesis Of Ultrafine Zinc Sulfide Particles. *Physica B.* **1997**, 239, 378-387.

49. Murali, G.; Reddy, D. A.; Poornaprakash, B.; Vijayalakshmi, R. P.; Rao N. M.; Effect of annealing on structural and optical properties of ZnS nanocrystals. *Optoelectron. Adv. Mater.* **2011**, 5, 928 – 931.

50. Gómez-Barojas, E.; Sánchez-Mora, E.; Mendoza-Dorantes, T.; Castillo-Abriz, C.; Silva-González, R. Study Of 4 The Influence Of Annealing Parameters On The Optical And Compositional Properties Of Zns, Zns:Mn And Zns:Sm Grown By Sol Gel. *J. Phys.: Conf. Ser.* **2009**, 167, 012051.

51. Lan, C.; Hong, K.; Wang, W.; Wang, G. Synthesis Of Zns Nanorods By Annealing Precursor Zns Nanoparticles In Nacl Flux. *Solid State Commun.* **2003**, 125, 455-458.

52. Qin, A.; Fang, Y.; Ou, H.; Liu, H.; Su, C. Formation Of Various Morphologies Of Covellite Copper Sulfide Submicron Crystals By A Hydrothermal Method Without Surfactant. *Cryst. Growth Des.,* **2005**, 5, 855-860.

53. Zhao, Z.; Geng, F.; Cong, H.; Bai, J.; Cheng, H. A Simple Solution Route To Controlled Synthesis Of Zns Submicrospheres, Nanosheets And Nanorods. *Nanotechnology,* **2006**, 17, 4731-4735.